INVESTIGATION OF TECTONIC STRUCTURES IN THE AREA BETWEEN
MARMARİS AND FETHİYE BAY


A THESIS SUBMITTED TO
THE GRADUATE SCHOOL OF NATURAL AND APPLIED SCIENCES
OF
MIDDLE EAST TECHNICAL UNIVERSITY


BY

AYHAN YAVUZOĞLU


IN PARTIAL FULFILLMENT OF THE REQUIREMENTS
FOR
THE DEGREE OF MASTER OF SCIENCE
IN
GEOLOGICAL ENGINEERING


SEPTEMBER 2019

Approval of the thesis:

**INVESTIGATION OF TECTONIC STRUCTURES IN THE AREA BETWEEN MARMARİS AND FETHİYE BAY**

submitted by **AYHAN YAVUZOĞLU** in partial fulfillment of the requirements for the degree of **Master of Science in Geological Engineering Department, Middle East Technical University** by,

Prof. Dr. Halil Kalıpçılar
Dean, Graduate School of **Natural and Applied Sciences**       _____

Prof. Dr. Erdin Bozkurt
Head of Department, **Geological Engineering Dept.**       _____

Prof. Dr. Erdin Bozkurt
Supervisor, **Geological Engineering Dept., METU**       _____


**Examining Committee Members:**

Prof. Dr. Erdinç Yiğitbaş
Geological Engineering Dept., ÇOMU       _____

Prof. Dr. Erdin Bozkurt
Geological Engineering Dept., METU       _____

Prof. Dr. Gürol Seyitoğlu
Geological Engineering Dept., Ankara University       _____

Assoc. Prof. Dr. Bülent Kaypak
Geophysical Engineering Dept., Ankara University       _____

Assist. Prof. Dr. Ulaş Avşar
Geological Engineering Dept., METU       _____

Date: 13.09.2019

I hereby declare that all information in this document has been obtained and presented in accordance with academic rules and ethical conduct. I also declare that, as required by these rules and conduct, I have fully cited and referenced all material and results that are not original to this work.

Name, Surname: Ayhan Yavuzoğlu

Signature:

**ABSTRACT**


**INVESTIGATION OF TECTONIC STRUCTURES IN THE AREA
BETWEEN MARMARİS AND FETHİYE BAY**

Yavuzoğlu, Ayhan
Master of Science, Geological Engineering
Supervisor: Prof. Dr. Erdin Bozkurt

September 2019, 145 pages

The relationship between, and continuum of, the Fethiye-Burdur Fault Zone (FBFZ) and Pliny-Strabo STEP fault zone are still debated and different school propose different models on the subject. The area between Finike Bay in the east and Datça Bay in the west along the Mediterranean Sea coastline forms one of the key locations because it lies at the linkage of the two major structures. This research therefore aims to address the existing controversies, shed light on the structural features in the northeastern part of the STEP fault zone and enlighten tectonic evolution of the STEP fault zone and the Anatolian Plate.

Seven 2D seismic sections (352 km long marine seismic data collected by MTA Sismik-1 ) are interpreted not only to explaining tectonic evolution of post-Messinian succession but also for understanding the active tectonic structures in the present area. Seismic interpretation revealed two main deformation periods until recent tectonic regime and presence of NE-SW striking faults in the region.

Focal mechanism solution of the most representative 6 (six) major earthquake are also carried out and the results indicate presence of mostly dextral also sinistral faulting as well in study area.

Correlation of focal mechanism solution and seismic interpretation indicate right-lateral strike-slip faulting is not compatible with the regional constraints that suggest left-lateral strike-slip faulting both in the FBFZ and the Pliny-Strabo STEP fault zone. This brings more confusion about the nature of faulting in the region. It is therefore suggest more detailed work is required for further discussion.

Keywords: 2D Seismics, Marmaris-Fethiye Bay, Active Tectonic, Focal mechanism solution, Fethiye-Burdur Fault Zone and Pliny-Strabo STEP fault zone

# ÖZ

## MARMARİS VE FETHİYE KÖRFEZLERİ ARASININ TEKTONİK YAPILARININ ARAŞTIRILMASI

Yavuzoğlu, Ayhan
Yüksek Lisans, Jeoloji Mühendisliği
Tez Danışmanı: Prof. Dr. Erdin Bozkurt

Eylül 2019, 145 sayfa

Fethiye-Burdur fay zonu ile Pliny Strabo fay zonu'nun ilişkisi ve devamlılığı tartışmalı olmakla birlikte bu konu hakkında değişik araştırmacı grupları tarafından değişik modeller önerilmiştir. Batıda Datça körfezi ile doğuda Finike körfezi arasında kalan alan iki ana yapının bağlantısının bulunduğu en önemli lokasyonlardan biridir. Bu çalışma, hâlihazırda bulunan tartışmaların üzerine eğilerek STEP fay zonu'nun kuzeybatı kesiminin yapısal özelliklerine ışık tutmayı ve STEP fay zonu ile Anadolu plakasının tektonik evrimini aydınlatmayı amaçlamaktadır.

Yedi tane 2 boyutlu (MTA Sismik 1 ile 352 km uzunluğunda deniz sismik verisi) sismik kesit sadece Messiniyen sonrası çökellerin tektonik evrimini değil, aynı zamanda alanda bulunan aktif tektonik yapıları anlamak amacı ile yorumlanmıştır. Sismik yorumlar ile güncel tektonik rejime kadar olan zaman diliminde iki önemli deformasyon süreci ve KD-GB doğrultulu faylar ortaya konulmuştur.

Çalışma alanını en iyi temsil eden altı (6) önemli depremin odak mekanizma çözümlerinin de yapılmasıyla çoğunlukla sağ yanal atımlı fayların yanında sol yanal atımlı fayların varlığını da ortaya koymuştur.

Odak mekanizma çözümleri ile sismik yorumların deneştirilmesi sonucunda ortaya çıkan sağ-yanal atımlı faylar, FBFZ ve Pliny-Strabo STEP fay zonlarının sol-yanal atımlı hareketlerinin alansal kısıtlamaları ile belirtilen yapıyla uyumlu değildir. Bu durum bölge'de ki fayların doğası hakkında daha fazla karışıklık oluşturmaktadır. Bu nedenle, daha ileri tartışma için daha ayrıntılı çalışma yapılması gerektiği önerilmektedir.



Anahtar Kelimeler: 2B sismikler, Marmaris-Fethiye körfezleri, Aktif Tektonik, Odak mekanizma çözümü, Fethiye-Burdur Fay zonu ve Pliny-Strabo STEP fay zonu

To My Family

# ACKNOWLEDGEMENTS

# TABLE OF CONTENTS

# LIST OF TABLES

# LIST OF FIGURES

FIGURES

xxv

# LIST OF ABBREVIATIONS

ABBREVIATIONS

| | |
|---|---|
| 2D | Two Dimensional |
| 3D | Three dimensional |
| AMS | Anisotropy of Magnetic Susceptibility |
| BHZ | Broadband VerticaL Component |
| CDP | Common Depth Point |
| CRS | Common Reflected Surface |
| DDA | National Seismic Networks of Turkey |
| CMP | Common Mid Point |
| EAFZ | East Anatolian Fault Zone |
| FDSN | International Federation of Digital Seismographs Networks |
| FBFZ | Fethiye Burdur Fault Zone |
| HHZ | Broadband Vertical Component |
| HNZ | Broadband Vertical Component (for strong motion) |
| GPS | Global Positioning System |
| GSAC | Generic Seismic Application Computing |
| KOERI | Boğaziçi Uni. Kandilli Observatory and Earthquake Research İnst. |
| Mb | Body Wave Magnitude |
| Ms | Surface Wave Magnitude |

| | |
|---|---|
| Mo | Seismic Moment |
| Mw | Moment Magnitude |
| MTA | General Directorate of Mineral Research and Exploration |
| NAFZ | North Anatolian Fault Zone |
| NMO | Normal Move Out |
| RV | Research Vessel |
| SEG | Society of Exploration Geophysicists |
| STEP | Subduction Transform Edge Propagator |
| USGS | United States Geological Survey |

# CHAPTER 1

# INTRODUCTION

## 1.1. Background

Anatolia is located within the Alpine-Himalayan mountain belt − orogenic belt along the southern margin of Eurasia that formed by Mesozoic−Cenozoic to recent closure of Tethyan ocean (s) and consequent continent-continent collision between the northward-moving Africa, Arabia and India (Gondwanaland) in the south, and the Asia-Europe (Laurasia) in the north. At present, Anatolia occurs within the ongoing convergence zone of Arabian, African and Eurasian plates in the Eastern Mediterranean (e.g., McKenzie, 1970, 1972; McKenzie et al., 1970; Dewey & Şengör, 1979; Dewey et al., 1986; Le Pichon & Kreemer, 2010) and takes place along the southern margin of Eurasian Plate where intense deformation prevails due to convergence of these plates. Anatolia also moves west- to southwest-ward and rotates counterclockwise relative to Eurasia and Arabia along its bounding structures (North Anatolian Fault, NAF in the north and East Anatolian Fault, EAF in the south) since the complete demise of the southern Neotethyan Ocean along the Bitlis-Zagros Suture. The suture has formed in response to early to middle Miocene continent-continent collision between Arabian and Eurasian plates (e.g., Ketin, 1948; McKenzie, 1976; Dewey & Şengör, 1979; Şengör, 1979; Şengör et al., 1985; Dewey et al., 1986; McClusky et al., , 2000; Faccenna et al., 2006; Reilinger et al., , 2006; Hollenstein et al., 2008; Kaymakcı et al., 2010; Okay et al., 2010; Biryol et al., , 2011 Rolland et al., , 2012; Müller et al., 2013; McQuarrie & van Hinsbergen, 2013; Philippon et al., 2015; Cawazza et al., 2018 and references therein) (Figure 1.1).

1
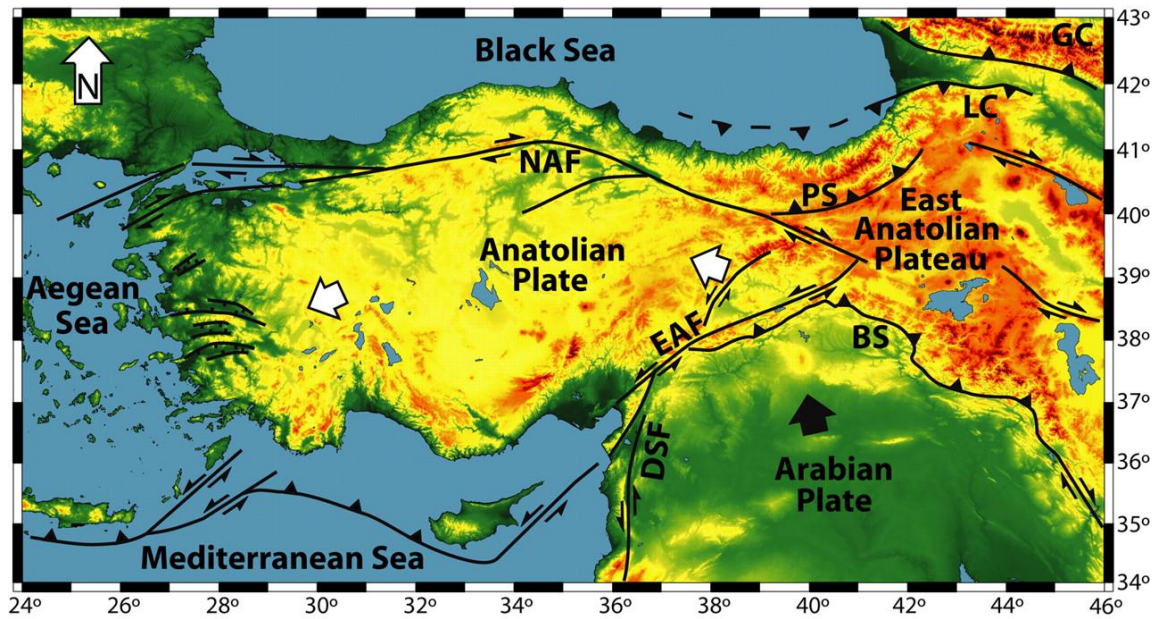
*Figure 1.1. A simplified neotectonic map of Turkey with topographic relief. Arrows indicate the direction of plate motions; half arrows, the fault motions. NAF, North Anatolian Fault; EAF, East Anatolian Fault; DSF, Dead Sea Fault; BS, Bitlis Suture; PS, Pontide Suture; LC, Lesser Caucasus; GC, Greater Caucasus (from Özacar et al., 2010).*

Southwestern Turkey is placed at one of the most tectonically active areas in the eastern Mediterranean region and has been experiencing approximately N–S extension since, at least, latest Oligocene time. It forms part of Aegean-Anatolian extensional domain that includes western Turkey, Cycladic islands and part of the mainland Greece. The present-day configuration and different rates of active (back arc) extensional tectonics of the region (e.g., Le Pichon & Angelier, 1979; McKenzie, 1978; Şengör et al., 1984; Meulenkamp et al., 1988; Yılmaz et al., 2000; Gessner et al., 2013; Jolivet et al., 2015) result from combined effects of southward slab retreat (roll back) along the Aegean-Cyprian subduction zone and westward-southwestward escape of Anatolia (e.g., Le Pichon & Angelier, 1979; McKenzie, 1978; Şengör et al., 1984; Seyitoğlu & Scott, 1991; Meulenkamp et al., 1988; Jolivet et al., 1998, 2010a, b, 2013, 2015, 2019; Koçyiğit et al., 1999; Okay & Satır, 2000; Seyitoğlu et al., 2002, 2004; Yılmaz et al., , 2000; Bozkurt, 2001a, 2004, 2007; Bozkurt & Sözbilir, 2004; Catlos & Çemen, 2005; Ring & Collins, 2005; Thomson & Ring, 2006; Cawazza et al., 2008; Çiftçi & Bozkurt, 2008, 2009a, b, 2010; Bonev et al., 2009, 2015; Agostini

2

et al., 2010; Jolivet & Brun, 2010; Lecomte et al., 2010; Bozkurt et al., 2011; Şengör and Bozkurt, 2013; Philippon et al., 2014; Seyitoğlu & Işık, 2015; Menant et al., 2016; Bessiere et al., 2018; Rabillard et al., 2018; Roche et al., 2018, 2019).

In this model, Aegean (Hellenic) and Cyprus arcs are defined as active convergent plate boundary of the Anatolian and African plates. Despite of their importance, there is a long-lasting (for several decades) debate on the geometry and nature of Cyprian and Aegean arcs since their first description (e.g., McKenzie et al., 1970, 1972; Dewey et al., 1973, 1979; Smith et al., 1971; Woodside et al., 1977; Nur et al., 1978; Şengör et al., 1979; Oral et al., 1995; Vidal et al., 2000). In the geodynamic development process of the Aegean region, the Aegean arc system holds an important place. The western extension of the arc is marked by Ionic convergence between the Aegean lithosphere and the Ionian Basin. The eastern part of the Aegean Arc serves as transform fault (Le Pichon *et al.,* 1979) where several trenches (Ptolemy, Pliny, and Strabo trenches) are prominent along the eastern parts of the Arc (Jongsma et al., 1977) (Figures 1.2 and 1.3).

Although the Aegean subduction zone is the main actor of the Mediterranean tectonics, its kinematics is still not explained effectively. While several medium size earthquakes (Ms> 6) have occurred along the Aegean Arc at intermediate depths, only two large earthquakes with Mw> 8 have occurred in the last 2000 years (Becker & Meier, 2010; Papazachos et al., 1999; Shaw & Jackson, 2010). The lacking of large earthquakes at large subduction zone, along which rapid convergence takes place between African and Anatolian plates, is a big question waiting for enlightenment (Shaw & Jackson, 2010).

Furthermore, Aksu et al., (2004) published a map (compiled from Şengör & Yılmaz, 1981; Hancock & Barka, 1981; Jongsma et al., 1985, 1987; Dewey et al., 1986; Mascle et al., 2000; Zitter et al., 2003; Salamon et al., 200) of major structures in the Eastern Mediterrenean Sea (Figure 1.4); the authors pointed out that some of these structures are controversial. Nevertheless, several '*deformation zones*' such as the Misis-Kyrenia

3

Fault Zone, the Amanos-Larnaka Fault Zone and the Latakia-Tartus Ridge are considered as major structures of the Eastern Mediterranean and they are attributed to continuing convergence of the African and Anatolian plates (e.g., Aksu et al., 2005; Hall et al., 2004a).
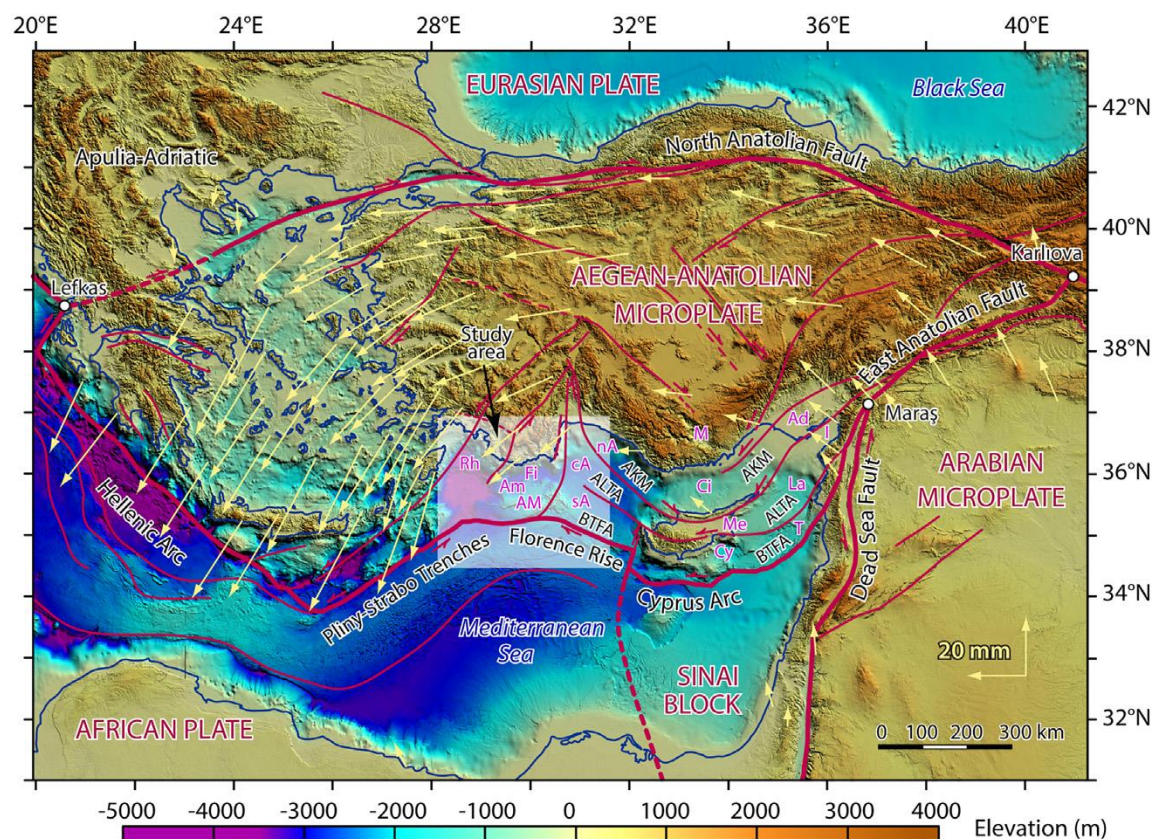


Figure 1.2. Simplified tectonic map of the eastern Mediterranean Sea and surrounding regions, showing Aegean (Hellenic) and Cyprus arcs along the margin between the African Plate and the Anatolian Plate (from Aksu et al., 2019). AKM, Aksu-Kyrenia-Misis fold-thrust belt; ALTA, Amanos-Latakia-Troodos-Antalya fold-thrust belt; BTFA, Bassit-Tartus-Florence Rise-Anaximander fold-thrust belt. Basins: Ad, Adana; Am, Anaximander; A, Antalya (n, north; c, central; s, south); Ci, Cilicia; Cy, Cyprus; Fi, Finike; I, Iskenderun; La, Latakia; M, Mut; Me, Mesaoria; Rh, Rhodes. Ridges/mountains: AM, Anaximander; T, Tartus.

Neotectonic features of eastern Mediterrenean are dominantly related to convergence between African Plate and Eurasian Plate at rate of ~10 mm/yr (McClusky et al., 2000; (Kahle et al., 2000; Reilinger et al., 2006, 2010; DeMets et al., 2010; Tiryakioğlu et al., 2013). Oceanic crust at the northern edge of African tectonic plate, possibly of Paleozoic age (Granot, 2016), subducts northwards beneath the the southern edge of the Eurasian Plate along Aegean (Hellenic) subduction zone (e.g., McKenzie, 1979;

4

Dewey & Şengör, 1979; Le Pichon et al., 1979; Chaumillon & Mascle, 1997) (Figure 1.5). The subduction zone therefore accommodates the convergence between the Africa in the south and Anatolia in the north; southward rollback of the subduction zone is considered as the main cause of N–S extension in the back region of Aegean Sea and western Anatolia. Several deep focus (100–150 km) earthquakes indicate that African oceanic crust subducts into the mantle (e.g., Caputo et al., 1970; Jackson & McKenzie, 1984; Hatzfeld & Martin, 1992; Hatzfeld, 1994).
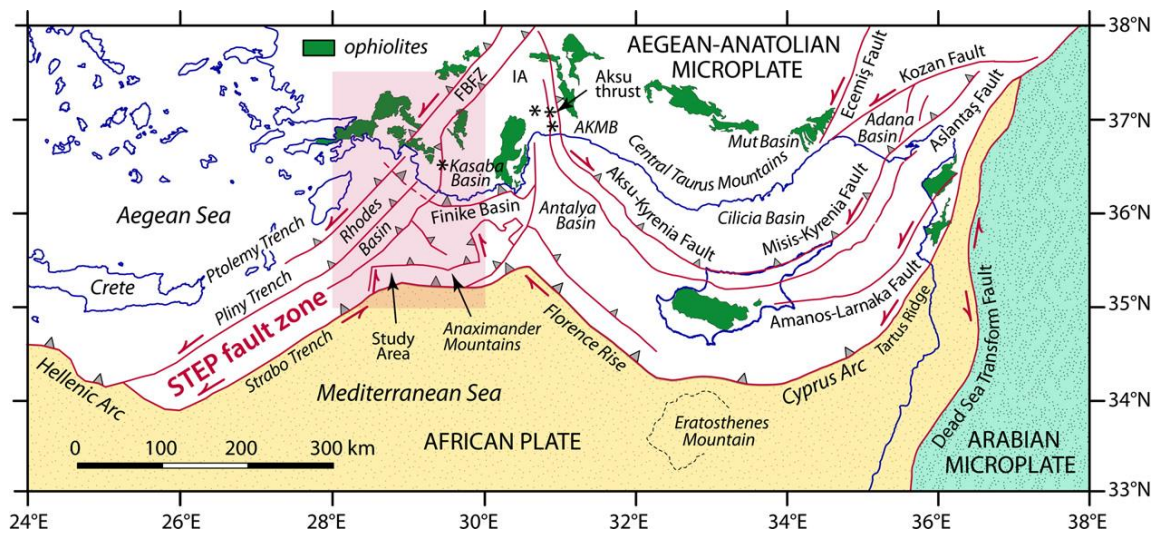


*Figure 1.3. Simplified tectonic map of the eastern Mediterranean Sea and surrounding regions, showing major plate/microplate boundaries, ophiolitic rocks and major tectonic elements. AKMB, Aksu, Köprüçay, Manavgat basins; FBFZ, Fethiye–Burdur Fault Zone; IA, Isparta Angle; STEP, Subduction Transform Edge Propagator *, Neogene–Quaternary volcanics. Half arrows indicate transform/strike–slip faults (from Hall et al., 2014a).*

In this scenario, relative differential motion of Aegean and Cyprus arcs is attributed to a tear (offset) along the subducting slab, termed the '*subduction transform edge propagator (STEP) fault*' – a high angle transfer zone to the trench that connects the two arcs (Wortel and Spakman, 2000; Govers & Wortel, 2005; Faccenna et al., 2006; van Hinsbergen et al., 2010; Biryol et al., 2011; Salaün et al., 2012; Özbakır et al., 2013; Hall et al., 2014a). STEP fault is described as continual tearing of (oceanic) lithosphere that marks the horizontal termination (lateral edges) of subduction zones and enables subduction to continue while adjacent lithosphere remains at the surface. Propagation of a tear along the edge of a subducting slab allows slab to retreat (roll

5

back) and facilitate back-arc extension while overriding lithosphere moves with the trench.
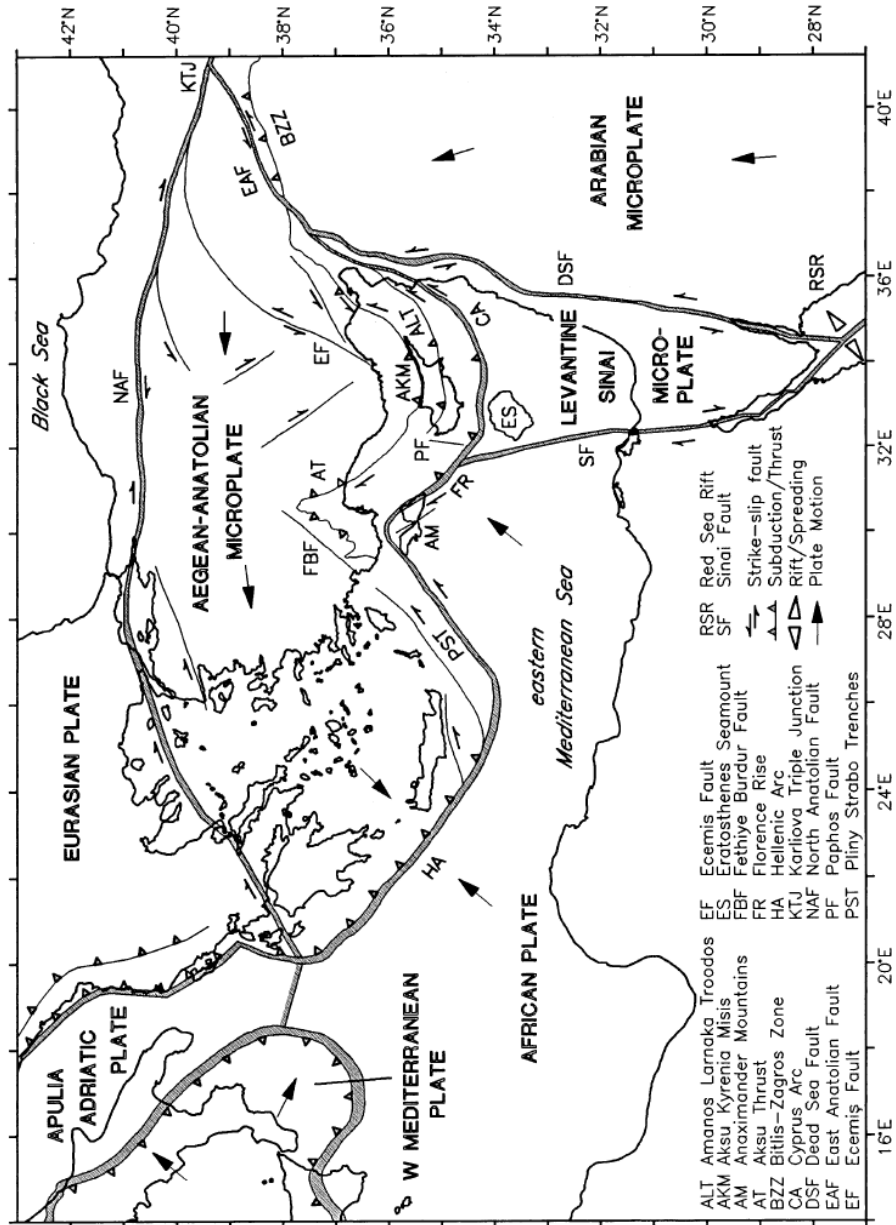


*Figure 1.4. Tectonic structures of eastern Mediterrenean Sea and surroundings region (from Aksu et al., 2005).*
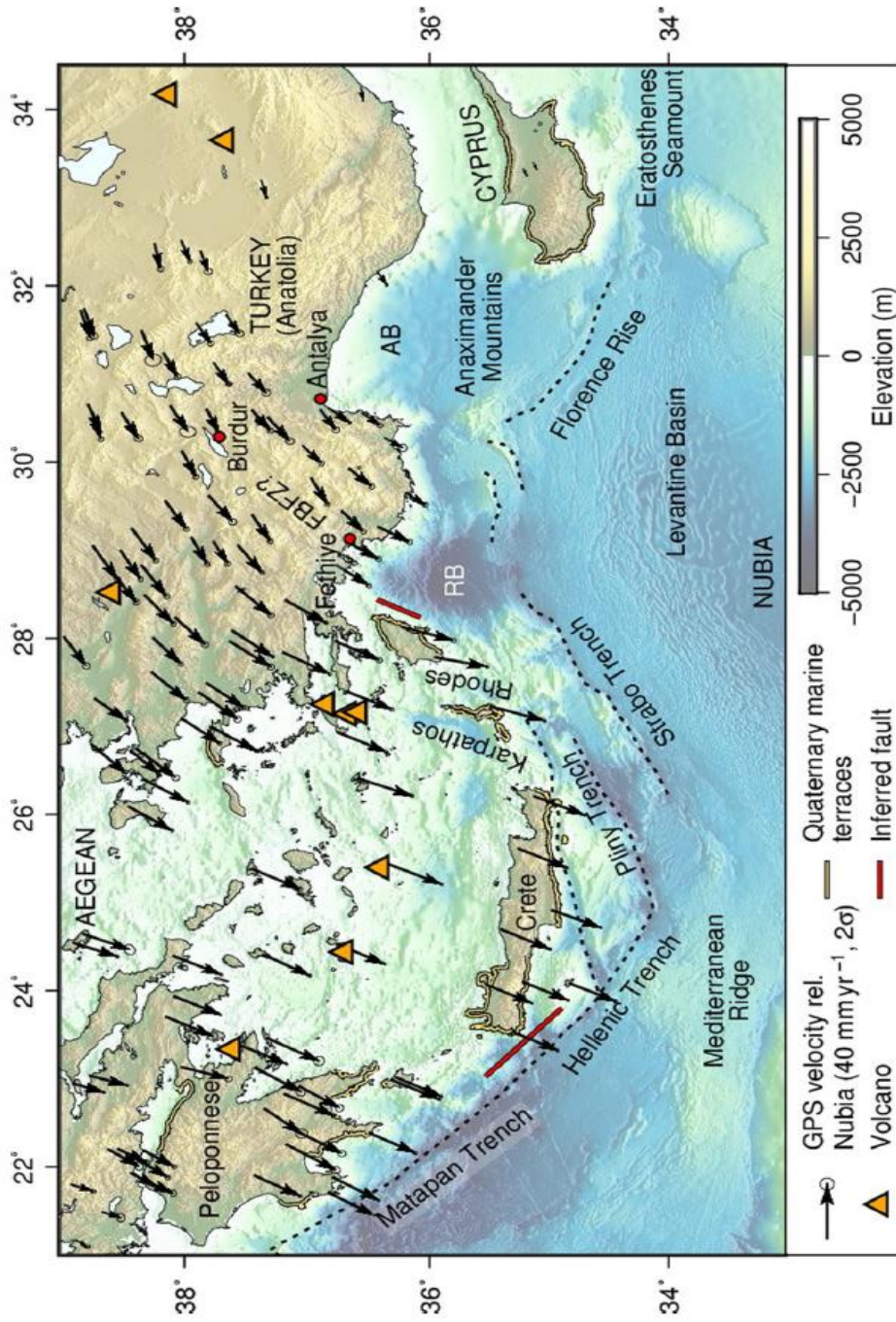
Figure 1.5. *Selected tectonic features and GPS velocities are indicated with black arrows (data of Reilinger et al., (2006). Yellow lines indicate uplifted Pliocene–Quaternary traces. Orange triangles demonstrate active volcanoes from Siebert & Simkin (2002). Thick red lines indicate large earthquakes Rhodes and Crete. 'RB', 'AB' 'FBFZ' refer to Rhodes Basin, Antalya Basin, Fethiye-Burdur Fault Zone, Topography is SRTM15 (Becker et al., 2009; Sandwell et al., 2014).*

7

The STEP fault thus forms the contact zone (weakness zone) between the overriding lithosphere and the adjacent non-subducted lithosphere. In this definition, STEP faults are not transform plate boundaries. Once formed, STEP faults continue to propagate through the landscape and may produce kilometer-scale major sedimentary basins (cf. Govers & Wortel, 2005; Baes et al., 2011; Nijholt & Govers, 2015). STEP faults also result in sharp changes in the lithospheric and crustal thickness and may trigger lateral and/or near-vertical mantle flow (Hidas et al., 2019).

Pliny-Strabo trench in the eastern Mediterranean is interpreted as surface expression of the STEP fault (here after named as Pliny-Strabo STEP fault zone) that connects the Aegean and Cyprean arcs and accommodates oblique Africa-Anatolia convergence (Figures 1.2 and 1.3; McKenzie, 1978a; Le Pichon & Angelier, 1979; Le Pichon et al., 1979; Leite & Mascle, 1982; Mascle et al., 1982, 1986; de Boorder et al., 1998; Huguen et al., 2001, 2006; Bohnhoff et al., 2005; Zachariasse et al., 2008; van Hinsbergen et al., 2010; Özbakır et al., 2013; Hall et al., 2009, 2014a, b; Aksu et al., 2009, 2019; Hall et al., 2009, 2014a, b; Shaw & Jackson, 2010; Ocakoğlu, 2012). It was first described, based on the kinematic model of 1957 Rhodes earthquake, by McKenzie (1978a), as a transform fault. Several papers about the results of marine geophysical studies, land studies, and first motions of recent earthquakes have been published; in these studies the Pliny-Strabo STEP fault zone is described as a ~50-km-wide, NE–SW-trending transpressional or sinistrial strike-slip fault zone that extends southwards into the Rhodes Basin (e.g., Le Pichon & Angelier, 1979; Woodsite et al., 2000; Zachariasse et al., 2008; Hall et al., 2009, 2014a, b; Shaw & Jackson, 2010; Özbakır et al., 2013; Aksu et al., 2019). Initiation age of the STEP fault zone is under discussion where claims range from 20 my to 4–5 my (e.g., ten Veen & Kleinspehn, 2002; Zitter et al., 2003; Zachariasse et al., 2008; Pe-Piper & Piper, 2007; van Hinsbergen et al., 2010; Le Pourhiet et al., 2012; Jolivet et al., 2013). The Pliny-Strabo STEP fault zone is interpreted to allow rollback of the Aegean subduction and back-arc extension of the Aegean to be detached from the deformation of the Cyprus Arc (Hall et al., 2014a). Upwelling asthenosphere (asthenospheric mantle window) below

western Anatolia (Dilek & Sandvol, 2009; van Hinsbergen et al., 2010; Biryol et al., 2011; Mutlu & Karabulut, 2011; Gessner et al., 2013, 2018; Kaymakcı et al., 2018) (Figure 1.6) is also attributed to tearing along the Pliny-Strabo STEP fault zone. Asthenospheric mantle flows vertically upwards and also westwards into the Aegean region, presumably produces a thermal load, ultimately causes overall high heat flow and high geothermal gradient in central western Anatolia (Gessner et al., 2018).
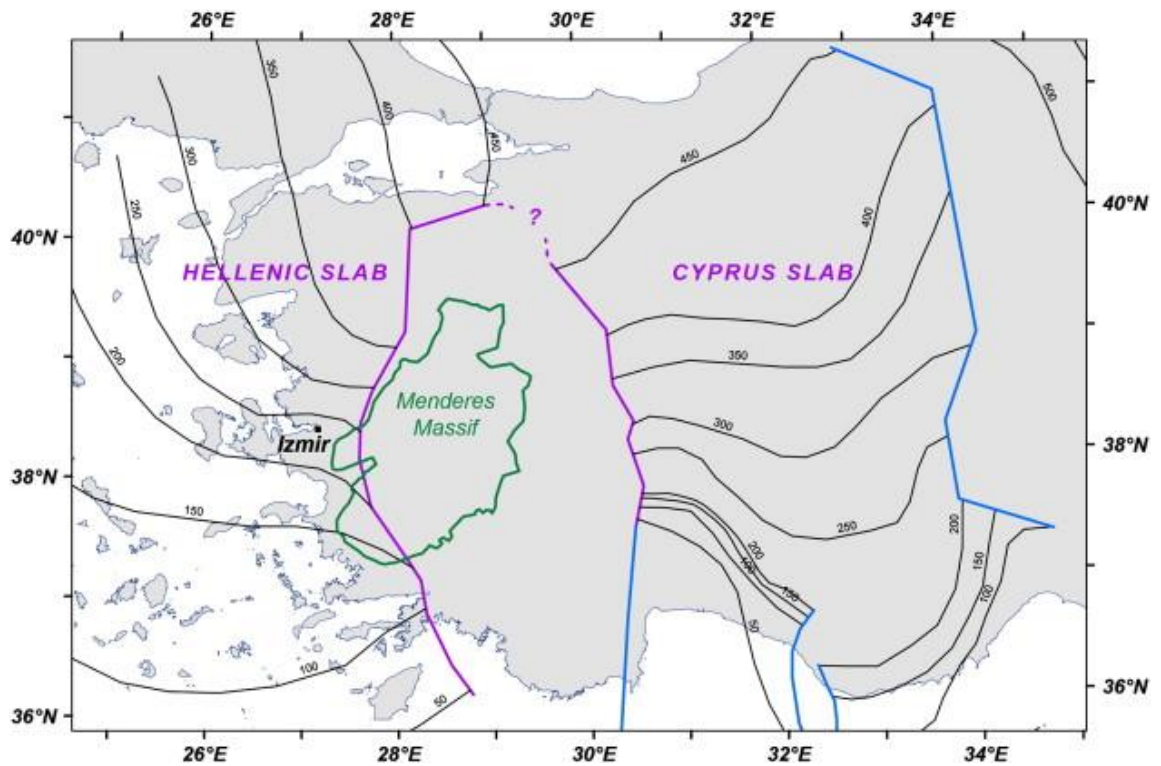


*Figure 1.6. Map showing the location of ca. 300 km wide 'asthenospheric window'; a slow wave speed anomaly that is commonly interpreted as a tear in the African plate (from Gessner et al., 2018).*

Monitoring the STEP fault in the northeast is difficult. Northeastern continuation of the Pliny-Strabo STEP fault zone on land is always disputed and formed the subject of controversies over the last decade. NNE–SSW structures of the Rhodes Basin is considered as the southwestward continuation of the STEP fault zone (Hall et al., 2009, 2014a). Fethiye-Burdur Fault Zone (FBFZ) forms one of the most important structural elements of southwest Anatolia and is interpreted as north-northeast prolongation of the Pliny-Strabo STEP fault zone on land (cf. Taymaz & Price 1992;

Barka & Reilinger 1997; Woodside et al., 2000; Huguen et al., 2001; Zitter et al., 2003; ten Veen, 2004; ten Veen et al., 2008; Aksu et al., 2009, 2019; Hall et al., 2009, 2014a; Ocakoğlu, 2012; Elitez & Yaltırak, 2014b; Elitez et al., 2015, 2016a, b, 2017, 2018a, b; Kaymakcı et al., 2018; Özkaptan et al., 2018). It is a NE–SW-trending broad fault zone (ca. 40–50 km wide) and forms a major boundary fault between western Anatolian extensional province in the west and relatively stable central Anatolia in the east; it also separates western Anatolia from the Isparta Angle (Barka et al., 1995; Eyidoğan & Barka 1996; Barka and Reilinger, 1997). Along most of its trace, the fault cuts through the southernmost part of the Lycian Nappes (Şenel, 1997a, b; Şenel & Bölükbaşı, 1997; Alçiçek et al., 2006; Alçiçek & ten Veen, 2008; ten Veen et al., 2009). Different terminology is proposed to describe the for the FBFZ: Burdur Fault, Fethiye-Burdur Fault, Fethiye-Burdur Fault Zone, Burdur-Fethiye Fault Zone (e.g., Price & Scott, 1994; Barka et al., 1995; Eyidoğan & Barka, 1996; Akyüz & Altunel, 2001; Barka & Reilinger, 1997; Glover & Robertson, 1998; ten Veen, 2004; Verhaert et al., 2004, 2006; Alçiçek et al., 2006; Bozcu et al., 2007; ten Veen et al., 2008; Över et al., 2010, 2013; Hall et al., 2014a, b; Aksu et al., 2019) or Burdur-Fethiye Shear Zone (Elitez & Yaltırak, 2014, 2016; Hall et al., 2014a, b; Elitez et al., 2015, 2016a, b, 2017, 2018a, b).

The linkage of the Pliny-Strabo STEP fault zone and the Fethiye-Burdur Fault Zone has always been debated. Ocakoğlu (2012) attempted, based on multi-beam bathymetric data and shallow reflection seismic profiles in the region of Fethiye and Marmaris bays, to provide first insight into, and map, possible fault linkages between two major structures. Several NE–SW-trending transtensional and normal faults below Marmaris Bay, and transpressional faults below Fethiye Bay are mapped. Faults below Fethiye Bay are interpreted to represent the northeastern extension of the Pliny-Strabo STEP fault zone while faults of the Marmaris Bay are associated with the FBFZ. The author also commented on the relationship between the STEP fault zone and the FBFZ as a '*missing link*'.

Similarly, Hall et al. (2014a) interpreted two seismic profiles running parallel to the present-day coastline between Dalyan River and Finike Basin (Figure 1.7). They concluded that many NE–SW-striking Pliocene–Quaternary high-angle faults with extensional separations mapped offshere clearly link with the similarly trending strike-slip faults onland in the Eşen Valley, and that FBFZ represents onland continuum of the of the STEP fault zone into the upper (Anatolian) plate. In this model, the STEP fault zone is interpeted as a crustal-scale a flower structure.

The FBFZ is originally described as a left-lateral fault (with normal component) that runs in the area between Burdur in the north and Fethiye in the south (Figure 1.8; Dumont et al., 1979; Barka et al., 1995; Eyidoğan & Barka 1996; Barka et al., 1997; Reilinger et al., 2010) but others claim that the STEP fault is linked to Eşen Fault along the eastern margin of the Eşen Çay Basin (Figure 1.9; Alçiçek, 2007; ten Veen, 2004; ten Veen et al., 2009).

Recently, it is argued that the FBFZ is not a major single fault or a narrow fault zone but a NE–SW-trending wide (75–90 km) sinistral transtensional zone that runs, for about 300 km, from Şuhut-Çay to the northeast to Sarıgerme-Gelemiş on land and to the Pliny–Strabo STEP fault zone in the southwest (Figures 1.10 and 1.11); it is therefore renamed as the Burdur-Fethiye Shear Zone that is composed of several NE–SW-striking faults (1- to 10-km-long) of normal, sinistral and oblique character (BFSZ, Elitez & Yaltırak, 2014; Hall et al., 2014a, b; Elitez et al., 2015, 2016a, b, 2017, 2018a, b). The shear zone is not a thoroughgoing structure but has ca. 20 km sinistral offset (a bend along strike), some of which may be taken up by the Gökova-Yeşilüzümlü fault zone (Figure 11). The latter is interpreted as a prominent structural element of the SW Turkey and is described to a major WNW–ESE-striking sinistral fault zone of numerous en-échelon normal faults; the fault zone clearly transects the NE–SW-striking basin-bounding strike-slip faults of the FBFZ (Hall et al., 2014a).
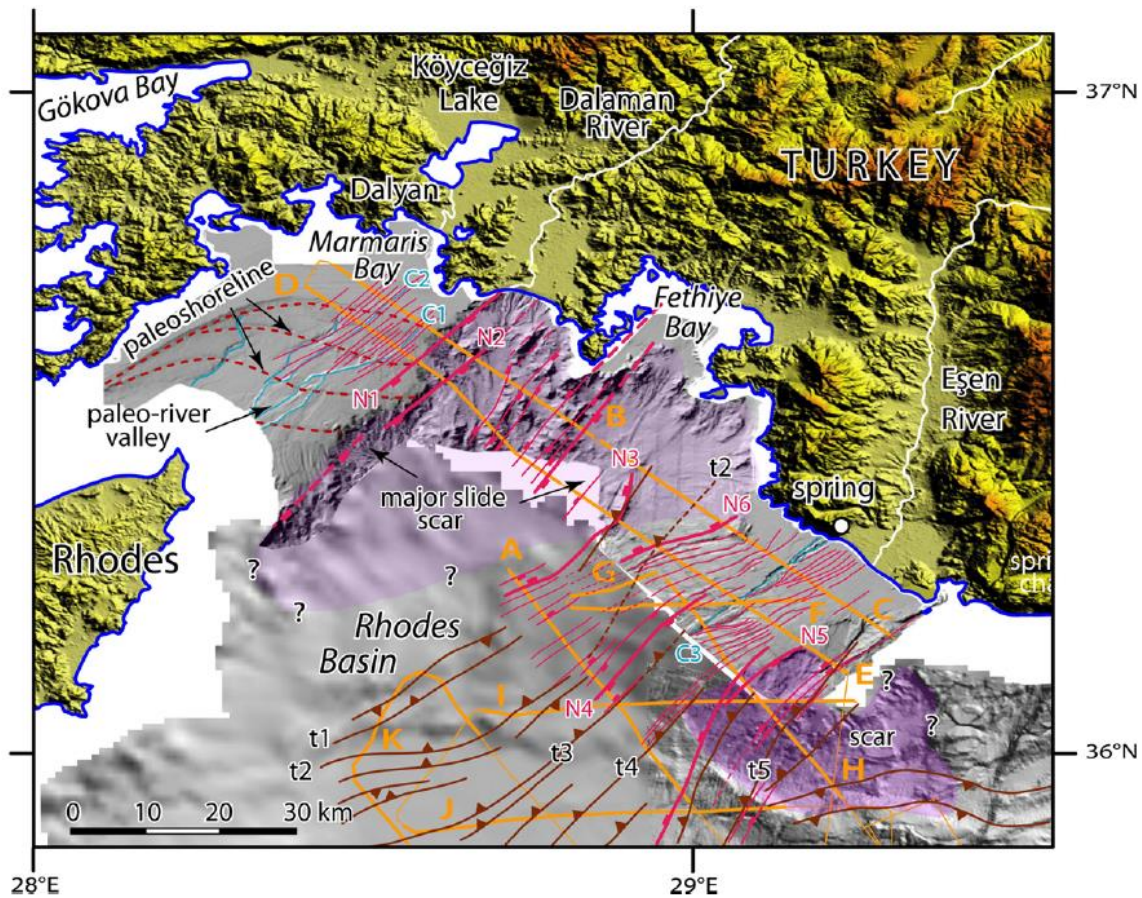
*Figure 1.7. Pliocene–Quaternary tectonic map of the Rhodes Basin and environs, showing the distribution of major thrust and normal faults (ticks on hanging wall). N1–N6, normal faults; t1–t5, thrust faults (from Hall et al., 2014a).*

In a recent paleomagnetic work done by Kaymakcı et al. (2018), the results of more than 200 samples from SW Anatolia and available paleomagnetic data in the literature are combined to identify three main rotation domainst in the area between subducted northern edge of the African Oceanic lithosphere and overriding south Anatolian plate (Figure 1.12): two domains of counter-clockwise rotation in the south and a domain of clockwise rotation in the north. The authors claimed that NW–SE-striking Acıpayam Transfer Zone form the boundary between two domains of counter-clockwise rotation and that Pliny-Strabo STEP fault do not propagate into the overriding plate in the SW Anatolia and paleomagnetic evidences does not support existence of Fethiye-Burdur Fault/Shear Zone (Kaymakçı et al., 2018).
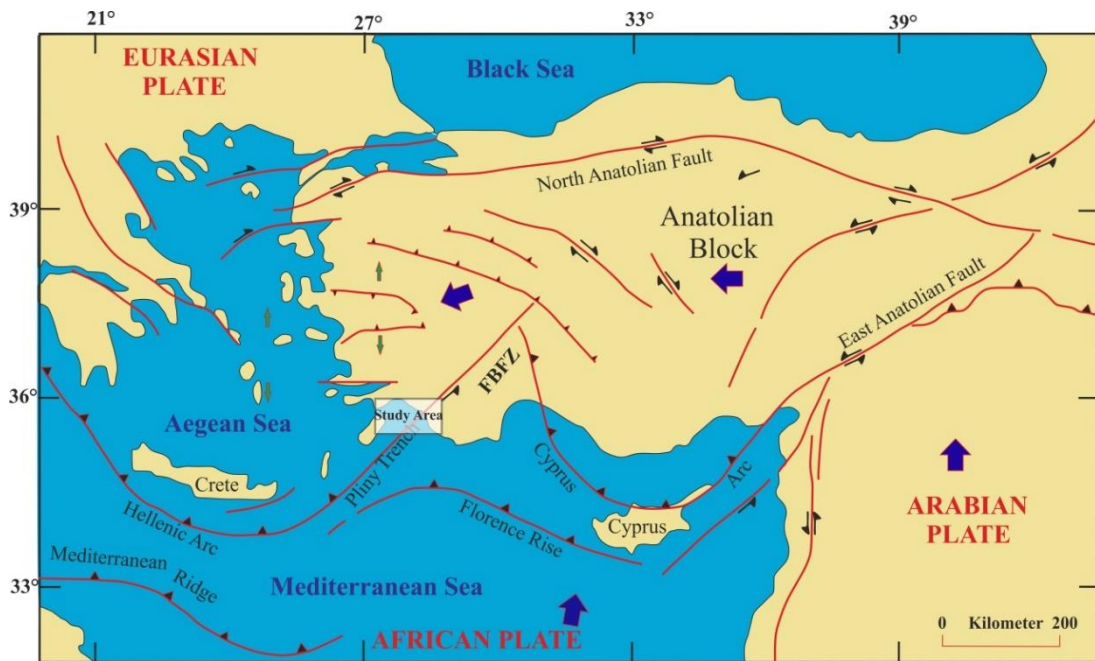
*Figure 1.8. A simplified map showing the Fethiye-Burdur fault zone (FBFZ) in the neotectonic framework of Turkey and surrounding areas (modified from Barka et al., 1995; Reilinger et al., 2010). Redrawn from Aksoy & Aksarı (2016).*

The long-standing tectonic activity of the Pliny-Strabo STEP fault zone and Fethiye-Burdur Fault Zone is well illustrated by several historical (1500 and 1800 A.D.) and instrumental earthquakes (e.g., 1971 May 12 Burdur earthquake) (Ambraseys, 1962; Taymaz & Price, 1992; Ambraseys et al., 1994; Ambraseys & Finkel, 1995; Akyüz & Altunel, 2001; Benetatos et al., 2004; Tohon et al., 2006; Yolsal et al., 2007; Karabacak, 2011). Possible kinematic relationship between Fethiye-Burdur Fault Zone and Aegean Arc is investigated by focal mechanism solution of major earthquakes (Figure 1.13; Canbay, 2009). The similarity of focal mechanism solution between two earthquakes (24.04.1957 M= 6.8 and 30.01.1964 M= 5.2 events) occurred in southwest of Fethiye Bay and 25.04.1957 M= 7.2 event placed at northwest of the Aegean Arc is considered to suggest that left-lateral strike-slip faulting occurred at left wing of Aegean Arc link the southern part of the FBFZ. The moderate to high tectonic activity of the Fethiye-Burdur Fault Zone is also indicated by several geomorphological indices within the Burdur and Yarışlı basins (Coşkuner et al., 2019).

13

*Figure 1.9. Active fault map of Eşen Fault from 1/250.0000 scale Active Fault Map of Turkey published by MTA (from Emre et al., 2013).*
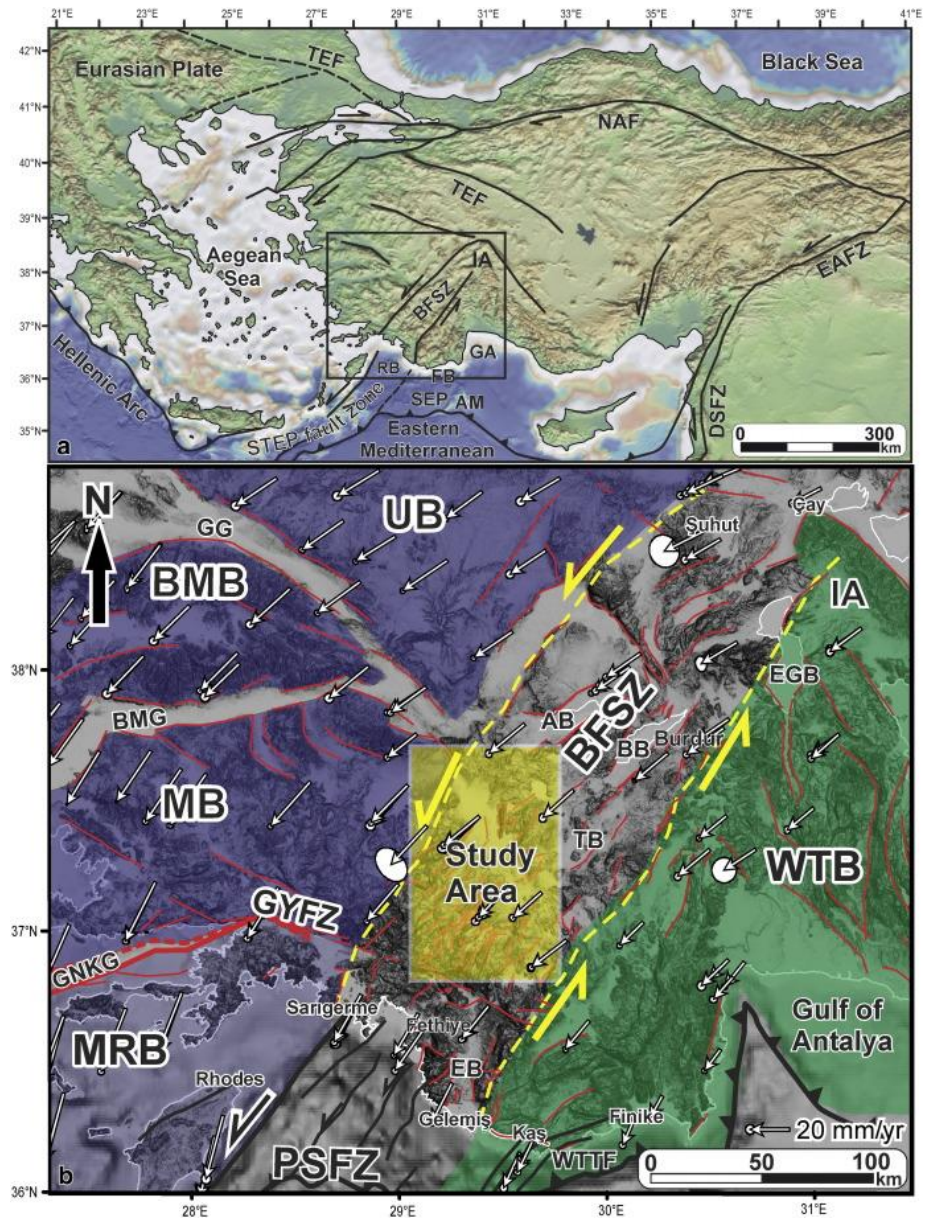
*Figure 1.10. (a) Simplified tectonic map of Turkey. TEF, Thrace-Eskişehir Fault; NAF, North Anatolian Transform Fault; EAFZ, East Anatolian Fault Zone; DSFZ, Dead Sea Fault Zone; IA, Isparta Angle; BFSZ, Burdur-Fethiye Shear Zone; RB, Rhodes Basin; GA, Gulf of Antalya; FB, Finike Basin; AM, Anaximander Mountain; SEP, Sırrı Erinç Plateau. Rectangle indicates the location of Figure 1b. (b) Regional fault map of southwestern Anatolia. Dark-blue region denotes the NE−SW extensional domain (MRB, Marmaris-Rhodes Block; MB, Menderes Block; BMB, Büyük Menderes Block; UB, Uşak Block; GG,Gediz Graben; BMG, Büyük Menderes Graben; GNKG, Gökova-Nisyros-Karpathos Graben). Green region denotes the NNE−SSW compressional domain (WTB, Western Taurides Block; IA, Isparta Angle; WTTF, Western Taurides Thrust Fault). BFSZ, Burdur-Fethiye Shear Zone; PSFZ, Pliny-Strabo Fault Zone; GYFZ, Gökova-Yeşilüzümlü Fault Zone; AB, Acıgöl Basin; BB, Burdur Basin; TB, Tefenni Basin; EGB, Eğirdir Basin; EB, Eşen Basin (from Elitez & Yaltırak, 2016a).*

15
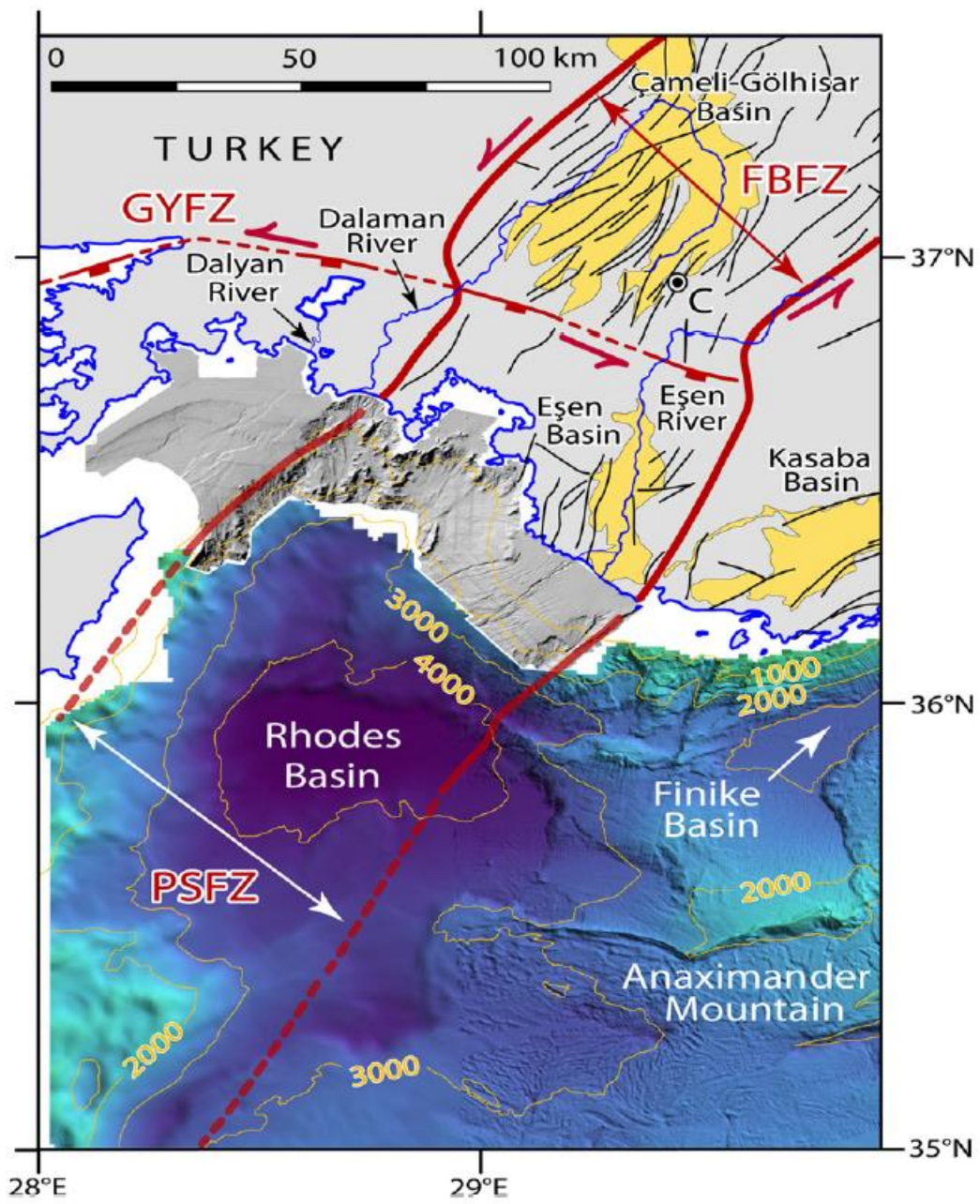
*Figure 1.11. Structural map of SW Anatolia showing the relationship between the Burdur Fethiye Fault Zone (FBFZ) and Gökova–Yeşilüzümlü fault zone (GYFZ). C, ancient town of Cibyra; PSFZ, Pliny-Strabo fault zone (from Hall et al., 2014a).*

16
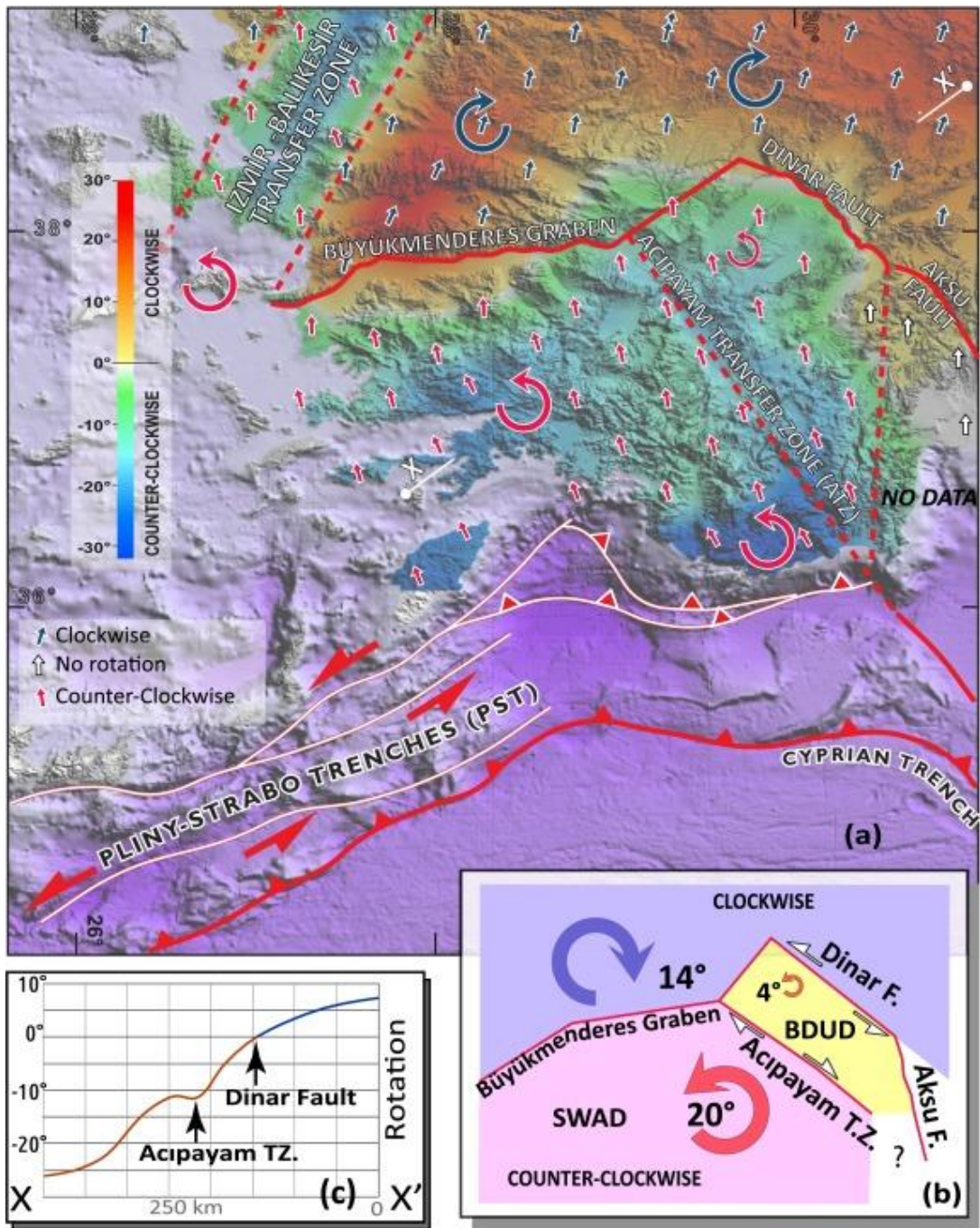
*Figure 1.12. (a) Simplified map that indicate tectonic features and rotational blocks in SW Anatolia; (b) Cross section X–X'; (c) simplified map for rotational block and amount from (Kaymakçı et al., 2018).*

17
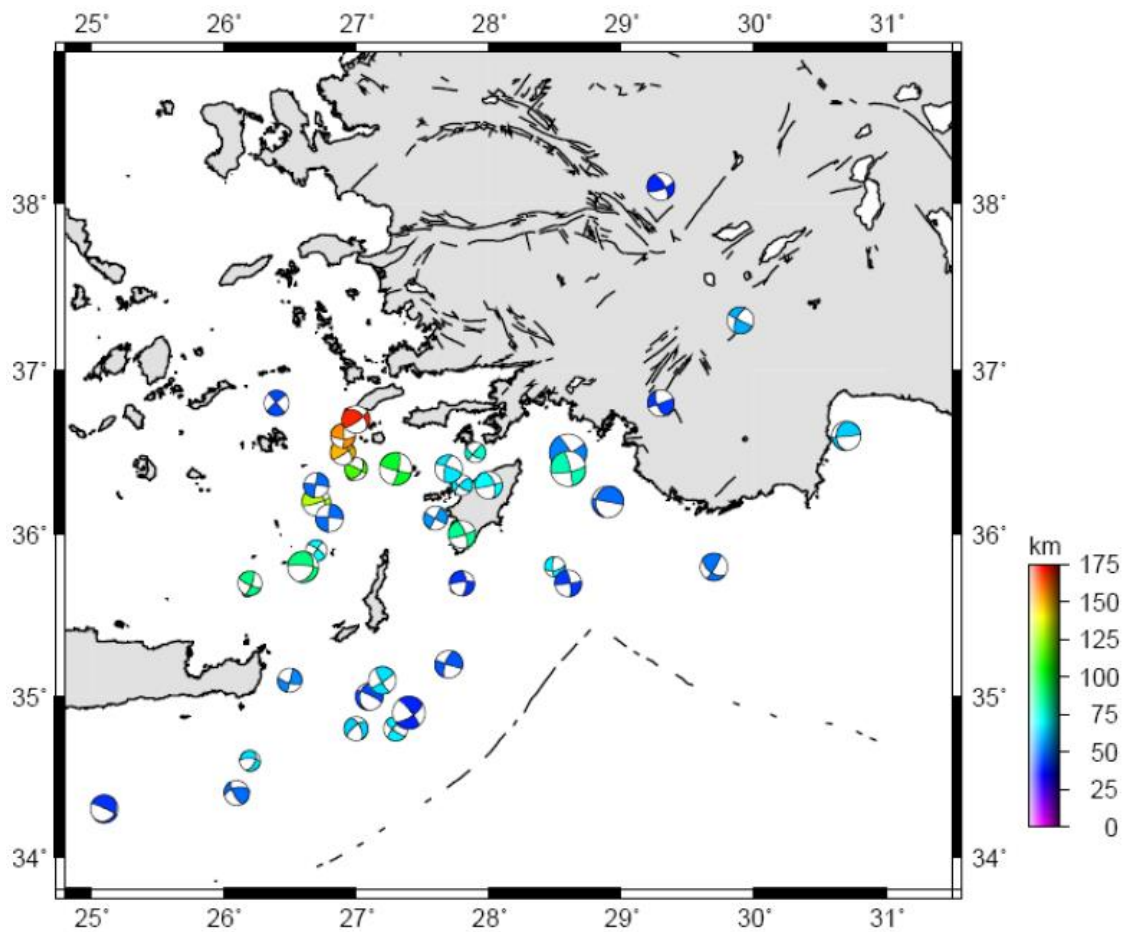
*Figure 1.13. Major earthquakes focal mechanism solution eastern Mediterranean region (from Canbay, 2009). Crossbar at the right indicates depth of the earthquakes.*

Although the FBFZ has been studied intensely during the last two decades; presence, geometry and kinematics (strike-slip nature) of the fault zone and its relation/linkage to the Pliny-Strabo STEP fault zone have been the subject of intense discussion during the last decade. GPS-based geodetic studies suggest a slip rate of 1.5–2 cm/yr along the BFSZ (Barka & Reilinger, 1997; Kahle et al., 2000; Reilinger et al., 2006, 2010; DeMets et al., 2010; Tiryakioğlu et al., 2013), there is however no strong evidence for considerable amount of sinistral strike-slip offset (cf. Hall et al., 2014a). Accordingly, Hall et al. (2014a) argued that the BFSZ comprises several smaller dominantly normal faults and that it is unlikely for the BFSZ to accommodate 60 km of sinistral

displacement required in models by van Hinsbergen (2010) and van Hinsbergen et al., (2010a).

It is also claimed that kinematic evidence (fault slip data, earthquake moment tensor solutions, and GPS velocities) in favor of sinistral FBFZ (Barka and Reilinger, 1997; Elitez et al., 2016a, b) is rather consistent with extensional nature of the FBFZ and that there is no significant evidence for strike-slip faulting (Gürer et al., 2004; Alçiçek et al., 2005, 2013; Alçiçek & Ten Veen, 2008; Över et al., 2010; Alçiçek 2015, 2018; Kaymakcı et al., 2018; Özkaptan et al., 2018). It is also concluded, based on paleomagnetic analyses of several samples and kinematic analyses of several fault planes from SW Anatolia, that the Pliny-Strabo STEP fault zone have not propagated into the overriding plate as a shear zone and that there is no evidence to support the presence of alleged Fethiye–Burdur Fault Zone, and its existence is dubious (quoted from Kaymakcı et al., 2018). This is consistent with earlier contention that the FBFZ is not a transform fault and that the dominant motion is dip-slip normal, not sinistral (e.g., Koçyiğit 2000; Alçiçek et al., 2006). Furthermore, earthquake focal mechanism solution does not indicate strike-slip motion for BFFZ (e.g., Taymaz & Price 1992; Shaw & Jackson, 2010). More recent study of the Burdur Basin, based on rock magnetic experiments, Anisotropy of Magnetic Susceptibility (AMS) measurements, magnetostratigraphy and kinematic analyses of fault-slip data, shows that SW Anatolia is dominated by NW−SE-directed extensional forces that cause to form NE−SW-striking normal faults from late Miocene to Recent (Özkaptan et al., 2018).

The seismic activity within the so-called Fethiye-Burdur Shear Zone (FBSZ) still continues as indicated by recent earthquakes in Acıpayam (Denizli) province. Focal mechanism solutions for this event indicate an almost pure normal faulting; the results are not compatible with sinistral nature of the FBSZ (Figure 1.14) and supports the contention that the dominant motion is dip-slip normal, not sinistral (e.g., Koçyiğit 2000; Alçiçek et al., 2006; Kaymakcı et al., 2018; Özkaptan et al., 2018).
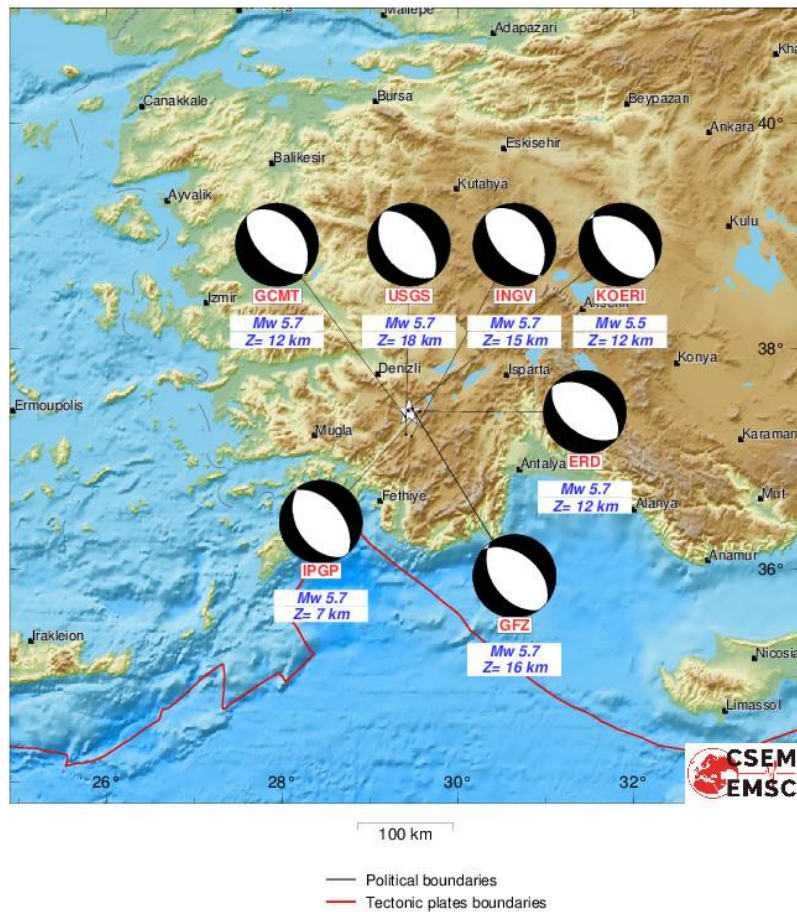
*Figure 1.14. Focal mechanism solutions of the Acıpayam (Denizli) earthquake; Magnitude: 5.5 (Mw), Epicenter Coordinates: 37.4401N, 29.4335E; Earthquake Depth: 10.8 km. Earthquake Date and Time: 2019-03-20 06:34:27 (GMT) from* **https://www.emsc-csem.org/Earthquake/earthquake.php?id=752096#**

## 1.2. Purpose and Scope

Active tectonics (neotectonics) of Anatolia is dominated by convergence of the Arabian and African (Nubia) plates with the Eurasian Plate (McKenzie, 1972; Dewey & Şengör, 1979; Dewey et al., 1986; Le Pichon & Kreemer, 2010). The Aegean (Hellenic) and Cyprus arcs represent the convergent boundary between the Anatolia in the north and Africa in the South (Figures 1.1–1.3). Offset along Aegean subduction zone (relative differential motion of Aegean and Cyprus arcs) correspond to NE–SW-trending Pliny-Strabo STEP fault zone (cf. Hall et al., 2014a). The Fethiye-Burdur Fault Zone (FBFZ) on land is considered as northeastern prolongation of the STEP fault. The continuum and linkage of the STEP fault zone and the FBFZ have always

20

been the subject of controversy among researchers. The presence and sinistral nature of the FBFZ have also been debated by many researchers and formed the subject of several recent '*comment and reply*' papers (see Section 1.1 for details).

Although there are several structural works along the Fethiye-Burdur Fault Zone on land, less is known about the presence, nature and linkage of offshore structures along Mediterranean coastline (Ocakoğlu, 2012; Hall et al., 2014a). Present study therefore aims to: (i) address existing controversies (as outlined above), (ii) shed light on the structural features in the northeastern part of the Pliny-Strabo STEP fault zone and (iii) enlighten tectonic evolution of the STEP fault zone and the Anatolian Plate.

In order to address the main objectives of this research, a key area along Mediterranean coastline between Dalyan and Fethiye bays (Figure 1.15) is chosen and the following studies were carried out:

**(1)** structural interpretation of seven 2D seismic lines (360 km long, 120-96 channel seismic data) collected by the General Directorate of Mineral Research and Exploration of Turkey (MTA) Sismik-1 Research Vessel in 1996 and 1997. The seismic data is processed at MTA and the software PETREL E@P is used for seismic interpretation to analyse main structural elements and stratigraphical framework of the study area; this provides furher information to better understand the region's overall structural framework (see Chapter 3 for more information and the results);

**(2)** focal mechanism solution of six (6) major shallow earthquakes occurred in the study area; moment tensor inversion solution of these events provide important data about the source fault characteristics (see Chapter 4 for more information and the results);

▪ integration of the main results from seismic interpretation and focal mechanism solution in order to define event (earthquake) and fault correlation;

▪ classification of the interpreted structural elements and discussion of the main conclusions (see Chapter 5 for more information).



*Figure 1.15. Google Earth image showing location of the study area.*

## 1.3. Study Area

Geographically, the study area is located in southwest Anatolia in the area between Fethiye Bay in the east and Dalyan Bay in the west along the Mediterranean Sea coastline (Figure 1.15). Geologically, Çameli-Gölhisar, Kasaba, Eşen and Gökova basins line in the north of, Fethiye and Finike basins within, and Rhodes Basin in the southwest of, the study area (Figures 1.7 and 1.11).

# CHAPTER 2

# DATA AND METHOD

In order to address the main objectives of this research, two types of dataset have been used to interpret and map the structural features in the study area.

Seismic waveforms generated by an earthquake and recorded by local and global seismic networks are analyzed and evaluated to calculate focal mechanism solution by using moment tensor inversion method. This method therefore provides valuable information about origin time, epicenter location, focal depth, magnitude (Mw), and seismic moment (Mo) for a given earthquake. Reasonable focal mechanism (beachball) diagrams are produced where fault-plane solutions (geometry and sense of slip of the fault) are also resolved.

The recognition of geological structures within the waters of Mediterranean Sea in the area between Dalyan Bay in the west and Finike Bay in the east is largely based on the structural interpretation of ca. 352-km-long 2D marine seismic data collected by MTA Sismik-1 in 1996-1997. Seismic data is processed by using SeisSpace ProMAX seismic software at MTA Marine Data Processing Laboratory. After data processing, stratigraphic horizons are picked and finally faults are interpreted with Schlumberger's Petrel E@P.

The detail information about the different methods employed will be provided in the following subsections.

## 2.1. Moment Tensor Inversion Method

Moment tensor is a mathematical description of seismic source that depends on wave propagation, Earth Model and synthetic seismograms. Moment tensor solution method is used for determination of fault type that caused an earthquake. Moment magnitude (Mw), Seismic Moment (Mo) and data for seismic source process are also obtained by this method. Least square fitting of amplitude and/or waveform data can be derived from seismograms moment tensor components (Dahm, 1996).

Inversion analysis of seismic waveforms recorded by local and global seismic networks lead to estimate moment tensor solution (Dziewonski et al., 1981; Kikuchi & Kanamori, 1991; Kawakatsu, 1995). Amplitude data for mutual ray path from various clustered seismic sources has been used for relative moment tensor inversion method. For moment tensor inversion method, some assumptions, for instance station velocity structure, are needed (Dahm, 1993 in Dahm, 1996).

Inversion of Green's function of surface-wave data supplied by earthquake clusters is described by Patton (1980). By using radiation pattern of one reference event, Green's function can be estimated from seismograms (Dahm, 1993 in Dahm, 1996). By using acquired Green's functions, radiation patterns of different earthquake from the same source area are studied by several researches (e.g., Strelitz, 1980; Oncescu, 1986; Oncescu & Trifu, 1987).

Main difficulties of Patton (1980) and Strelitz (1980) approaches are about their solution method, which is largely based on precise knowledge of radiation pattern of a reference event. Radiation patterns error may cause two-sided moment tensor solution for other events and it is resulted in remarkable deviations from double couple radiation pattern (Dahm, 1993 in Dahm, 1996). This problem can be solved by using non-double-couple components (cf. Vasco, 1990; Kawakatsu, 1991; Kuge & Kawakatsu, 1992; Foulger & Julian, 1993).

24

## 2.1.1. Application of Moment Tensor Inversion Method

Software for moment tensor inversion is prepared by Prof. Robert B. Hermann from Natural Sciences Department of Earth and Atmospheric Sciences at Saint Louis University and it is based on Linux operating system. This software has following paths used for calculations.

Moment tensor inversion method has a 'to-do-list' of eight steps, which are performed by software as indicated in Figure 2.1. *First step* involves selection of event and related seismic stations. Mostly, choosing nearest seismic stations provides good data quality and accordingly better solution(s). *Second step* is about gathering and selecting the data from seismic stations; it implements election and elimination of bad quality data recorded at seismic stations. Third and fourth stages are about the quality control of both the data and related stations. *Third step* requires filtering of seismic stations; stations presenting poor quality data is determined and then avoided in the subsequent stages. In the *Fourth stage*, data is filtered by using band pass filter to eliminate pointless data in waveform. Processing the data by the software forms the main theme of the *fifth stage*. *Sixth stage* involves evaluation of the results. If the best fit ratio is fulfilling, there is no need for the *seventh step*; this stage requires improvement, optimization and reprocessing of the results to obtain the best fit solution(s). Finally, moment inversion method provides the best fit solution for a given event. It is important to emphasize that all these steps at the flow chart (Figure 2.1) should carefully be fulfilled to find the best solution for a given earthquake. Because of their occurrence rate, moment tensor solution of middle-size earthquakes needs to be used for understanding of stress field and faulting system in regional aspect.

The first step of the moment tensor inversion method is about selecting events (earthquakes) and observer seismic stations. Selection of the closest seismic record stations always provides more accurate solutions for given events. Thus, event-data supplied by seismic stations settled near and/or at the study area are selected (Figure 2.2) for further analyses.

25
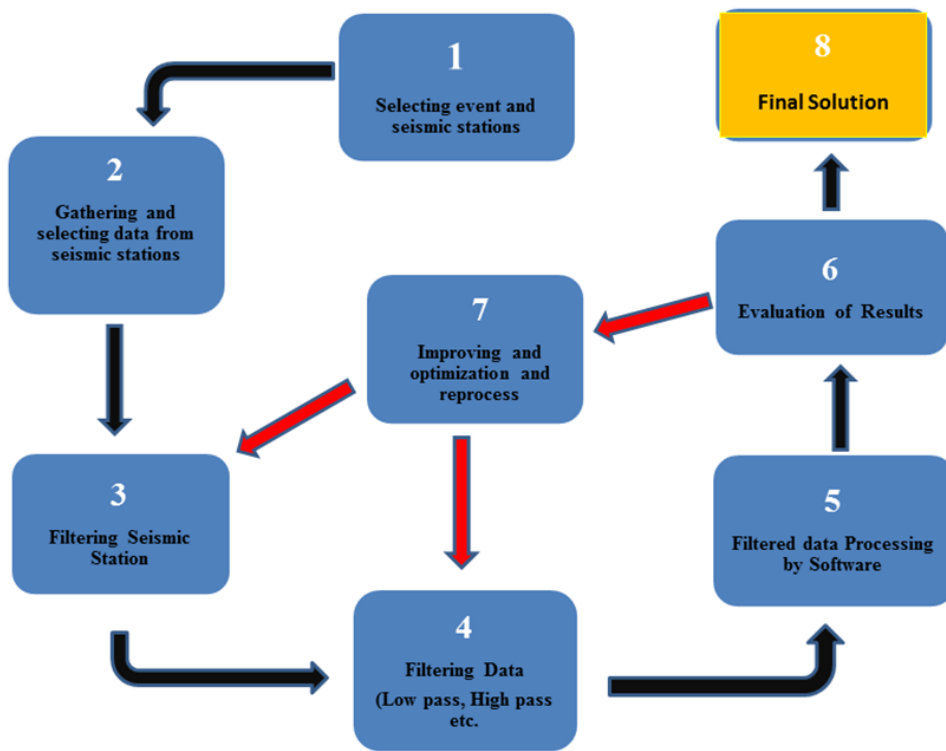
*Figure 2.1. Figure illustrating flow chart of moment tensor inversion method. Compiled from Hermann (2015) tutorial.*
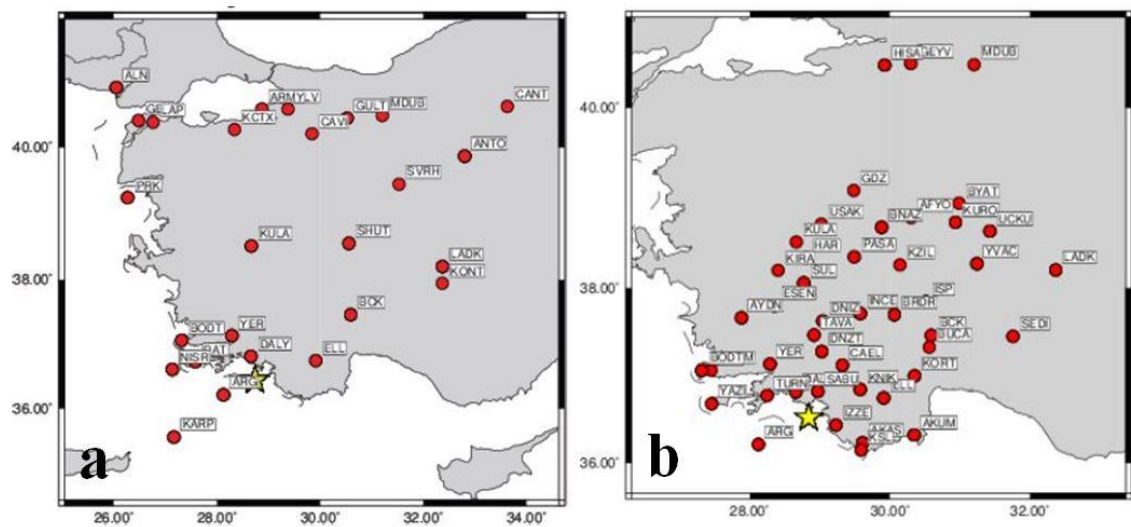


*Figure 2.2. Seismic stations that are used for moment tensor inversion method solution for sampled events in the study area. Seismic station locations used for solving (a) 2018/09/12 (18:13:26) event and (b) 2019/04/15 (17:42:25) event. These figures are produced by using Hermann (2015) software.*

Filtering seismic station data forms important part of the process: data quality must be checked and examined in detail. If the data supplied by seismic stations have not enough quality and accuracy, it should be eliminated by user; otherwise this may lead to wrong calculation for the final solution. The seismic data used for moment tensor inversion method contains BHZ and HHZ channels from broadband sensors and the HNZ sensor from an accelerometer (Figure 2.3; Herrmann, 2015).
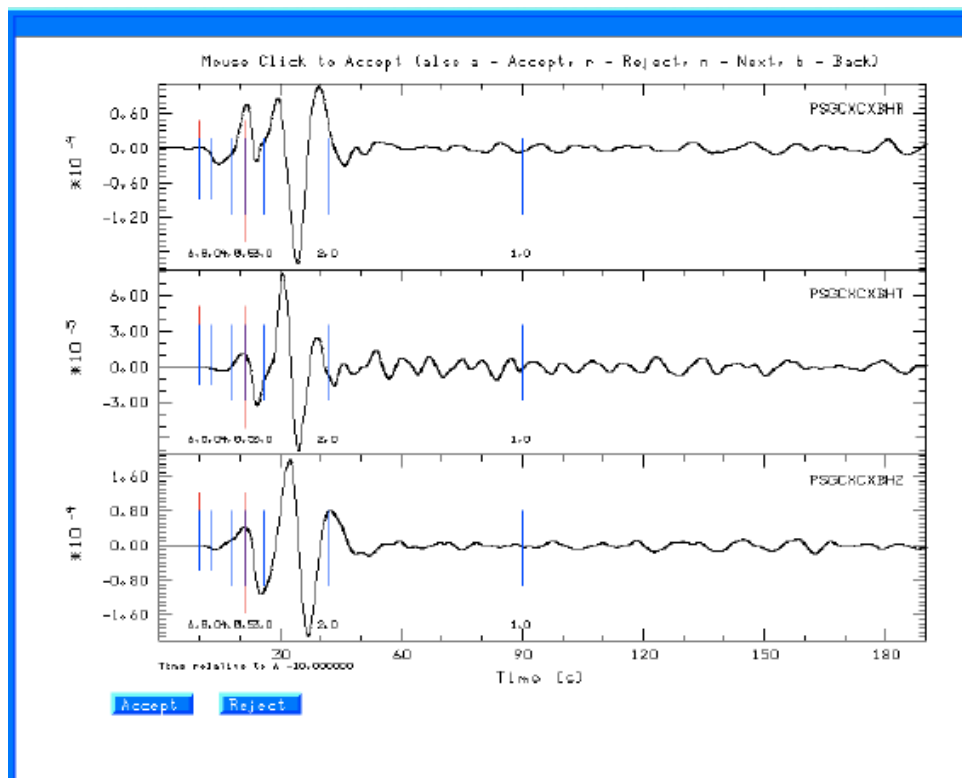


*Figure 2.3. Filtering process of seismic stations data that contains components of events from Hermann (2015) software.*

Filtering good quality data from seismic stations can be done by using low and/or high filter band pass methods. These methods are placed in the script name 'Do'. This script will get raw waveform data from seismic stations and deconvolve the data to ground velocity in units of m/s, rotate to vertical, radial and transverse components, place theoretical P- and S-wave first arrival times into the Sac file headers using the velocity model, and then select those waveforms at short distance for quality control. Checking for the same P-wave polarity on the vertical and radial component, little or no P-wave

on the transverse, and Rayleigh wave particle motion on vertical and radial axis at great distance is highly required because this process may help to identify any signal in the presence of noise (Figure 2.3).

Band pass filter is implemented for event data to supply more accuracy for solution. For example, low band filter pass 0.04 and high band filter pass 0.06 can be applied to the data; thus program only use data between 0.04 and 0.06. For filtered data processing, the software uses short distance stations' data, which contains good traces to define depth, focal mechanism, seismic moment (Mo) of event. In order to find best solution, software needs to use well-determined velocity model for Green's functions, high quality signal.

The program wvfgrd96 is used with good traces observed at short distance to determine the focal mechanism, depth and seismic moment (Mo) of a given event. This technique requires a high quality signal and well-determined velocity model for the Green's functions. To the extent that quality data is available, this type of mechanism should be preferred over the radiation pattern technique which requires the separate step of defining the pressure and tension quadrants and the correct strike. Software generates the best fitting source depth, strike and rake angles, magnitude (Mw) and gives the best solution in a table (Table 2.1). The best solution has the largest value for the fit. The software therefore accepts the best solution, whichever gives the largest fit value.

For example, moment tensor inversion methods supply the highest best fit value of 0.77 for 2012/06/25 (13:05:28) dated event in the study area; where this ratio occurs in the table (Table 2.1) is picked up as a main solution for the event. The results given in Table 2.1 can be drawn in a binary plot of the best fit value vs depth (Figure 2.4).

In the evaluation step, the software picks up the best fit solution, draw the best moment tensor solution and calculate values (such as, depth, magnitude, nodal planes, strike, dip, rake, principal axis value, plunge azimuth) related with the event (Figure 2.5). The evaluation of the results should be performed carefully.

28

*Table 2.1. All solutions generated by the software for given events. Red raw indicates the largest best fit value (0.7676) for event solution. This solution is accepted as a main solution for a given event. Table is generated for 2012/06/25 (13:05:28) dated event in the study area; moment tensor inversion solution is from Herrmann (2015) software.*

| | Depth | Strike | Dip | Rake | Mw | Fit | | | Depth | Strike | Dip | Rake | Mw | Fit |
|---|---|---|---|---|---|---|---|---|---|---|---|---|---|---|
| 1 | 0,50 | 275,00 | 45,00 | 90,00 | 4,34 | 0,25 | | 26 | 25,00 | 225,00 | 70,00 | -30,00 | 4,81 | 0,74 |
| 2 | 1,00 | 275,00 | 45,00 | 90,00 | 4,37 | 0,25 | | 27 | 26,00 | 225,00 | 70,00 | -30,00 | 4,82 | 0,75 |
| 3 | 2,00 | 95,00 | 45,00 | 90,00 | 4,5 | 0,35 | | 28 | 27,00 | 225,00 | 70,00 | -30,00 | 4,82 | 0,75 |
| 4 | 3,00 | 280,00 | 45,00 | 95,00 | 4,56 | 0,36 | | 29 | 28,00 | 225,00 | 70,00 | -30,00 | 4,83 | 0,75 |
| 5 | 4,00 | 60,00 | 65,00 | 30,00 | 4,49 | 0,36 | | 30 | 29,00 | 225,00 | 70,00 | -30,00 | 4,84 | 0,76 |
| 6 | 5,00 | 60,00 | 65,00 | 30,00 | 4,52 | 0,39 | | 31 | 30,00 | 225,00 | 70,00 | -30,00 | 4,85 | 0,76 |
| 7 | 6,00 | 60,00 | 70,00 | 30,00 | 4,54 | 0,42 | | 32 | 31,00 | 225,00 | 70,00 | -30,00 | 4,86 | 0,76 |
| 8 | 7,00 | 60,00 | 70,00 | 30,00 | 4,56 | 0,44 | | 33 | 32,00 | 225,00 | 70,00 | -30,00 | 4,87 | 0,76 |
| 9 | 8,00 | 60,00 | 70,00 | 35,00 | 4,61 | 0,46 | | 34 | 33,00 | 225,00 | 70,00 | -30,00 | 4,88 | 0,76 |
| 10 | 9,00 | 60,00 | 70,00 | 35,00 | 4,63 | 0,48 | | 35 | 34,00 | 225,00 | 70,00 | -30,00 | 4,89 | 0,75 |
| 11 | 10,00 | 60,00 | 75,00 | 35,00 | 4,64 | 0,50 | | 36 | 35,00 | 225,00 | 70,00 | -30,00 | 4,9 | 0,75 |
| 12 | 11,00 | 60,00 | 75,00 | 35,00 | 4,65 | 0,52 | | 37 | 36,00 | 225,00 | 70,00 | -30,00 | 4,91 | 0,75 |
| 13 | 12,00 | 60,00 | 75,00 | 35,00 | 4,66 | 0,54 | | 38 | 37,00 | 225,00 | 70,00 | -30,00 | 4,92 | 0,74 |
| 14 | 13,00 | 225,00 | 70,00 | -35,00 | 4,68 | 0,57 | | 39 | 38,00 | 225,00 | 70,00 | -30,00 | 4,93 | 0,73 |
| 15 | 14,00 | 225,00 | 70,00 | -35,00 | 4,7 | 0,59 | | 40 | 39,00 | 230,00 | 75,00 | -25,00 | 4,95 | 0,73 |
| 16 | 15,00 | 225,00 | 70,00 | -30,00 | 4,71 | 0,61 | | 41 | 40,00 | 225,00 | 65,00 | -35,00 | 5,01 | 0,72 |
| 17 | 16,00 | 230,00 | 70,00 | -30,00 | 4,72 | 0,64 | | 42 | 41,00 | 225,00 | 65,00 | -35,00 | 5,02 | 0,72 |
| 18 | 17,00 | 230,00 | 70,00 | -30,00 | 4,73 | 0,65 | | 43 | 42,00 | 225,00 | 65,00 | -35,00 | 5,03 | 0,72 |
| 19 | 18,00 | 230,00 | 70,00 | -30,00 | 4,74 | 0,67 | | 44 | 43,00 | 225,00 | 65,00 | -35,00 | 5,03 | 0,71 |
| 20 | 19,00 | 230,00 | 70,00 | -30,00 | 4,75 | 0,69 | | 45 | 44,00 | 225,00 | 65,00 | -35,00 | 5,04 | 0,71 |
| 21 | 20,00 | 230,00 | 70,00 | -30,00 | 4,76 | 0,70 | | 46 | 45,00 | 225,00 | 65,00 | -35,00 | 5,05 | 0,70 |
| 22 | 21,00 | 230,00 | 70,00 | -30,00 | 4,77 | 0,71 | | 47 | 46,00 | 225,00 | 70,00 | -35,00 | 5,06 | 0,69 |
| 23 | 22,00 | 230,00 | 70,00 | -30,00 | 4,78 | 0,72 | | 48 | 47,00 | 225,00 | 70,00 | -35,00 | 5,07 | 0,68 |
| 24 | 23,00 | 225,00 | 70,00 | -30,00 | 4,79 | 0,73 | | 49 | 48,00 | 225,00 | 70,00 | -35,00 | 5,08 | 0,67 |
| 25 | 24,00 | 225,00 | 70,00 | -30,00 | 4,8 | 0,74 | | 50 | 49,00 | 225,00 | 70,00 | -35,00 | 5,08 | 0,66 |
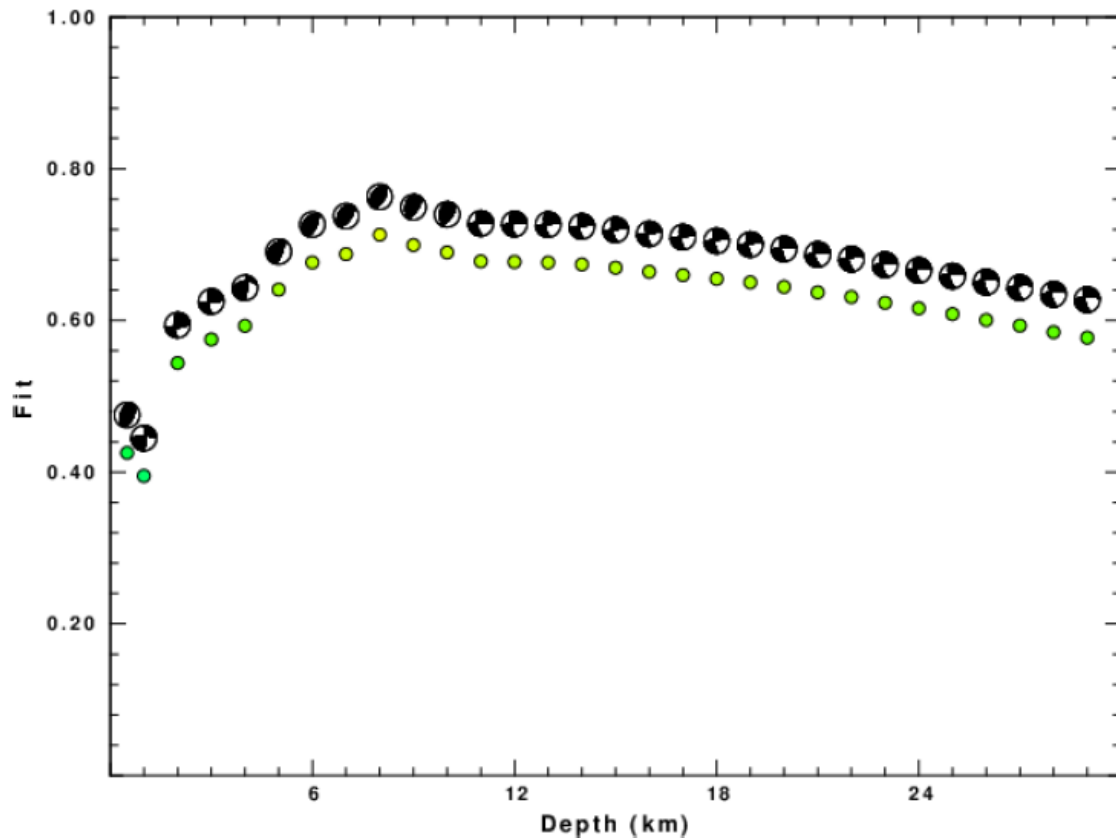
*Figure 2.4. Figure illustrating the best fit as a function of depth for 2011/04/03 (23:42:18) dated event in the study area. For this event, the best fit value is 0.7131 and indicates a depth of 8 km. Moment tensor inversion solution is from Herrmann (2015) software.*

Before getting into the final solution, the software also provides comparison between observed and predicted waveforms. Each observed (red traces)-predicted (blue traces) components are plotted using the same scale and peak amplitudes are indicated by the numbers to the left of each trace (Figure 2.6). Figure 2.6 also contains pair of numbers that indicate the time shift required for maximum correlation between the observed and predicted traces and percentage of variance reduction to characterize the individual goodness of fit (100% indicates a perfect fit).

30

**a**

| Plane | Strike | Dip | Rake |
|-------|--------|-----|------|
| NP1 | 225 | 70 | -30 |
| NP2 | 326 | 62 | -157 |

**b**

Best Fitting Double Couple

Mo = 2.54e+23 dyne-cm

Mw = 4.87

Z = 32 km

**c**

Principal Axes:

| Axis | Value | Plunge | Azimuth |
|------|-------|--------|---------|
| T | 2.54e+23 | 5 | 277 |
| N | 0.00e+00 | 54 | 14 |
| P | -2.54e+23 | 35 | 183 |

**d**

*Figure 2.5. Moment tensor inversion solution of 2012/06/25 (13:05:28) dated event in the study area, generated by Hermann (2015) software. Tables indicating (a) nodal plane's strike, dip and rake values; (b) magnitude and depth; (c) T, N, P axis, plunge and azimuth value. (d) focal mechanism solution of the event.*

*Figure 2.6. Figure indicating correlation and percentages between observed (red traces) and predicted (blue traces) for 2011/04/03 (23:42:18) dated event in the study area. Three components of seismic record are R (Radial), Z (Vertical), and T (Transverse). Each observed-predicted component is plotted using the same scale and peak amplitudes are indicated by the numbers to the left of each trace. A pair of numbers given in black at the right of each predicted traces indicates: (i) the upper number, the time shift required for maximum correlation between the observed and predicted traces and (ii) percentage of variance reduction to characterize the individual goodness of fit. Solution is from Herrmann (2015) software.*

Furthermore removing seismic record, which has not good correlation between predicted and observed, gives more dependable solutions. In order to find good correlation, elimination of the seismic stations that present low correlation value and/or band pass filter can be applied to waveforms. This is one important way of improvement and optimization of reprocess as indicated in Figure 2.1. Before second data processing, band filter is being optimized as part of the second improvement and optimization of reprocess.

Time shift between predicted and observed waveform traces is required because the synthetics are not computed at exactly the same distance as the observed and because the velocity model used in the predictions may not be perfect. A positive time shift indicates that the prediction is too fast and should be delayed to match the observed trace (Figure 2.6). A negative value indicates that the prediction is too slow. The time shifts are used to test the epicenter and origin time parameters that started the process.

A large change may indicate the need to relocate the event and rerun the processing. The time shifts for waveform matching may arise from several reasons. (i) Firstly, origin time and epicentral distance are incorrect. (ii) Secondly, velocity model used for the inversion is incorrect. (iii) Thirdly, velocity model used to define the P-arrival time is not the same as the velocity model used for the waveform inversion (assuming that the initial trace alignment is based on the P arrival time). By using one mislocation, time shift can be fitted a functional form by using equation 1. By using this formula, time shifts for this inversion lead to the next figure (Figure 2.7). The red color indicates good fit to the waveforms.

Time_shift = A + B cos Azimuth + C Sin Azimuth          equation 1
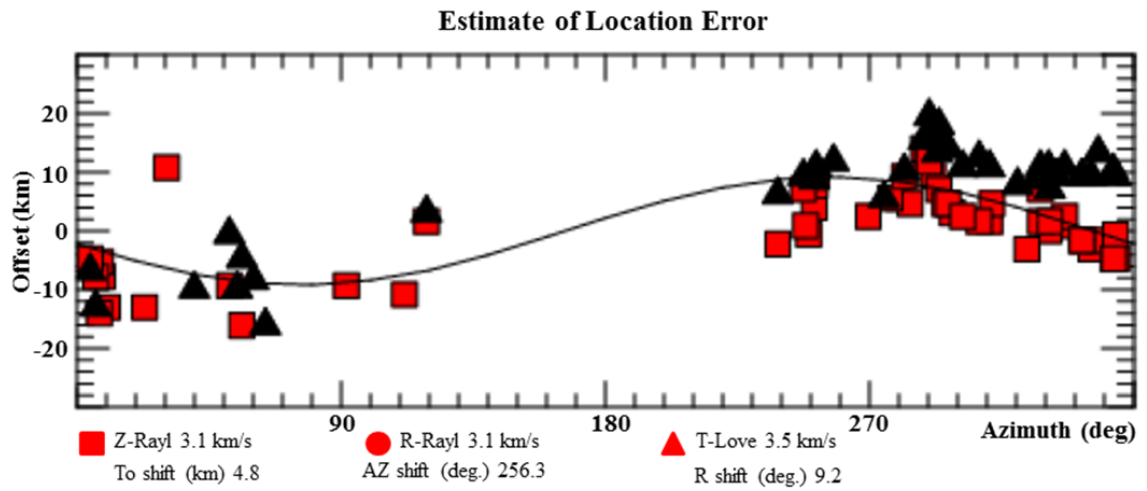


*Figure 2.7. The time shifts between predicted and observed waveform traces for inversion calculations of the 2012/06/25 (13:05:28) dated event in the study area. Moment tensor inversion solution from Hermann (2015) software.*

## 2.2. Seismic Data Acquisition and Processing

In order to recognize geological structures (faults) within the study area, 2D seismic profiles are interpreted, faults are mapped. All seismic reflection data (352-km long) were acquired during a research cruise in 1996 and 1997, by the MTA Sismik-1, which belongs to General Directorate of Mineral Research (MTA).

Seismic data acquisition parameters are decided to observe main target(s) that researchers want to investigate. Optimization of shot interval, group interval, number of channel and sample interval parameters supply more resolution at researcher's target area. The main acquisition parameters of these seismic data are given in Table 2.2.

*Table 2.2. Table indicate shot interval, group interval, number of channel, sample interval record length which were applied during data acquisition.*

| Line Name (Year) | Mar96 (1996) | Mar97 (1997) |
|---|---|---|
| Shot Interval (m) | 50 | 50 |
| Group Interval (m) | 12.5 | 12.5 |
| Number of Channel | 96 | 120 |
| Sample Interval (ms) | 2 | 2 |
| Record Length (ms) | 5000 | 5000 |

All seismic data were processed by using SeisSpace ProMAX Seismic Processing Software in the MTA Marine Data Processing Laboratory, Department of Marine Research. A conventional seismic data processing flow (Figure 2.8) was applied to the data until stack section step. In the stack section step, specific stacking method (*Common Reflection surface stack*) is applied to the data to increase the signal content.
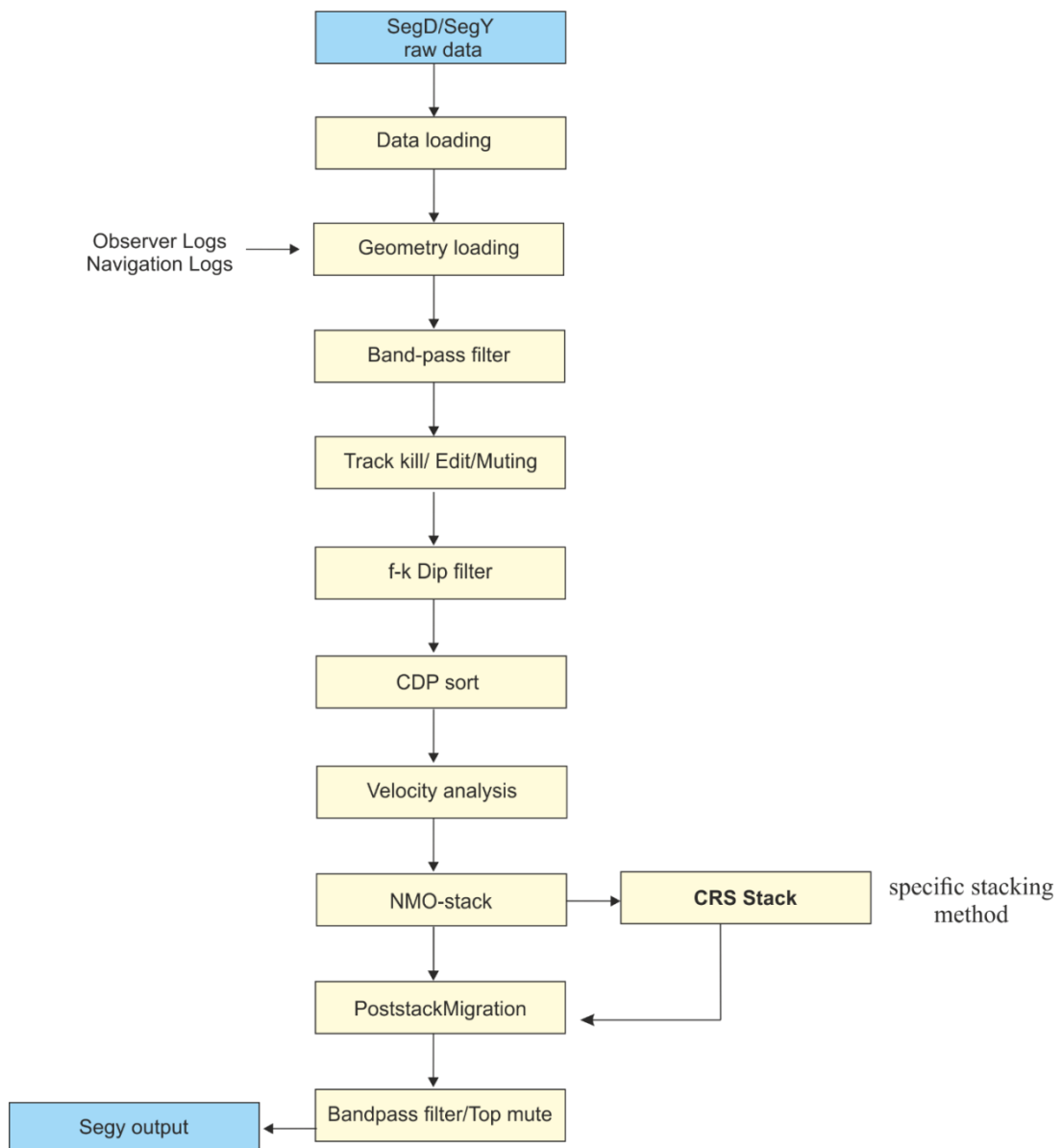
*Figure 2.8. Data processing step applied to Mar96 and Mar97 seismic data acquired by MTA RV Sismik-1 at 1996–1997.*

The processing stream (Figure 2.8) was as follows: raw data importation, static, geometry definition, bandpass filter, F-K filter, kill trace, mute, sort, NMO analysis and CRS stack and time domain Kirchoff migration, frequency filtering, and finally automatic gain correction. No multiple elimination methods were used to remove multiples from the real reflections.

35

The first step of seismic processing is loading SEGY raw data to processing software. After this step, seismic data acquisition parameters are entered to processing program; this means *Geometry*. In the other words, *Geometry* definition is design of source-receiver geometry and it is completed by using real coordinates of the sources and receiver for each shot location (Dondurur, 2018). Seismic data may have some different noise types, which needs to be removed by filtering. Frequency filtering is an operation of directly changing the amplitude range of the seismic data. Also *trace edit* is one of the earliest methods to remove noise from the seismic data. *Muting* is used to remove direct waves, refractions, etc. in the seismic data.

Seismic data consists of noise and reflection with different dips. The most important purpose of f-k filter is generally to removing the linear events, such as tail buoy noise, bird noise, or cable noise.

After f- k filter, all traces are sorted into a single gather; this step is called CDP sort. The traces are sorted by offset because of performing velocity analysis for data processing and *moveout correction* (http://subsurfwiki.org/wiki/Gather). For velocity analysis, the most important step is *NMO flow*; the reflection from horizon arrives receivers through the length of streamer with different travel time. However, if the velocity is known, the arrival time difference (*moveout*) at each receiver can be predicted. (https://wiki.aapg.org/Seismic_processing_basics)

In the stack section step, instead of traditional NMO stacking method, CRS (Common Reflection Surface) stacking method was preferred and applied to the data set to increase the signal content on the wavelet. CRS gets a clearer image and coherent structures reflected from the ground (http://geoprocesados.com/english/nuestros-servicios/procesamiento-sismico-crs/index.html). CRS-stack method produces better reflector continuities over the NMO stacking method.

Finally, Kirchoff migration is applied to stacked data. Seismic migration is a process for moving the reflection events in the seismic data to their true subsurface locations (Dondurur, 2018). It is a process that suppresses the diffractions and dipping reflecting

events on a stacked section to their supposedly true locations (https://wiki.seg.org/wiki/Basic_data_processing_sequence). After Migration bandpass filter is used to improve the clarity of the seismic section. The last step seismic section interpretation is final top mute for removing the noisy area just above the seabed and is to get a clearer final seismic section.

The results of seismic interpretation and moment tensor inversion method will be presented in Chapters 3 and 4, respectively.

# CHAPTER 3

## SEISMIC INTERPRETATION

This chapter contains structural and seismic stratigraphical interpretation of 2D seismic data (120-96 channel) acquired by the General Directorate of Mineral Research and Exploration of Turkey (MTA) Sismik-1 Research Vessel during a research cruise in 1996 and 1997. The data is processed by using SeisSpace ProMAX Seismic Processing Software in the MTA Marine Data Processing Laboratory, Marine Research Department. The software used to define main tectonic structures of the study area during seismic interpretation is PETREL E@P.

A total of 360-km-long 7 seismic sections are interpreted; they are renamed as section A thorough section G (Figure 3.1; Table 3.1). Four sections are oriented almost parallel to the coastline in NW−SE direction (sections A, B, C and D); a direction being almost perpendicular to expected fault's strike in the Pliny-Strabo STEP fault zone. Three seismic lines (sections E, F and G) trend in W−E direction (Figure 3.1). Longest seismic section is line D with a length of 84.87 km and the shortest, line E with a length of 84.87 km. Both seismic lines are the nearest to shoreline among NW−SE and W−E seismic lines, respectively (Figure 3.1; Table 3.1).

Main purpose of this chapter is therefore to intepret, define and map major tectonic and seismic stratigraphical features of the thesis study area; main faults' strike and dip directions will also be studied. Furthermore interpreted fault strike and dip direction will be used and compared with the results of moment tensor inversion solutions of the selected events occurred in the study area (see Chapter 5). Finally, strurctural and stratigraphical framework of the study area will be established.
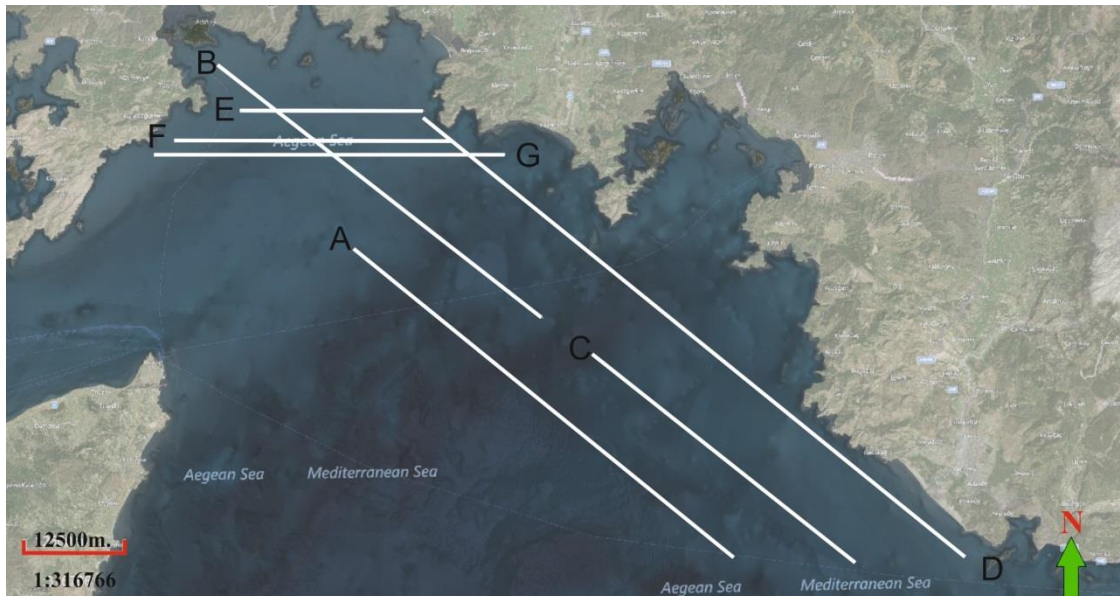
*Figure 3.1. Location map of seismic lines acquired by MTA Sismik-1 in 1996-1997. Seismic lines are renamed as A, B, C, etc.*

*Table 3.1. Length and direction of seismic sections.*

| Section Name | Length | Direction |
|---|---|---|
| Seismic Line E | 21.70 km | W–E |
| Seismic Line F | 32.80 km | W–E |
| Seismic Line G | 42.08 km | W–E |
| Seismic Line D | 84.87 km | NW–SE |
| Seismic Line B | 61.62 km | NW–SE |
| Seismic Line C | 50.24 km | NW–SE |
| Seismic Line A | 58.11 km | NW–SE |

40

## 3.1. Seismic Horizon Identification

Seismic sections are geologically interpreted; four (4) seismic stratigraphic horizons that bounds 3 (three) main units are picked based on seismic stratigraphical features like, erosional truncation, uncomformities, initial surface of deposition, etc. Main reason of horizon identification is neither clarifying stratigraphical and lithological distinction between various rock units in the study area nor attempting to make correlation with other rock units identified and madded in the onshore. Actually, it is aimed at indicating tectonic structures more accurately and effectively; finally faults are interpreted. The description of the seismic units will be given in the following subsections.

### 3.1.1. Seismic Unit 1

Horizon 1 represents a sea-bottom layer where seismic sections have strong and continous reflections that can be trace all along each seismic sections. Reflection coefficient of seafloor, P wave, is an unique parameter for acquisition interpretation and processing of seismic data (cf. Schneider & Backus, 1964; Amundsen & Reitan, 1995; Sheriff & Geldart, 1995; Caldwell, 1999; Stewart et al., 2002; Edme & Singh, 2008). Seafloor model (a simple shallow-water model) depends on an isospeed water column (homogenous acoustic water layer) over homogenous elastic half-space (cf. Etter, 2018). Sharp connection between two media creates significant seismic traces.

Bathymetric data between Fethiye-Marmaris bays is also important for the identification of *horizon 1* and active tectonic structures as indicated in Figure 3.2. Upper boundary of the *unit 1* marks the seabottom surface in the study area.

Furthermore deformation (offset) of *Horizon* 1 as the upper boundary of the *unit 1* is also important to identify and locate active tectonic structures in the study area and to interpret Holocene and Pliostecene activity of these faults (Figure 3.3). Some lanslides also ocuured in unit 1 that cause thickening dominantly high slope area. Lower boundary of *seismic unit 1* is defined by *horizon 2*. Unit 1 can therefore be identified with acoustically strong, high reflective continous seismic reflectors. The thickness of

the Pleistocene–Holocene *unit 1* ranges between 35 ms and 75 ms. Depending on sedimentation rate in the study area, thickness may correspond to only Holocene age of the sediments. Furthermore, there is also a possibility that as active sedimentation continues, the *unit 1* may cover inffered active tectonic structures; in this case, the lower boundary of the *unit 1* becomes very important. The possible deformation (offset) of this boundary then may define Pliostecene–Holocene activity of tectonic structures.
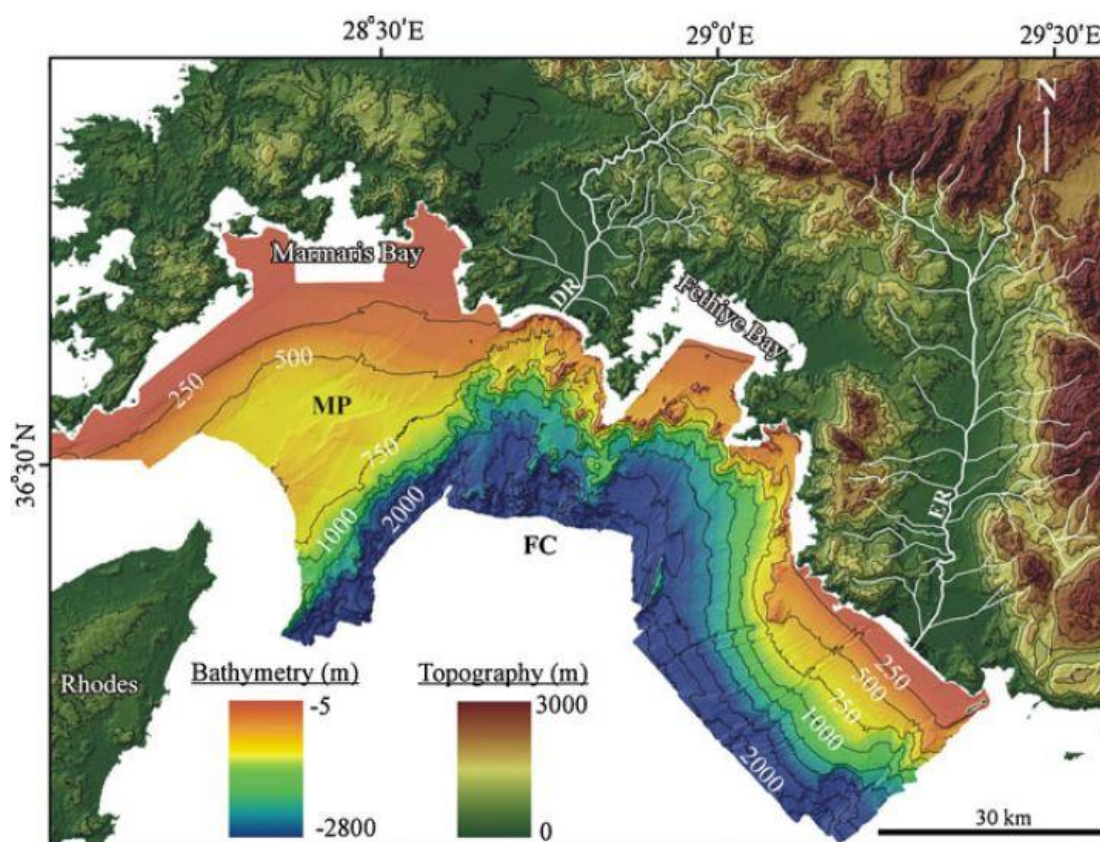


*Figure 3.2. Multibeam bathymetric data for the area between Marmaris Bay in the west and Finike Basin in the east. The date is obtained by TCG Çeşme and TCG Meseah-2 research vessels in 2009 and belongs to Turkish Navy, Department of Navigation, Hydrography and Oceanography (from Ocakoğlu, 2012).*

### 3.1.2. Seismic Unit 2

Seismic *unit 2* is interpreted below surface where strong sea bottom (unit 1) reflection does not occur. *Horizon 2* therefore forms the upper boundary of the *unit 2*. It is interpreted as a regional unconformity which is regional landslide's upper surface as

it truncates and covers the upper surface of the *unit 2*; the *Horizon 2* is well illustrated along seismic section G (Figure 3.4). Seismic horizon just below the truncation (erosional) surface, where relatively strong reflections occur, is interpreted as a *horizon 3*. Seismic unit limited by horizon 2 and horizon 3 is defined as unit 2 and this unit is marked by relatively low reflective laterally non-continous seismic reflectors (Figure 3.4).

Thickness of the *unit 2* is variable because of the geometry of the erosional surface. Local landslide is interpreted as possible cause of this truncation and it is observable only along section G (Figure 3.4). Similar submarine landslide is described as giant feature in the South China Sea and its length may reach up to 250 km along the continental slope (cf. Zhu, 2019). Regional erosional surface indicating upper boundary of the unit 2 is well presented in Figure 3.5 where truncation can be observable significantly. The landslide is interpreted to be triggered by earthquake and is marked by a sudden break in the seabottom morphology (Figure 3.6).
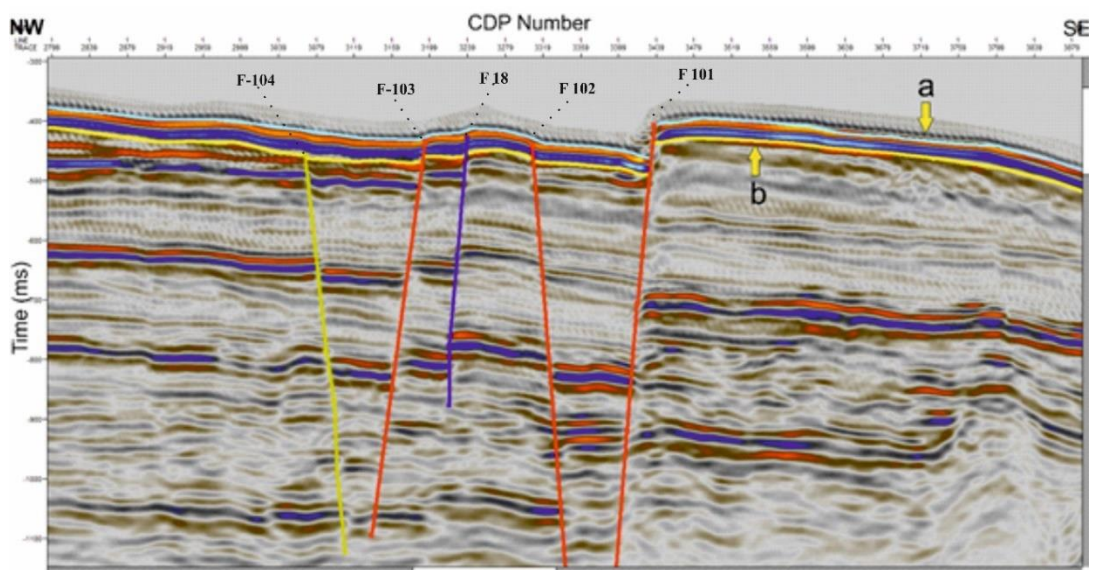


*Figure 3.3. Seismic section illustrating seismic unit located between yellow and blue lines. Blue line ('a') indicates seabottom and the upper boundary of the unit 1; yellow line marks the lower boundary of the unit 1. Seismic section is cut from seismic line B. The distance between two CDP is 6.25 meters. Note the offset of both lower and upper boundaries along interpreted fault F1 that suggest the recent (Holocene, and possibly Pleistocene) activity of the fault. Note also that, some faults (F2, F3 and F4) offset the lower boundary (line b) of the unit 1, while fault F5 appears terminate against the same boundary. This suggests possibly Pliocene–Holocene activity of the first group of faults and that the fault F5 may not be an inactive structure. See Figure 3.1 for location of the seismic section.*

43
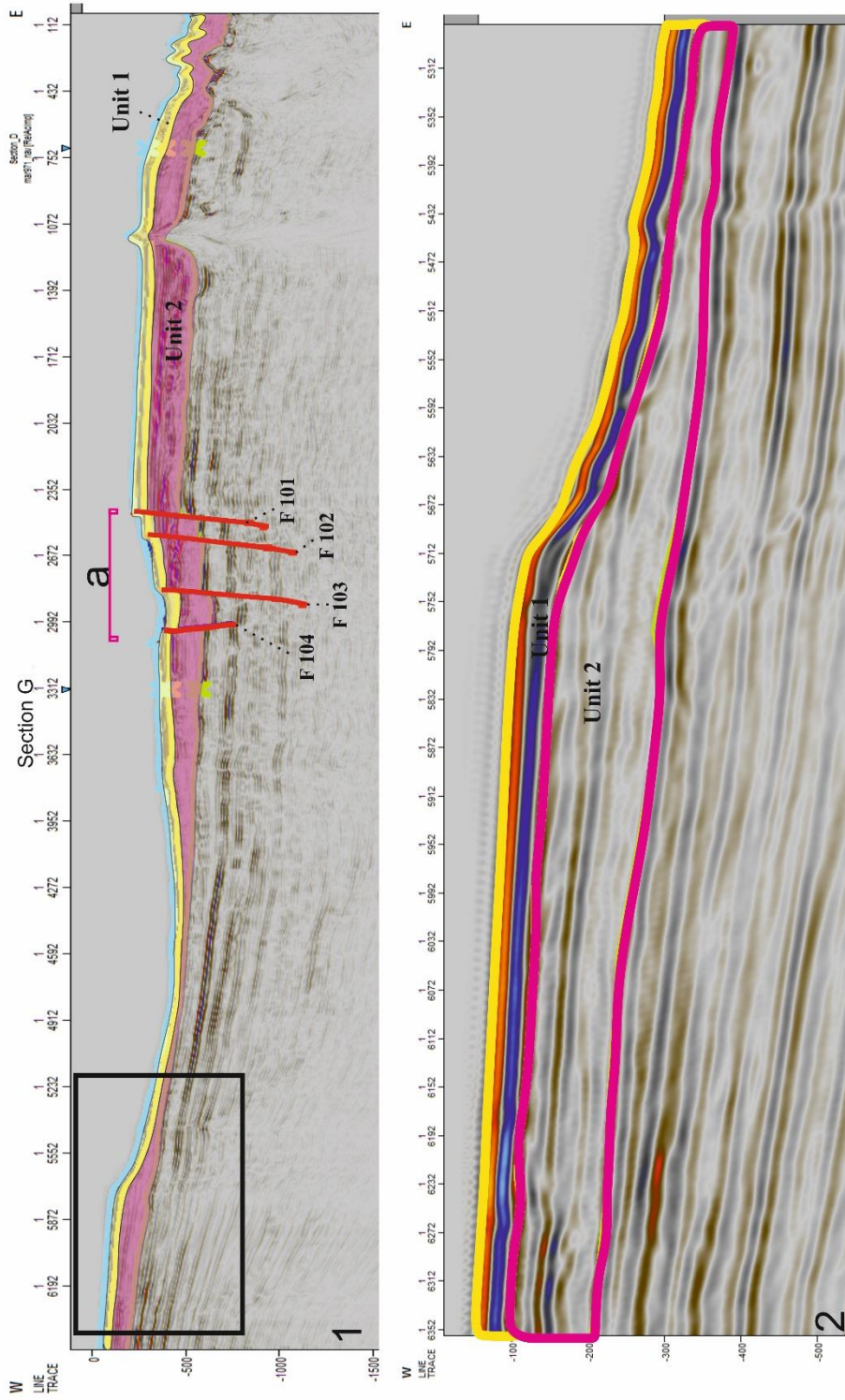
*Figure 3.4. (1) Interpretation of the seismic unit 2 along 42-km-long E–W seismic section G. Note truncated (erosional) boundary between the two units. Area A represents a deformation zone marked by a series of faults with normal displacement. The step like geometry and a small half graben are pronounced. Rectangle shows the location of lower diagram, which represents a detailed view of the boundary between units 1 and 2 (2). Unit 1 in yellow color and, unit 2 in purple. See Figure 3.1 for location of the seismic section.*
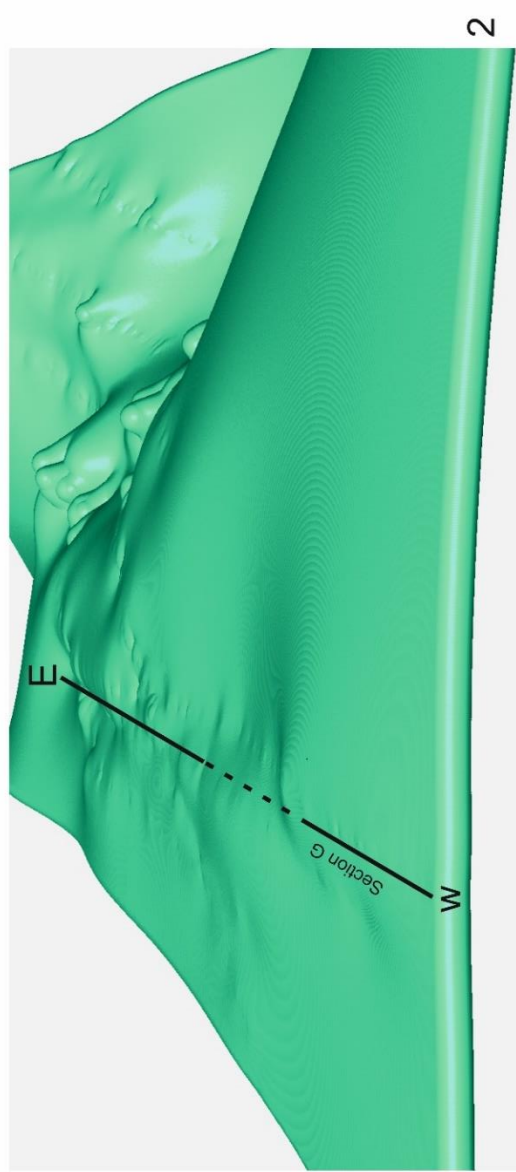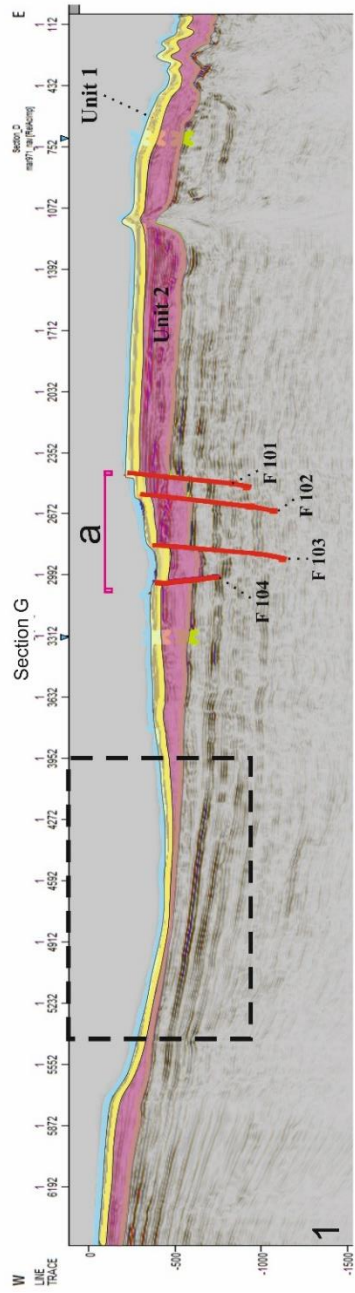
*Figure 3.5. (1) Interpretation of the seismic unit 2 along 42-km-long E −W seismic section G. Dashed rectangle shows area of landslide and the best location where truncated (erosional) surface is well exposed. Note the dramatic decrease in the thickness of the unit 2. (2) Sea-floor geometry in the area between Marmaris and Finike bays. See Figure 3.4 for more explanation. Note abrupt break in the slope immediately to the south of seismic section G line; The erosional surface is interpreted as a regional unconformity and is well observable in the area to the south of the section G. unit 1 in yellow colour and, unit 2 in purple. See Figure 3.1 for location of the seismic section.*

45
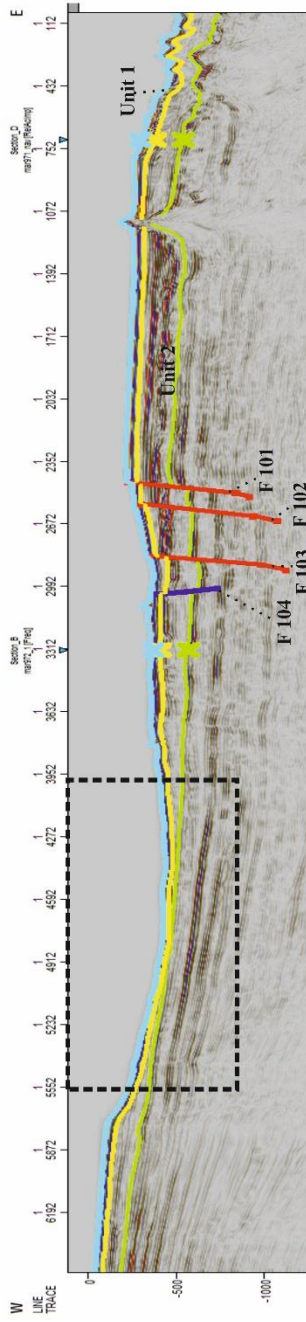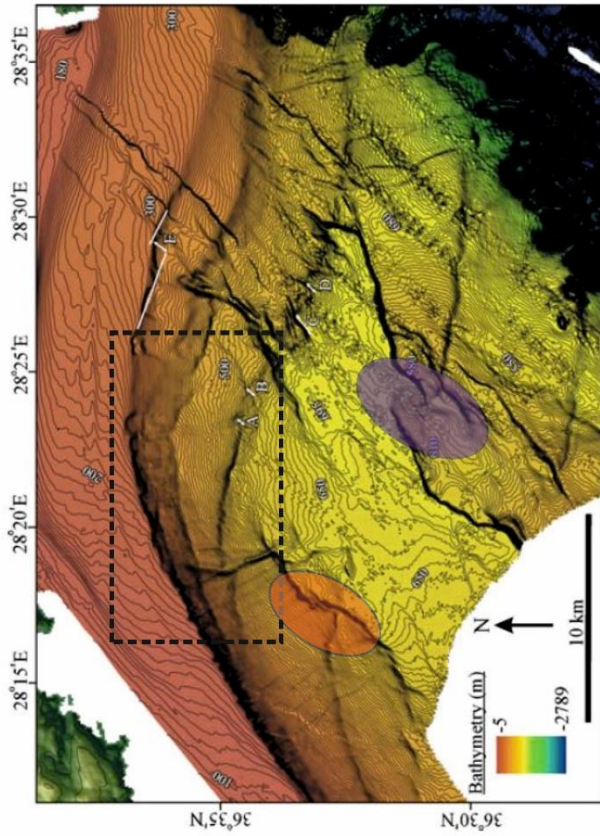
Figure 3.6. (a) Interpretation of the seismic unit 2 along 42-km-long E −W seismic section G. The area of landslide is marked by dashed rectangle. See Figure 3.4 for more explanation about the section; (b) bathymetric map of the study area from Ocakoğlu (2002). Dark undulated lines corresponds to NE–SW-trending offshore normal (?) faults. Note that the faults overlap and form well-developed relay-ramp (s) (purple ellipse area). Note also curving of fault segments into one another to define a corrugated geometry (red ellipse area). The faults and the landslide are marked by abrupt break in seafloor bathymetry (slope). See Figure 3.1 for location of the seismic section.

46

### 3.1.3. Seismic Unit 3

Seismic *unit 3* is identified between horizon 3 and horizon 4 (Figure 3.7). Horizon 3 is interpreted as a conformable boundary between unit 2 and unit 3. Seismic unit 3, when compared with the seismic *unit 2*, has relatively strong and non-continuous seismic reflectivity. Lateral continuity of seismic reflections in seismic unit 3 is less observable compared to the seismic unit 2.

The lower boundary of the seismic *unit 3* is identified by seismic horizon 4 and it forms the upper boundary of seismic basement in the seismic sections (Figure 3.7). The style and pattern of deformation in the seismic basement differs clearly from other horizons described above; it is well illustrated in seismic section B (Figure 3.8). In this figure, some inactive faults intersect the upper boundary of the seismic basement (horizon 4); it appears that these structures control the upper boundary of seismic basement in the NW of the study area. Relatively high amplitude and continuous parallel reflections indicate low energy depositional environment for the unit 3 (Posamentier et al., 1992a, 1999a; Vail et al., 1991; Van Wagoner et al., 1990)

### 3.1.4. Seismic Unit 4 (Seismic Basement)

The seismic unit 4 constitutes the deepest stratigraphic unit in the study area. The lower frequency reflections of this seismic unit terminate along the upper surface of the seismic basement with downlap and onlap structures. The upper boundary is prominent and interpreted as an erosional surface covered unconformably by the seismic *unit 3* (Figure 3.8). Lower boundary of the seismic basement is not imaged in the seismic sections because penetration of the seismic waves is not satisfactory at greater depths.

The basement unit may be correlated with variably thick Messinian evaporites in the Eastern Mediterranean that form a prominent seismic marker succession in the Finike and Antalya bays (Aksu et al., 2009; İşler et al., 2005). Messinian evaporites are however absent in the study area because the Rhodes Basin remained above the depositional evaporite environment during the Messinian (cf. Woodside et al., 2000;

Aksu et al., 2009; Hall et al., 2009; Roveri et al., 2014a, b). The contention that Messinian evaporites are not present in the area of interest is also supported by a map that shows distribution of Messinian evaporates in the Mediterranean (Figure 3.9; Roveri et al., 2014). The seismic basement therefore must be represented by pre-Messinian rocks that forms the basement of onland Çameli-Gölhisar, Eşen, Kasaba, Aksu, Köprüçay and Manavgat basins.
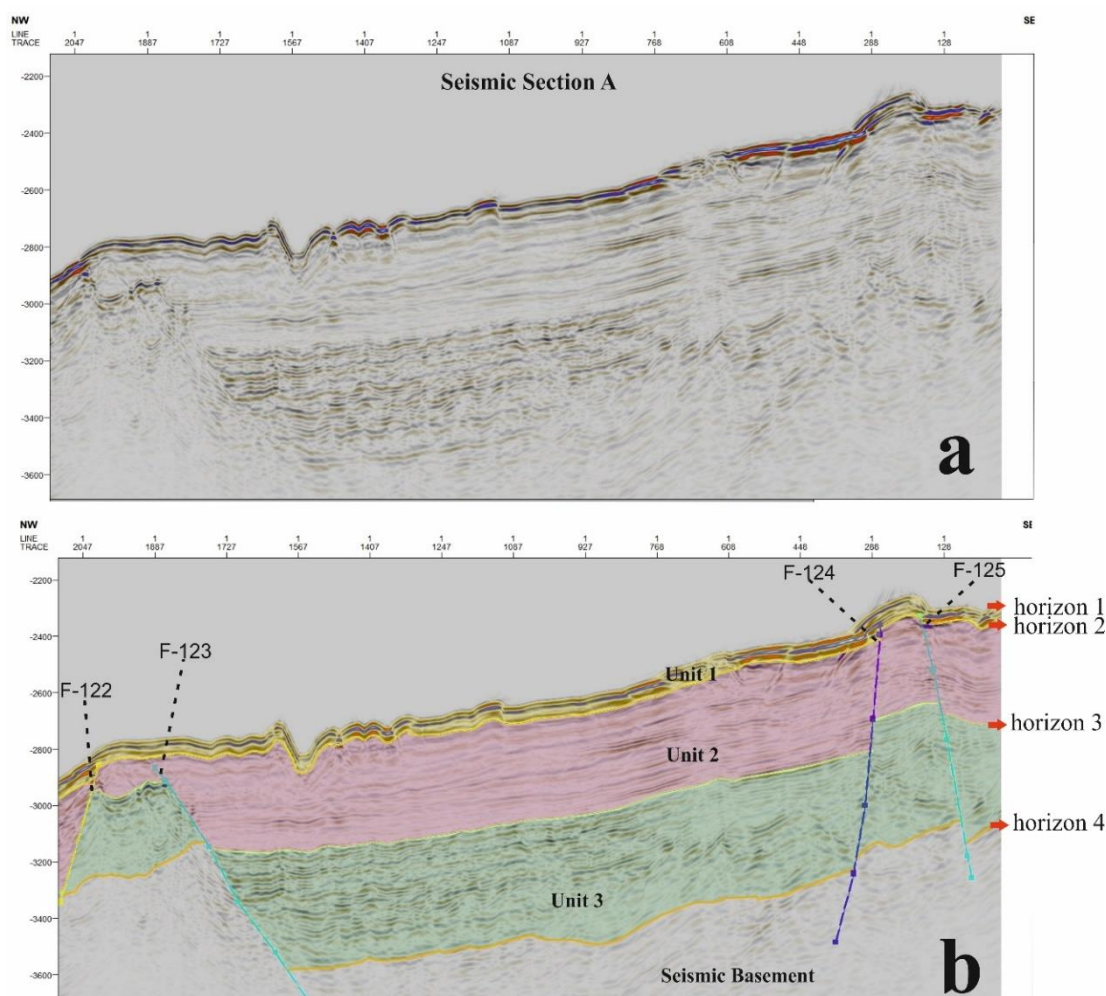


*Figure 3.7. Interpretation of the seismic unit 3 along ca. 58-km-long NE–SW seismic section A. (a) uninterpreted and (b) interpreted section. Note that some of the faults (F122, F124 and F125) cut and displace (normal slip) the horizon 2 (lower boundary of the seismic unit 1) while F123 terminates within the unit 2. It appears that the faults do not deform the sea floor. These faults define a typical horst-and-graben structure; the graben, bounded by faults F123 and F124, appears as a relatively large-scale asymmetric structure tilted towards northwest while bounding horst are narrow features. See Figure 3.1 for location of the seismic section.*
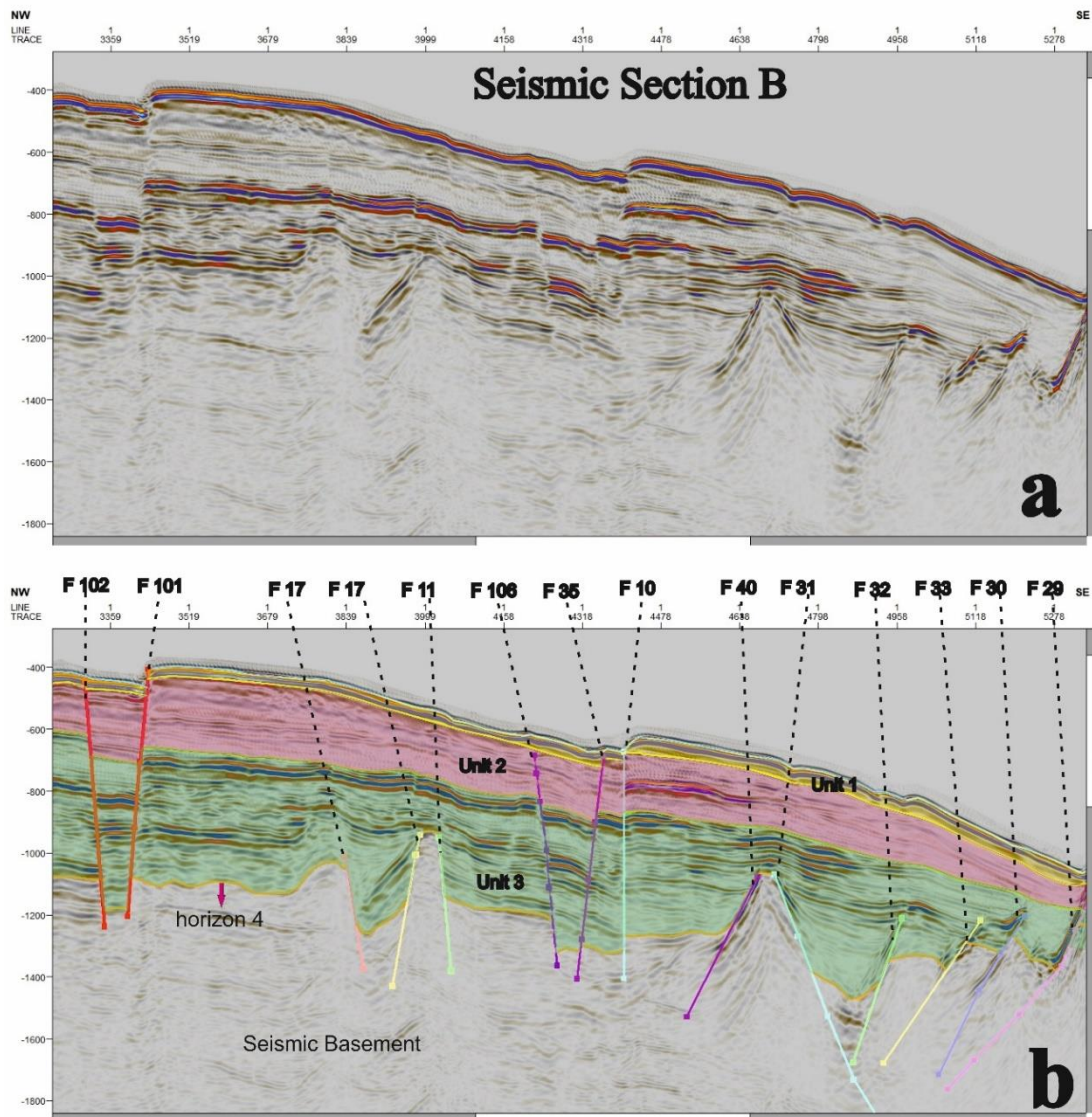
*Figure 3.8. Interpretation of the upper boundary of the seismic basement (horizon 4) along 58-km-long NE–SW seismic section B. (a) uninterpreted and (b) interpreted section. The basement displays lower frequency reflections which distinctly differ from that of other overlying seismic units. Note that there are several faults with normal motion cut and displace the horizon 4 only; the horst-and-graben structure controls post-basement sedimentary environment. Other faults (F102, F101, F10 and F29 appear to cut and displace the sea floor, thus attesting their possibly Holocene activity.*

Some faults (F106 and F35) appear to deform the post-basement sedimentary succession (seismic units 1 thorough 3) but terminates against sea floor and thus suggest their presumably Pleistocene activity. See Figure 3.1 for location of the seismic section.
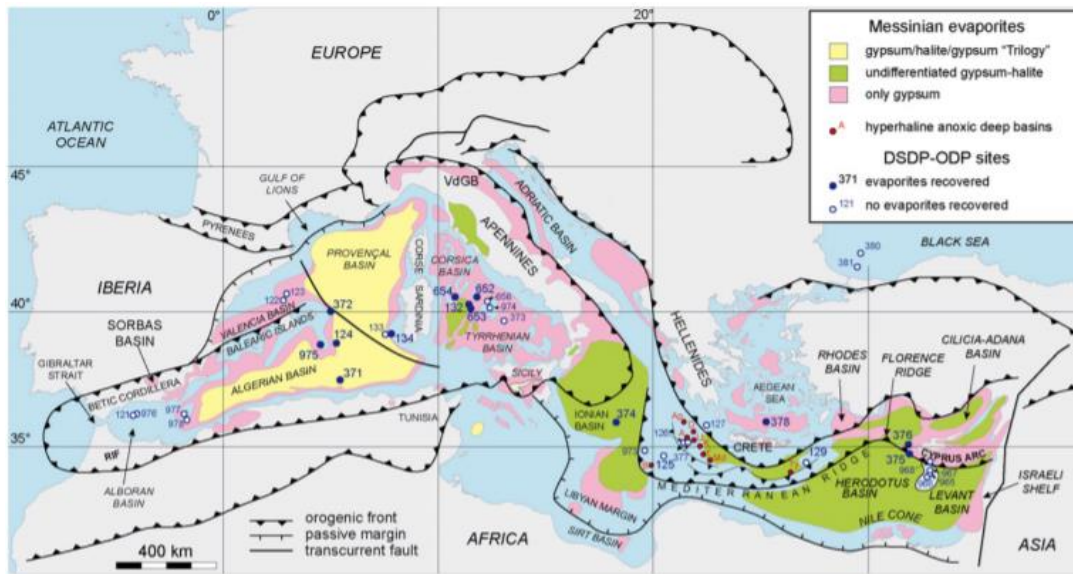
*Figure 3.9. Distribution of Messinian evaporates in the eastern Mediterrenean (from Roveri et al., 2014b).*

## 3.2. Seismic and Structural Interpretation of the Study Area

Seismic structural interpretation of the study area is performed by using seven (7) main seismic sections acquired in the area Fethiye and Datça bays (Figure 3.1). Seismic sections E, F and G are oriented in E−W direction and used to interpret and identify N−S-trending faults. These seismic sections are respectively shorter and crosscut the Datça Bay. Whereas seismic sections A, B, C and D are respectively longer profiles and crosscut both the Fethiye and Datça bays. They are oriented in a WNW−ESE direction and used to interpret and identify SW−NE-trending tectonic structures. During structural interpretation of the seismic sections, all possible faults are picked up and identified; their geometry (dip direction) and dip-slip components (normal or reverse) are also discussed.

Furthermore, in our seismic sections, tectonic structures are classifed as (i) faults responsible for opening of main basins (*margin-bounding faults*) and (ii) intra-basinal fault. Basin-bounding faults are considered as a main faults that caused events (earthquakes) occured in the study area. If continuity of these faults appear in at least two seismic sections, they are labelled with numbers, like F100 and F102 (Figures 3.7

50

and 3.8). All seismic sections are viewed at 3D window (Petrel software) iteratively to trace and understand continuation of these faults along the next seismic section. Otherwise, the fault names are not labelled.

### 3.2.1. Seismic and Structural Interpretation of Seismic Section E

W−E-oriented seismic section E has a total length of 21.7 km (Table 3.1) and is the closest seismic section to the Mediteranean shore line in the study area (Figure 3.1). Section E is placed at the centre of the Marmaris Bay where sea bottom is almost horizontal and water depth may reach up to 200 m. At the east of the section E below the *unit 1*, there is a seismic succession which is presumably different the *unit 2* (Figure 3.10a, c). This unit appears to display  coastal onlap, which in turn indicates that deposit are transported from the land. This succession is included within the seismic unit 2 because it only appears in this particular area only where Dalaman river is very close section E (Figure 3.10). Seismic package is therefore interpreted as deltaic deposits accumulated by the Dalaman River and/or related river system in the study area. The seismic basement (*unit 4*) is cut and displaced by near vertical faults in this particular area (Figure 3.10a, c) whereas the horizon 4 is smooth and appears not deformed in other parts of the seismic section E in Marmaris Bay area where close to the shoreline.

Faults F-102 and F-101 are interpreted as major structures in this section; they also appear in seismic  sections F, G and B. Fault F-102 appears as almost vertical structure; its relationship with the seabottom is not possible to observe and it is not clear if this structure deforms the sea floor or not  (Figure 3.10c).

The dip direction of the  fault F-102 appears changing at different seismic sections that indicates presume strike-slip nature of faulting. F-101  is also interpreted in seismic sections E, F, G and B; it appears to deform seabottom that may indicate recent activation of the fault. Last event caused from the fault F-101 may be of Pleistocene−Holocene age. The fault F-101 appears almost vertical or dipping steeply westwards in all seismic sections
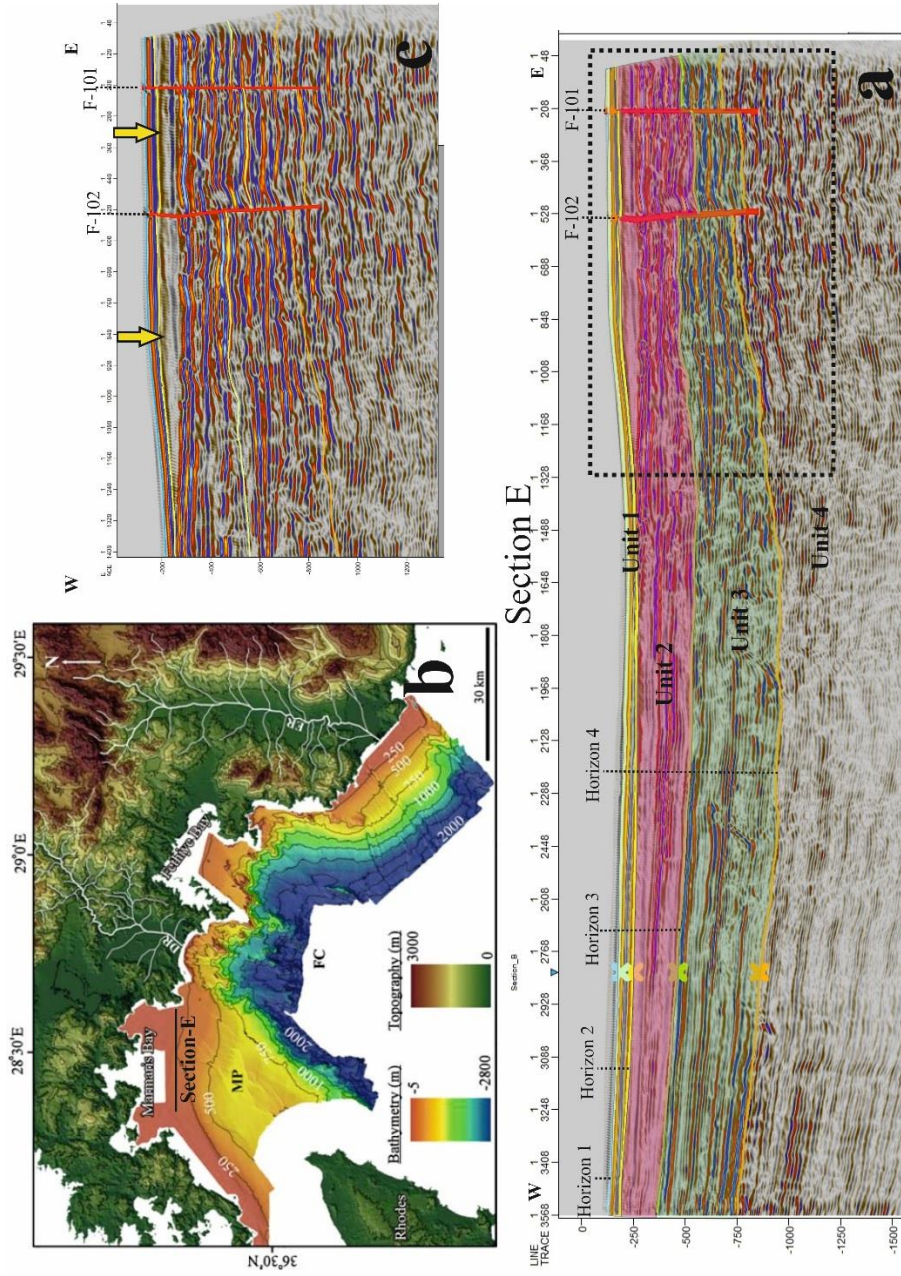
Figure 3.10. (a) Structural interpretation of ca. 22-km-long W–E-trending seismic section E. Dashed rectangle shows location of Figure 'c'; (b) Multibeam bathymetric data for the area between Marmaris Bay in the west and Finike Basin in the east (from Ocakoğlu 2012) and (c) zoomed picture of the dashed rectangle in 'a'. Yellow arrows indicate Dalaman river-related fluvial deposits. Note that fault F-101 appears to cut and displace the sea floor but not the fault F-102, thus attesting the Pleistocene –Holocene activity of the former. The displacement of the units 2, 3 and 4 are evident; the area between the two faults appears as small graben structure. Some artifact noise, which is not removed during seismic data processing, appears between CDP 500 and CDP 100. See Figure 3.1 for location of the seismic section.

52

### 3.2.2. Seismic and Structural Interpretation of Seismic Section F

W−E-oriented seismic section F has a total length of 32.8 km (Table 3.1) and is the second closest seismic section to the Mediteranean shore line in the study area (Figure 3.1). Section E is also placed at the centre of the Marmaris Bay where water depth may reach up to 250 m.

There appears that the thickness of the *unit 1* in areas close Dalaman river system is relatively greater than that of the other parts along the profile; this may suggest higher sedimentation rate related to deposition by river system (Figure 3.11). The upper bundary of the seismic basement, the horizon 4, appears almost straight and suggests that, like in seismic section E, deformation of the seismic basement deformation is not observable along seismic section F.

Two faults labelled F-102 and F-101 are interpreted along this profile (Figure 3.11); these structures are also apparent in seismic sections E, G, and B. Fault F-101 appears almost vertical or dips east with very high angle whereas fault F-102 is subvertical and dips east. Horizon 3, cut and displaced by the faults F-101 and F-102, creates a dipping surface (Figure 3.11c). As it stands, the Fault F-101 appears to have reverse component where horizon 3 is clearly cut and displaced upward in the eastern block (Figıre 3.11b). The area between the two faults appear to move downward and is filled with sediments of the *unit 1*; it is much thicker in the downthrown area.

Similar to seismic profile E, the fault F-102 appear not cutting the sea floor but it diplaces the lower boundary of the unit 1. Whereas the fault F-101 appears to displace (normal motion) the seabottom, attesting its recent, presumably Pleistocene−Holocene, activity.
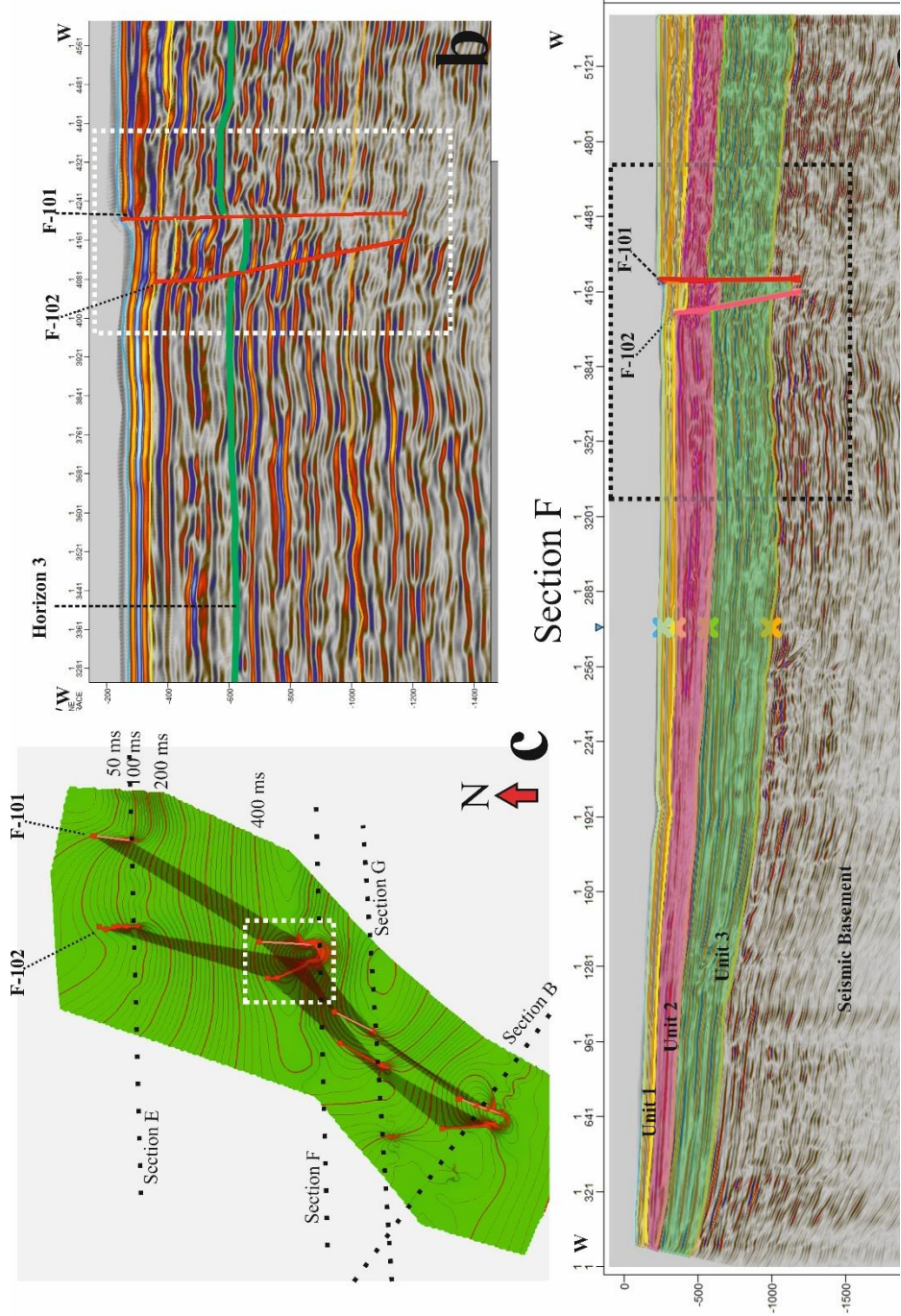
Figure 3.11. (a) Structural interpretation of ca. 33-km-long W–E-trending seismic section F. Dashed rectangle shows location of Figure 'c'; (b) zoomed picture of the dashed rectangle in 'a' and (c) dipping surface generated from horizon 3 (green area) to indicate faults F101 and F102. It is dissected by the two faults. White rectangle indicates surface and horizon 3 intersection area. There contours between two bold red lines indicate 50 ms. Note that fault F-101 appears to have reverse dip-slip displacement while F-102, normal motion. The displacement of the unit 2 is evident; the down-thrown area between the two faults appear to be filled by sediments of the unit 1. See Figure 3.1 for location of the seismic section.

54

### 3.2.3. Seismic and Structural Interpretation of Seismic Section G

W−E-oriented seismic section G has a total length of 42.08 km (Table 3.1 ) and is the third closest seismic section to the Mediteranean shore line in the study area (Figure 3.1). It is placed at the end of Marmaris Bay where sea bottom is almost horizontal and water depth may reach up to 400 m.

There appears deformation of the see bottom in the eastern part of the seismic section G; it is intepreted as an artifact that arises from approaching continental slope and faulting and is produced by seismic data processing error (Figure 3.12). The unit 2 is interpreted by using seismic stratigraphical relationship from seismic section F. West of the section is marked by a regional landslide (see Section 3.1.2. for more information; Figures 3.4 – 3.5).

Two main active fault zones are interpreted and labelled as fault zone A and B (Figure 3.12). Fault zone A is observed between CDP 3100 and CDP 2300 and comprises faults F-104, F-103, F-102 and F-101. Furthermore fault F-18 described in in section B only is included in this fault zone (Figure 3.12). The step-like geometry and a small half graben bounded by these faults are pronounced. Main strike direction of the fault zone A is approximately N40°E. Dip direction and minor dip-slip component of the fault segments  change from one section to another; this phenomenan is attributed to the strike-slip dominant nature of the fault zone. As described in other seismic sections, the strike of the fault segments is also variable from one section to another; the amount varies between 5° and 20°. Faults F-103 and F-104 are also defined in seismic sections G and B.

The second fault zone (fault zone B) comprises faults F-14, F-100 and F-106 (Figure 3.12); they also appear in seismic sections B, D, and G: faults F-106 and F-100 in section B, F-100 and F-106 in section D, F-14, F-106 and F-100 in section G. Main strike direction is approximately N65°E. Seabottom deformation along fault F-100 is consistent with reverse dip-slip component (Figure 3.12); reverse component is also observed in seismic sections D and B.
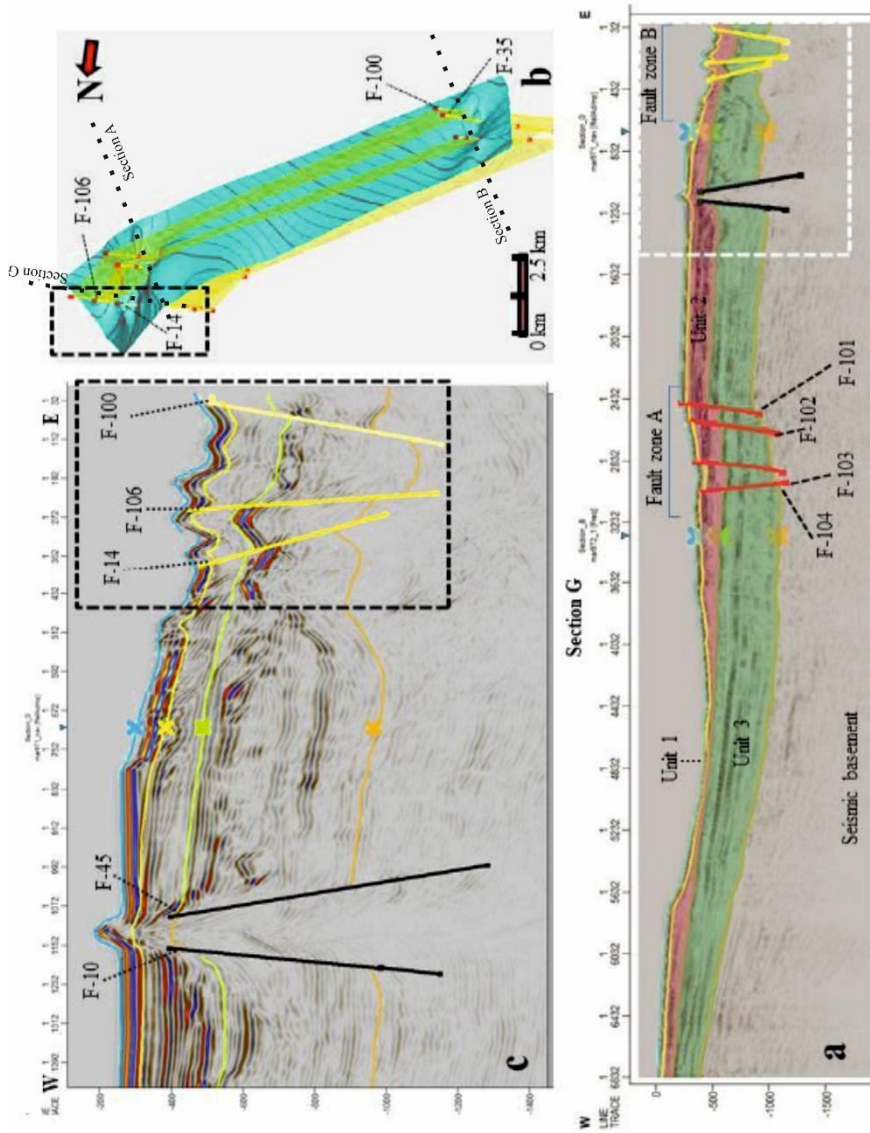
*Figure 3.12. (a) Structural interpretation of ca. 42-km-long W–E-trending seismic section G. Dashed rectangle shows location of Figure 'c'. Two fault zones (A and B) in red and yellow are interpreted. Two black faults indicate inactive structures. Seabottom deformation in this area is an artifact and produced by seismic data processing error. (b) Surface generated from horizon 1 to indicate fault zone B and (c) zoomed picture of the dashed rectangle in 'a'. Fault sticks indicated with yellow color also appear in seismic sections G, D and B. Note reverse dip-slip component of fault F106 and F14 in fault zone B (c). Note also the drag folds in the hanging walls of faults F-10 and F-45 and narrow horst in-between. The fault F-101 appears displacing the sea floor while faults F-10 and F-45 terminates within seismic unit 2; the relationships are consistent with active and inactive nature of these structures, respectively. See Figure 3.1 for location of the seismic section.*

Change in dip direction of fault F-100 is pronounced and may used as evidence to support dominant strike-slip (with minor reverse component) nature of fault segments in fault zaone A. Similarly, deformation of the sea floor along fault F-101 confirm recent, possible Pleistocene –Holocene, activity of the fault zone.

In addition to fault zone A and B; two more structures are also interpreted; faults F-10 and F-45 (Figure 3.12a, c). They dip away from each other and define a narrow-horst structure in-between. The hanging walls seem to move downward and this is well illustrated by the normal draging of horizon 3, the upper boundary of the seismic unit 3. The faults cut and displace the horizon 3 and 4 but seems not affecting horizon 2, the upper boundary of the unit 2. The contact relationhips between the fault and seismic units supports the contention that they are inactive structures.

### 3.2.4. Seismic and Structural Interpretation of Seismic Section D

NW−SE-oriented seismic section D has a total length of 84.87 km (Table 3.1) and is the first seismic section between Marmaris and Fethiye bays. It is the closest section to the shoreline among NW−SE seismic sections (Figure 3.1). The seismic section is the longest among others. Sea bottom is almost horizontal until the Basin A, which is located at the continental slope where sea bottom gets lowered up to 2000 ms.

Three major fault zones are identified and they display a typical horst-and-graben structure. The faults appear to bound three basins and interveining relatively narrow horst areas in-between; the basins are labelled as basin A, B and C (Figure 3.13). In addition to the basin-bounding faults, there is a fourth group of structures (labelled fault zone B) that comprises two steeply-dipping to almost vertical fault segments, F-100 and F-106. They appear to be active structures and deform almost horizontal sea bottom (Figure 3.13a, b). The almost vertical geometry is interpreted to relate a strike slip fault character.
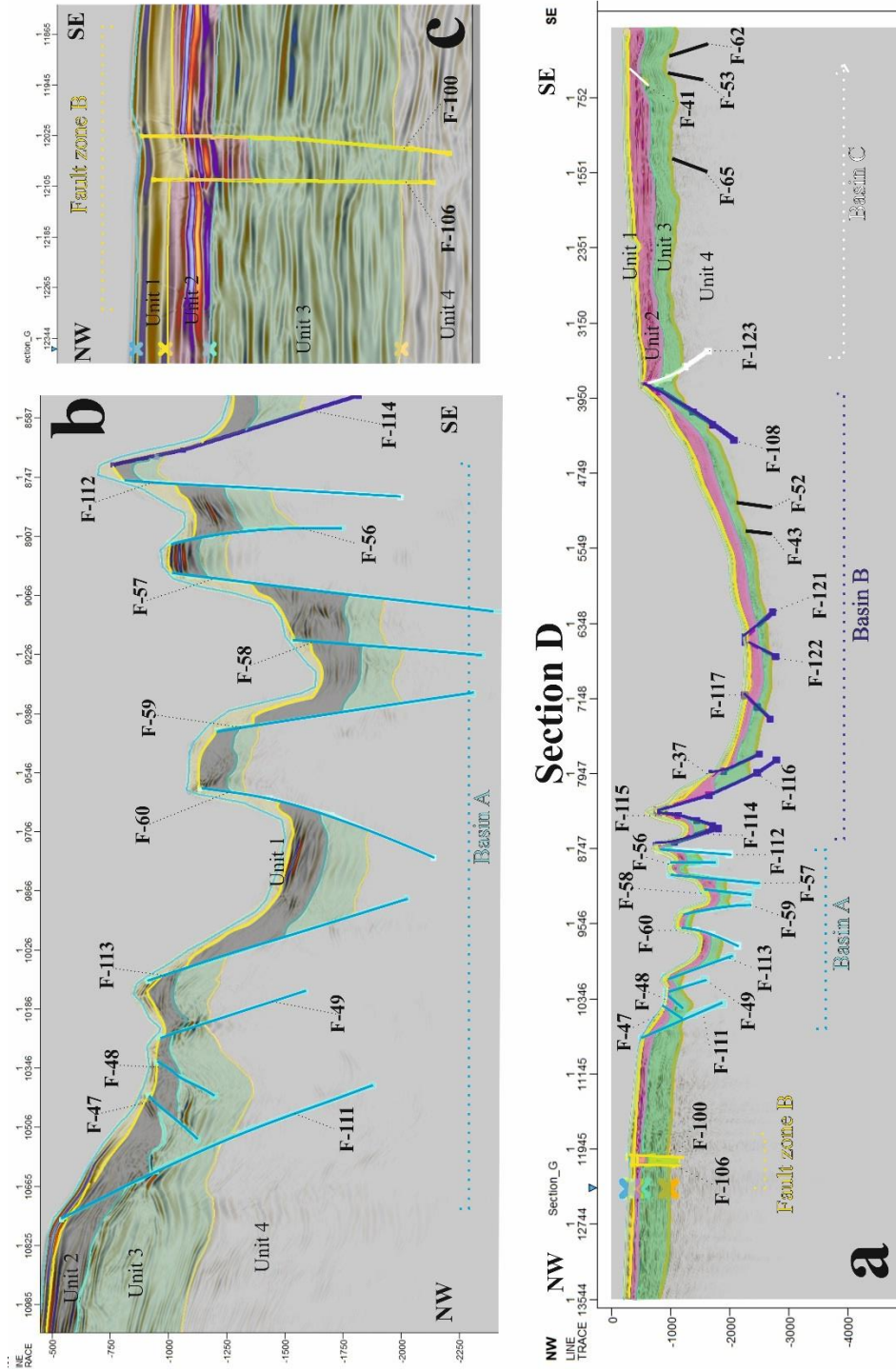
Figure 3.13. (a) Structural interpretation of ca. 85-km-long NE–SE-trending seismic section D. Three basins and intervening ridges/horsts are defined. The basins are bounded by oppositely dipping faults. (b) Close-up view of the basin A. Note that the basin is internally deformed and comprises several sub basins and intervening narrow ridges/horsts. The ridges and bounding faults (blue in color) appear to deform the unit 1 (yellow in color) and the sea floor, attesting recent activity along these structures. (c) Close-up view of two almost vertical fault segments located to the northwest of basin A. They also appear to deform almost horizontal sea bottom, suggesting a possibly Pleistocene–Holocene activity. See Figure 3.1 for location of the seismic section.

58

Basin A is bounded by two main fault segments: N66°E-oriented SE-dipping F-111 in the northwest and N70°E-oriented NW-dipping F-112 in the southeast. They are interpreted as basin-bounding stuctures. Basin A also appears in seismic sections D, B, and A. The basin A itself comprises several subbasins and interveining narrow horsts/ridges in-between. Three main ridges occur at CDP 9546, CDP 9000, and CDP 8747, and they all clearly deform the sea bottom (Figure 3.13b). The offset of sea floor along ridge-bounding faults suggest that these structures are active.

Second basin is observed at middle parts of the seismic section D; the basin B is relatively wider and deeper relative to other two basins (Figures 3.13a and 3.14c). These two basins, basin A and B, are seperated by a ridge area bounded by faults F-112 and F-114 (Figures 3.13a and 3.14a, c). In seismic section C, seabottom morphology is deformed by some active channels at CDP 2350. The channel system creates sea bottom deformation in a zone of about 250 m wide (Figure 3.15). Basin B bounded by F-116 in the northwest and at the fault F-108 in the southeast (Figure 3.14c). There appears a considerable vertical elevation difference between the top of the bounding ridges (ca. 500 ms) and the deepest part of the basin (ca. 2250 ms). Basin B is a prominent structure and appears in seismic sections A, B, C, and D. Two boundary faults, F-114 and F-116, are observable in seismic sections A and D. Bounding fault F-116 in the northwest also appear in section B. Whereas bounding fault F-108 in the southeast occur in seismic section C.

Basin C is placed at southeastern flank of the Basin B where sea floor appears almost horizontal (Figure 3.14b). It occurs at continental shelf where sea bottom depth is 400–500 ms. Observable width of the basin C in section D is almost 23 km. Basin C is bounded by fault F-123 in the northwest whereas southeastern boundary fault does not occur in seismic sections of the present study. The bounding fault F-123 also occur in seismic sections A, C, and D. Intense internal deformation of the basins A and B appear not obvious in Basin C; this may be due to inactive nature of bounding fault(s) along the SE of the basin.
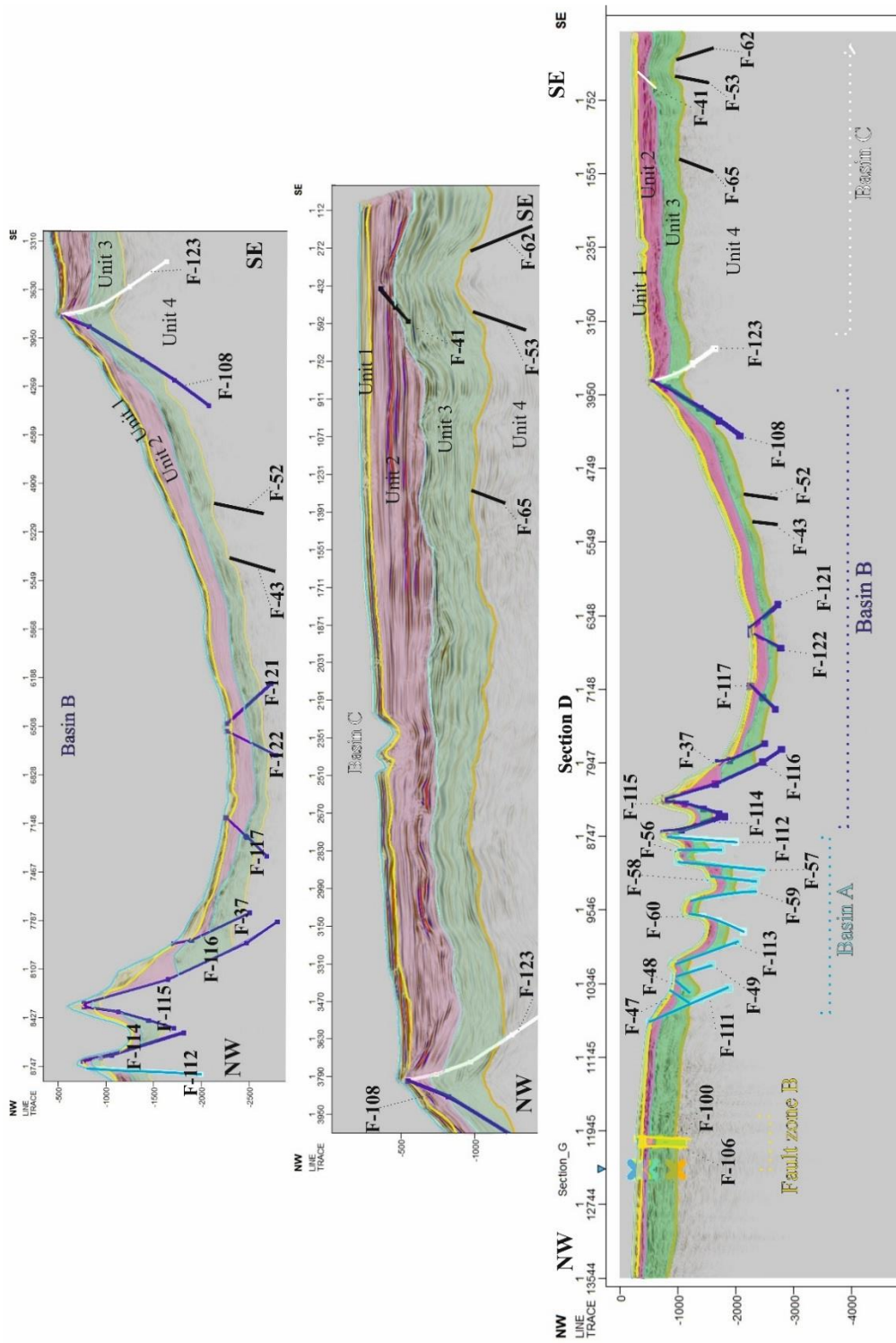
Figure 3.14. (a) Structural interpretation of ca. 85-km-long NE–SE-trending seismic section D. See Figure 3.13 for more explanation. Close-up views of the basins C (b) and B (c). Note that the basin-bounding faults cut and displace the different seismic units and the almost horizontal sea floor. See Figure 3.1 for location of the seismic section.

60

The faults bounding three basins are oriented in NE−SW direction (Figures 3.13 and 3.14); a direction perpendicular to seismic section D orientation. The section D is therefore important for interpretation of all basins and bounding fault zones.

### 3.2.5. Seismic and Structural Interpretation of Seismic Section C

NW−SE-oriented seismic section D has a total length of 50.24 km (Table 3.1) and is the first seismic section between Marmaris and Fethiye bays. It is the second closest section to the Fethiye Bay shoreline among NW−SE seismic sections (Figure 3.1). Two basins, basin B and C, are interpreted at the continental shelf (Figure 3.15). Sea bottom is almost horizontal until the basins; basin C occurs between 900 ms and 1250 ms whereas basin B is relatively depper and occurs between 1250 ms and 3000 ms. In the section, the width of the basin C is almost 17.5 km (Figure 3.15).

Basin C is bounded by SE-dipping fault F-123, like in other seismic sections A and D. Along this section, basin C appears relatively more deformed and is dissected by a number fault segments that bound a narrow ridge. The ridge bounding faults F-124, F-125, F-46 and F-5 appear to cut and displace the sea floor (Figure 3.15b), attesting their recent activity. Similar ridge structure bounded by the similar faults also occur in seismic section A (see Section 3.2.7).

There are also relatively smaller fault segments, F-3, F-2, and F-8; as they do not reach the sea bottom and appear to deform unit 3 only (Figure 3.15b), these faults are interpreted as inactive structures.

Basin B is bounded by NW-dipping fault F-108 like in other sections A and D. There appears a narrow ridge at the center of the basin; the ridge is bounded by fault segments F-121 and F-122 (Figure 3.15a). Similar ridge is also defined in seismic sections A and D (see Sections 3.2.6 and 3.2.7). The ridge and bounding faults appear to deform and displace the seabottom and indicate their recent activity. In seismic section C, seabottom morphology also appear to be carved by some active channels observed at CDP 5300 and CDP 3700 (Figure 3.15b).
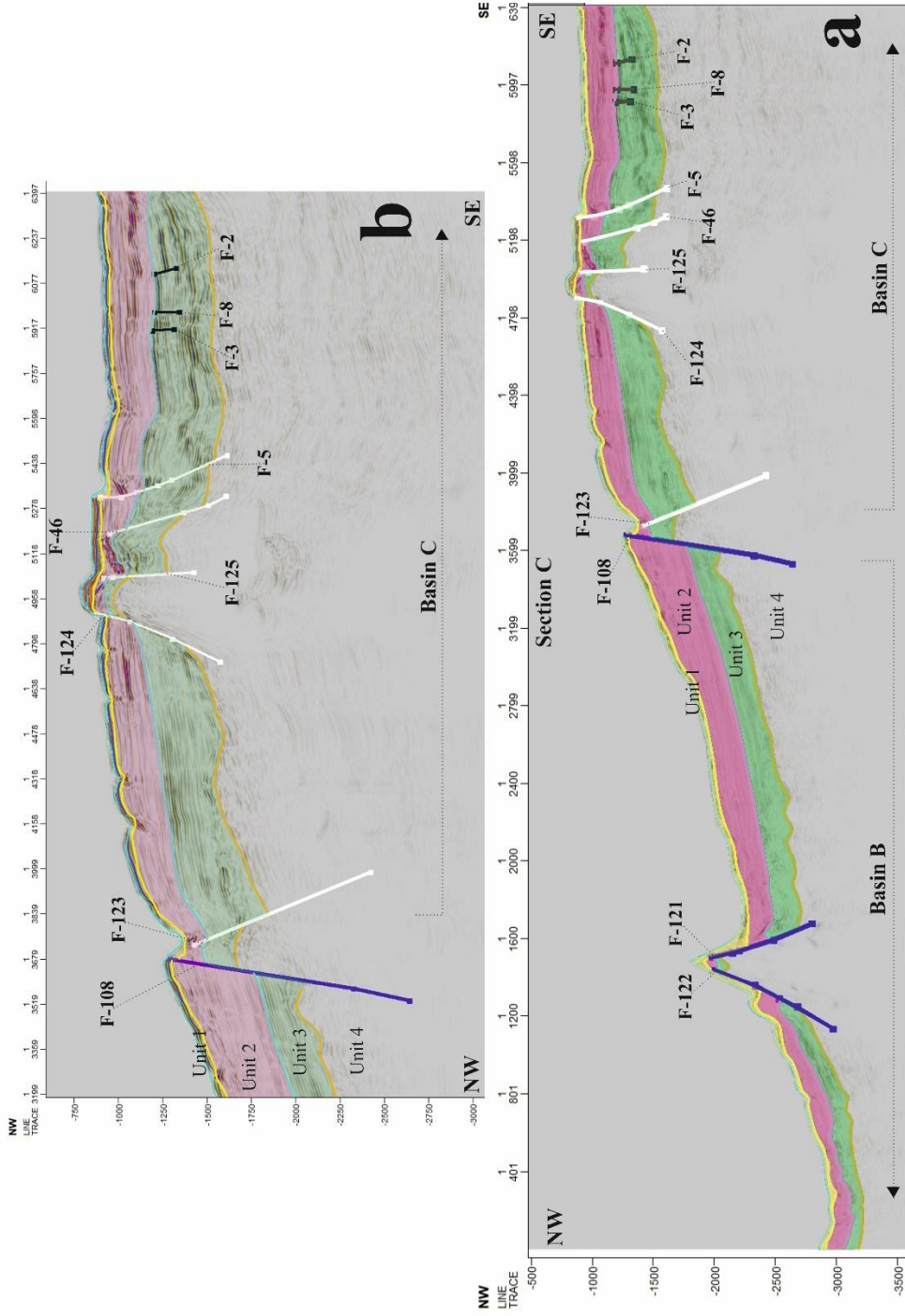
Figure 3.15. (a) Structural interpretation of ca. 50-km-long NE–SE-trending seismic section C. The interpreted faults define two basins, basin B and C. (b) Close-up views of the basin C. Note narrow ridges at the center of basins B and C. The ridge and bounding faults in both basins cut and displace the sea bottom and confirm their recent activity. Note also that seabottom morphology appear to be carved by some active channels at CDP 3700 and CDP 5300. Dark blue and white faults are interpreted active, while black lines represent inactive faults. See Figure 3.1 for location of the seismic section.

62

### 3.2.6. Seismic and Structural Interpretation of Seismic Section B

NW−SE-oriented seismic section D has a total length of 61.62 km (Table 3.1) and is the one of the farthest seismic section to the shoreline in the Fethiye bay among NW−SE seismic sections (Figure 3.1). Sea bottom occurs at 200 ms and 2600 ms in the northwest and southeast parts of the seismic section B, respectively.

Six different fault groups are identified and they are all shown in different colours (Figure 3.16). **Red faults** occur at CDP 3200 and consist of 5 segments (F-104, F-103, F-18, F-102 and F-101). Change dip direction of the fault F-102 is pronounced and suggest strike-slip nature of these fault segments. Similar character of the F-102 is also reported in seismic  section E (Figure 3.10). **Black faults** occur between CDP 3700 and CDP 5200; eight faults (F-21, F17, F-11, F-40, F-31, F-32, F-33 and F-30) are intepreted as inactive faults. They might have played important role in deformation of seismic *unit 3* only (see Discussion Chapter for more information).

**Light green faults** occur between CDP 5250 and 5600 placed between continental shelf and slope. This fault zone consists of there fault segments (F-131, F-132 and F-28) and also appear in seismic section A between continental shelf and slope (see Section 3.2.7). F-28 occurs in seismic section B. Reverse component of fault F-131 and normal component of fault F-132 appear clearly in seismic sections A and B (Figures 3.16a and 3.17a). This fault zone forms boundary between continental shelf and transition zone (Figure 3.16a). **Yellow faults** at CDP 4300 and consist of 3 segments (F-106, F-35, and F-100); they occur between two clusters of black faults. Among fault segments, fault F-100 appear to cut and displace the sea floor whereas the other two segments terminate within seismic *unit 1* (Figure 3.16a). This relationship between the yellow faults and sea bottom is attributed to their activity.
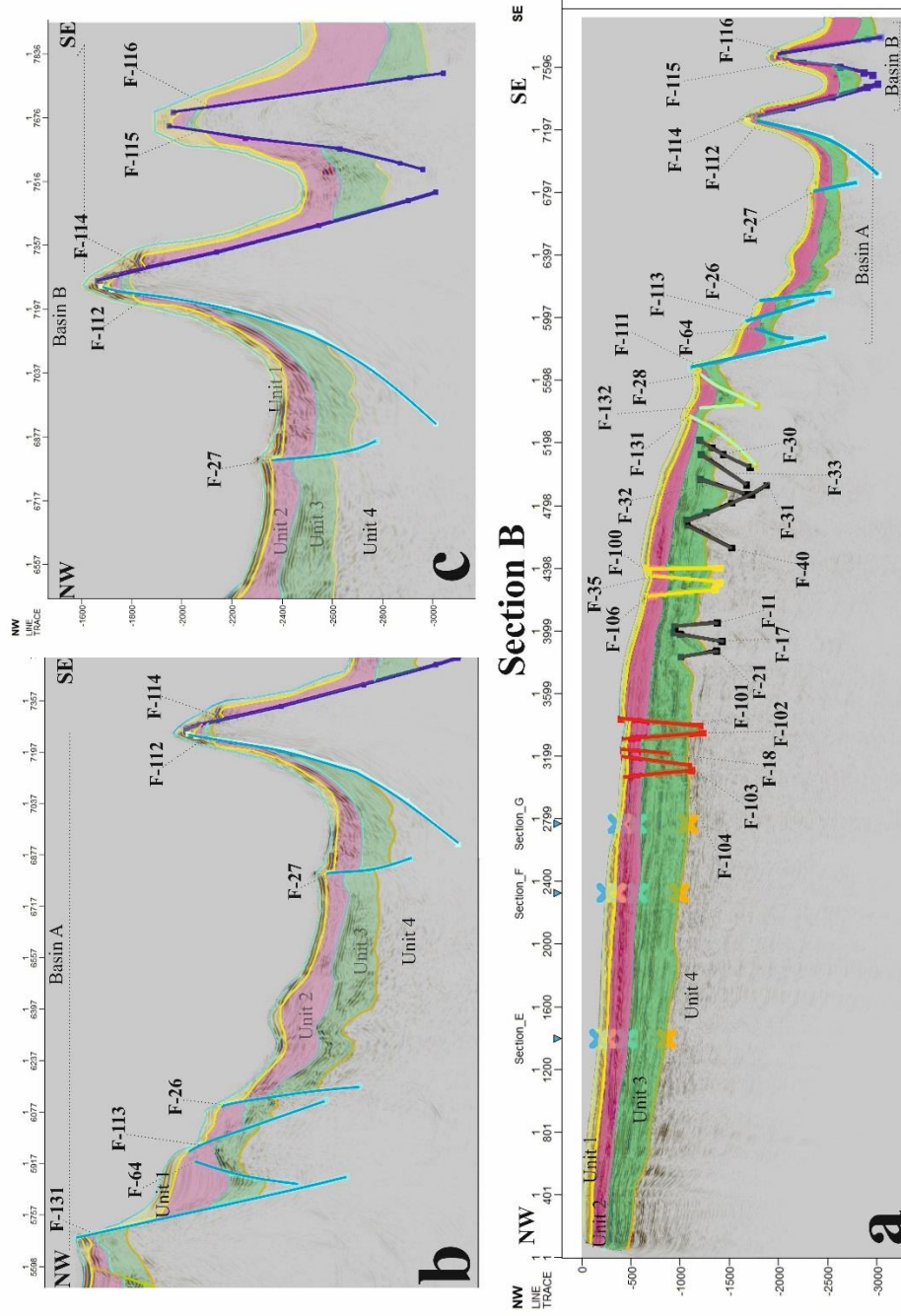
*Figure 3.16. (a) Structural interpretation of ca. 62-km-long NE–SE-trending seismic section B. Six fault zones are interpreted and each is illustrated with different colors. (b, c) Two basins (basin A and B), separated by a narrow ridge, are defined. Among the fault segments, red, yellow and basin bounding (blue and navy) faults appear to cut and displace the sea floor; they may represent active faults in the seismic section, while black faults are inactive structures that deforms unit 3 only. Note that green fault F-131 has a reverse displacement, but the rest appear to display normal motion. Note also a narrow ridge within basin B; F-115 and F-116 form ridge-bounding faults. Southwest extension of the basin B occurs in seismic section C. See Figure 3.1 for location of seismic section.*

Two major basins, basins A and B, are defined; they are bounded by two sets of faults (**blue and navy coloured faults)** in Figure 3.16). The two basins are separated by a narrow ridge that deforms the sea floor (Figure 3.16b, c). The bounding fault segments F-111 and F-114 also occur in seismic section B (see Section 3.2.7). Width of the Basin A is narrower than the one desribed in seismic section D (Figures 3.13 and 3.14). The northwestern margin of the basin B appears in the seismic section and is bounded by fault F-114 (Figure 3.16). The basin extends towards SE, which is observable in seismic section C. The basin B is also dissected by a narrow ridge; faults F-115 and F-116 occur as ridge-bounding structures (Figure 3.16c).

### 3.2.7. Seismic and Structural Interpretation of Seismic Section A

NW−SE-oriented section-C total length is 58.11 km (Table 3.1) and is the one of the farthest seismic section to the shoreline in the Fethiye bay among NW−SE seismic sections (Figure 3.1). Sea bottom occurs at 900 ms, 4400 ms and 2500 ms in the northwest, centeral and southeast parts of the seismic section A, respectively.

Basins A, B and C also occur in seismic section A. The width of basins is different than in other seismic sections. For example, the width of the basin A is almost 8.5 km and is much narrower than what is in all other sections. Basin A is bounded by fault segments F-111 and F-114 (blue coloured faults in Figure 3.17a). The northwestern margin of the basin is steeper and bounded by fault segments F-111 and F-112 with a normal dip-slip component. Change in dip direction of the fault F-102, as shown in section E (Figure 3.10), is important for describing the basin-bounding fault zone and suggest strike- slip faulting with normal dip-slip component. To northwestern margin of the basin A, there is another fault zone (light green coloured faults in Figure 3.17a and 3.18b) being interpreted at CDP 8600; these faults (F-132 and F-131) are placed between continental shelf and slope. Reverse dip-slip component of the fault F-131 and normal component of the fault F-132 are also reported in seismic section B (Figure 3.16).
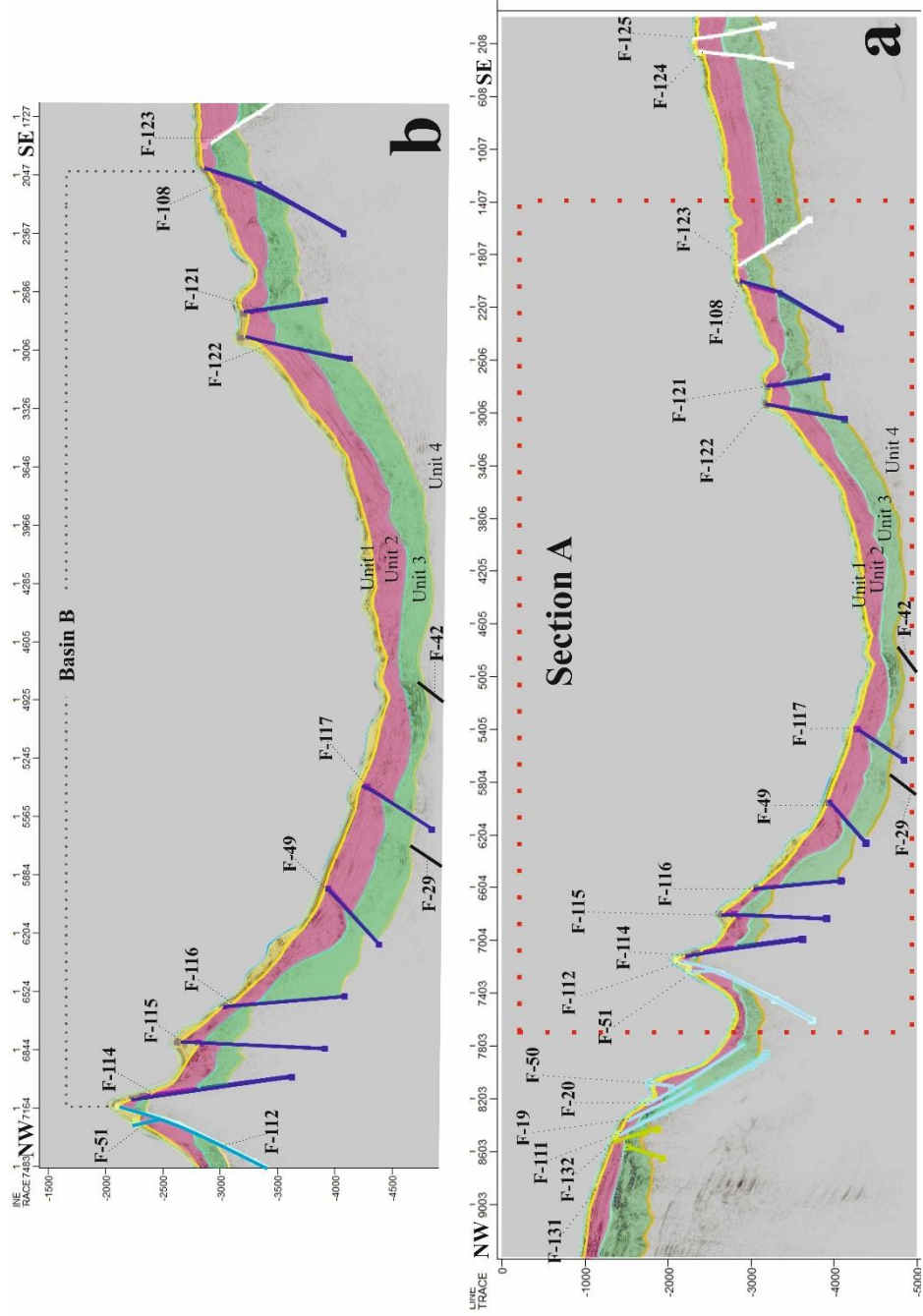
*Figure 3.17. (a) Structural interpretation of ca. 58-km-long NE–SE-trending seismic section A. Basins A, B and C are also defined along this section. (b) Close-up view of the basin B. Note that some faults have pronounced reverse dip-slip component (F-132, F-117 and F-49) while the rest display normal motion. The basins are separated by narrow ridges; their bounding structures deform the sea bottom and suggest that they are active structures. See Figure 3.1 for location of seismic section.*

The fault zone bounds continental shelf at the northwestern part of the seismic section A (Figure 3.17).

The basin B forms the most prominent feature of seismic section A. Wide basin (almost 32 km) is bounded by fault segments F-114 in the northwest and F-108 in the southeast (Figure 3.17). Faults F-122 and F-121 appear to define a narrow ridge within the ridge; they also occur in seismic sections C and D (Figures 3.13 and 3.14) but associated seabottom deformation is more significant in this section (Figure 3.17b). The two fault segments and intervening narrow ridge are also described in seismic section A (Figure 3.167). Two more faults (F-115 and F-116) are interpreted along the northwestern margin of the basin A; these structures appear to deform sea bottom as in seismic sections B and D (Figures 3.13 and 3.14). Navy fault segments (F-49 and F-117), that occur between CDP 5400 and 6200 within the basin B, display a pronounced reverse component and deform all of the seismic units, but not *unit 1* (Figures 3.17 and 3.18). These structures are defined only in seismic section A. Black faults that occur between CDP 3700 and 5200 within the basin B are inactive faults; they might have played important role in deforming the seismic *unit 3* (See Discussion Chapter for more information).

Basin C occurs at the southeastern part of the seismic section A and is bounded by fault segment F-123. There is a narrow ridge bounded by faults F-124 and F-125 near northwestern margin of the basin. The ridge is also described in C (Figure 3.14); it appears to create relaticely less sea bottom deformation at CDP 2000 (Figure 3.17).

### 3.3. 3D Structural Interpretation and Basin Analysis

3D sections provide the opportunity to see the extension and character of faults separately in each seismic section at the same time. For that reason in structural interpretation, using 3D seismic sections gives better results. Basin analysis and relationship between each other are investigated at this part. Basins are already mentioned chapter 3 going to be discussed and analyzed.
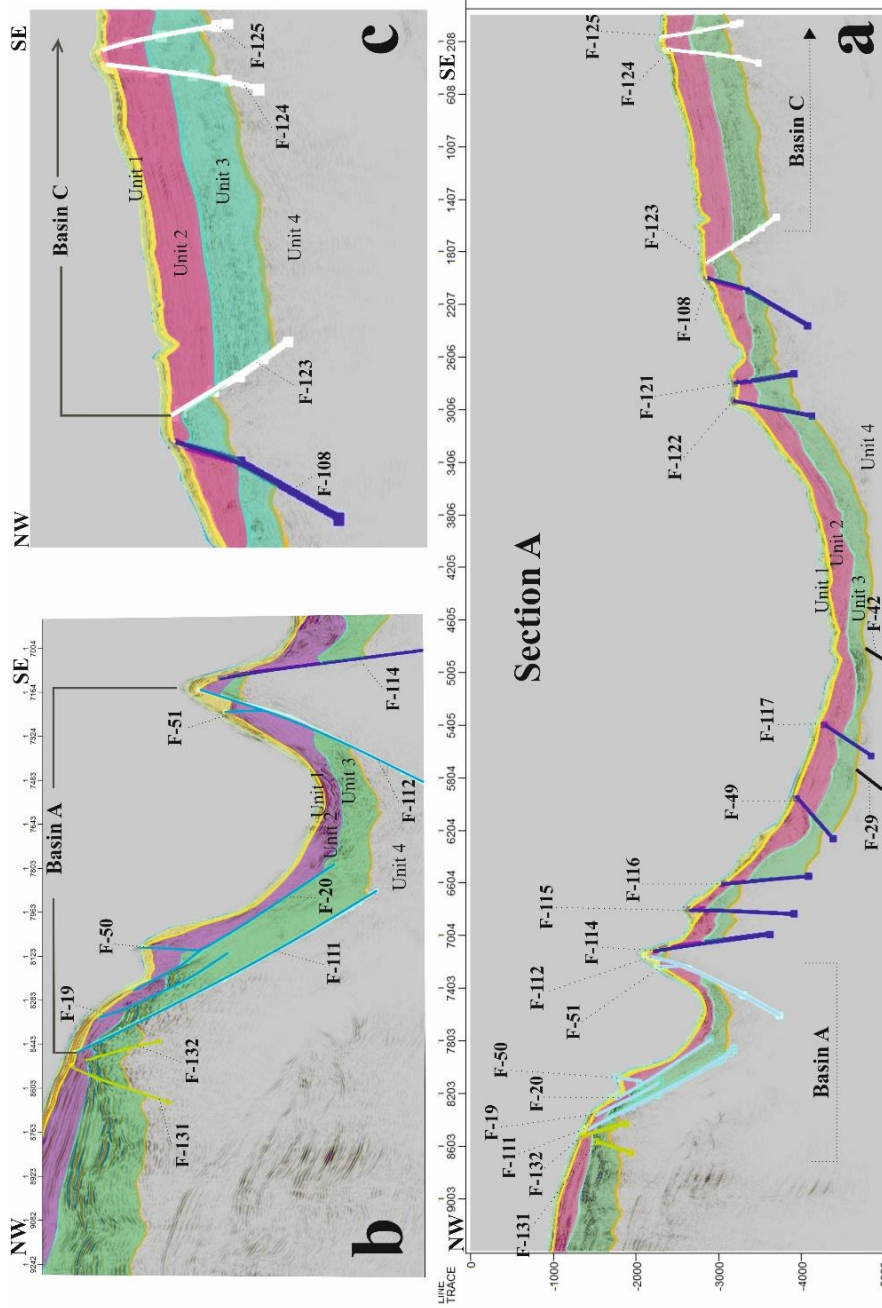
Figure 3.18. (a) Structural interpretation of ca. 58-km-long NE–SE-trending seismic section A. Basins A, B and C are also defined along this section. Close-up view of the basin B and (b) basin C; (c). Note a intrabasinal high in basin B; it is defined by a relatively small-scale fault antithetic to the basin-bounding faults at the northwestern margin of the basin A. Similarly, the boundary between basins B and C is marked by a narrow ridge and fault segments F-108 and F-123 are ridge-bounding structures. Note also that these faults terminate against seismic unit 1. There appears another small-scale ridge within basin C; the bounding fault segments F-124 and F-125 appear not to cut sea floor but the pronounced deformation between two faults appear as a ridge at sea floor. The basin-bounding structures of basins A, B, and C are represented by light blue, navy and white lines, respectively. See Figure 3.1 for location of the seismic section and Figure 3.17 caption for more information.

68

### 3.3.1. Seismic Interpretation of the Basin A

Basin A is interpreted in seismic sections A, B, and D and occurs at continental slope bounded by faults F-111 in the northwest and F-112 in the southeast. The basin-bounding faults F-111 and F-112 dip southeast and northwest, respectively; both display normal dip-slip component. They are interpreted as normal faults with a strike-slip component; this is also supported by moment tensor inversion solutions of the events related with these two faults (see Chapter 4 for more information).

Width of the basin A is variable from one section to another; it is about 8.5 km, 10 km and 12.5 km in seismic sections A, B, and D, respectively. Basin center line trends almost in NE–SW direction, almost parallel to the bounding structures. It seems to have rather wedge-shape geometry where basin width increases from northwest to southeast.

Depositional sequence in the basin A consists, form the bottom to the top, of seismic units 3, 2 and 1, respectively. When basin A started to form, seismic *unit 3* was deposited unconformably above the basement; this erosional surface is labelled as horizon 4, which forms the upper boundary of the seismic basement (seismic *unit 4*).

Total thickness of the seismic units in the basin A also differs from one seismic section to another. Maximum and minimum total thickness observed in sections A, B and D are 350 ms and 200 ms, 1050 ms and 500 ms, and 600 ms and 330 ms, respectively (Figure 3.19). 330 ms thickness is measured at the top of the ridge in section D at CDP 9400 (Figure 3.19d). Basin A is therefore placed at the continental slope and is bounded by faults with normal component; there are also characteristic intrabasinal high(s)/ridge(s) within the basin.
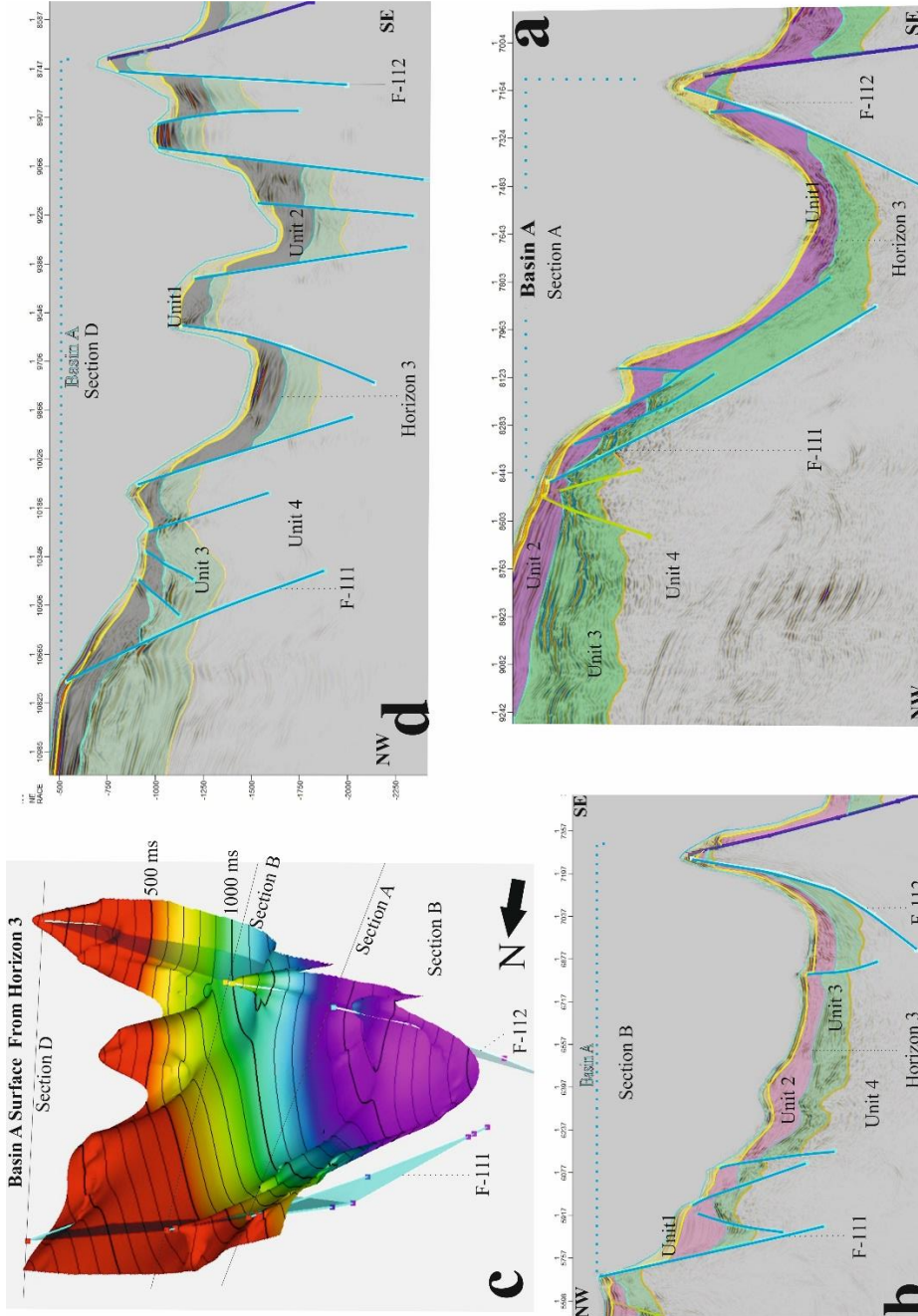
Figure 3.19. (a–c) Interpretation of Basin A in seismic sections A, B, and D; (c) basin surface prepared from integration of horizon 3 from all sections. The basin is relatively a narrow feature and is bounded by high-angle faults with considerable normal component. The basin-bounding faults appear to deform the sea floor, thus suggesting that these faults are active structure and that the basin growth still continues. Steep basin margins attest their fault-controlled nature. There are also intrabasinal highs/ridges within the basin as is seen in seismic section D (c). The horizon 3 surface clearly illustrates that the basin becomes deeper towards southeast and that there are several rather narrow intrabasinal highs/ridges.

Width of the basin A is variable from one section to another; it is about 32, 28, 22.5 and 4 in seismic sections A, B, C, and D, respectively. Basin center line trends almost in NE–SW direction, almost parallel to the bounding structures. Unlike basin A, the width of the basin B increases from southeast to northwest (Figure 3.20).

**3.3.2. Seismic Interpretation of the Basin B**

Depositional sequence in the basin B comprises, form the bottom to the top, seismic units 3, 2 and 1. Seismic *unit 3* forms the first and oldest unit that marks the commencement of the basin B. Unit 3 overlies the erosional surface horizon 4 above the seismic basement. Thus the lower boundary of the *unit 3* is a regional unconformity. The basement boundary (horizon 4) appears to be affected, at least, more than one phase of deformation; and this is totally different from horizons 1, 2, and 3. This issue is going to be discussed in Discussion Chapter.

Total thickness of the seismic units in the basin B also differs from one seismic section to another. Maximum and minimum total thickness observed in sections A, B, C and D are 750 ms and 500 ms, 1000 ms and 400 ms, 1500 ms and 600 ms, 1500 ms and 600 ms, respectively (Figure 3.19). 600 ms thickness is measured at the top of the ridge in sections C and D at CDP 1500 (Figure 3.20a) and CDP 8300 (Figure 3.13a), respectively (Figure 3.19d). Basin B therefore occurs at the continental slope and is bounded by faults with normal component; intrabasinal high(s)/ridge(s) form characteristic features within the basin.

**3.3.3. Seismic Interpretation of the Basin C**

Basin C is interpreted in seismic sections A, C, and D at the continental slope; the basin is bounded by fault F-123 in the northwest whereas the southeastern boundary of the basin is not observed in any 7 seismic sections. The basin-bounding fault F-123 dips southeast and has normal dip-slip component (Figure 3.21). The fault F-123 is interpreted as normal faults with a strike-slip component, which is also supported moment tensor inversion solutions of the events related to the fault (see Chapter 4 for more information).

71
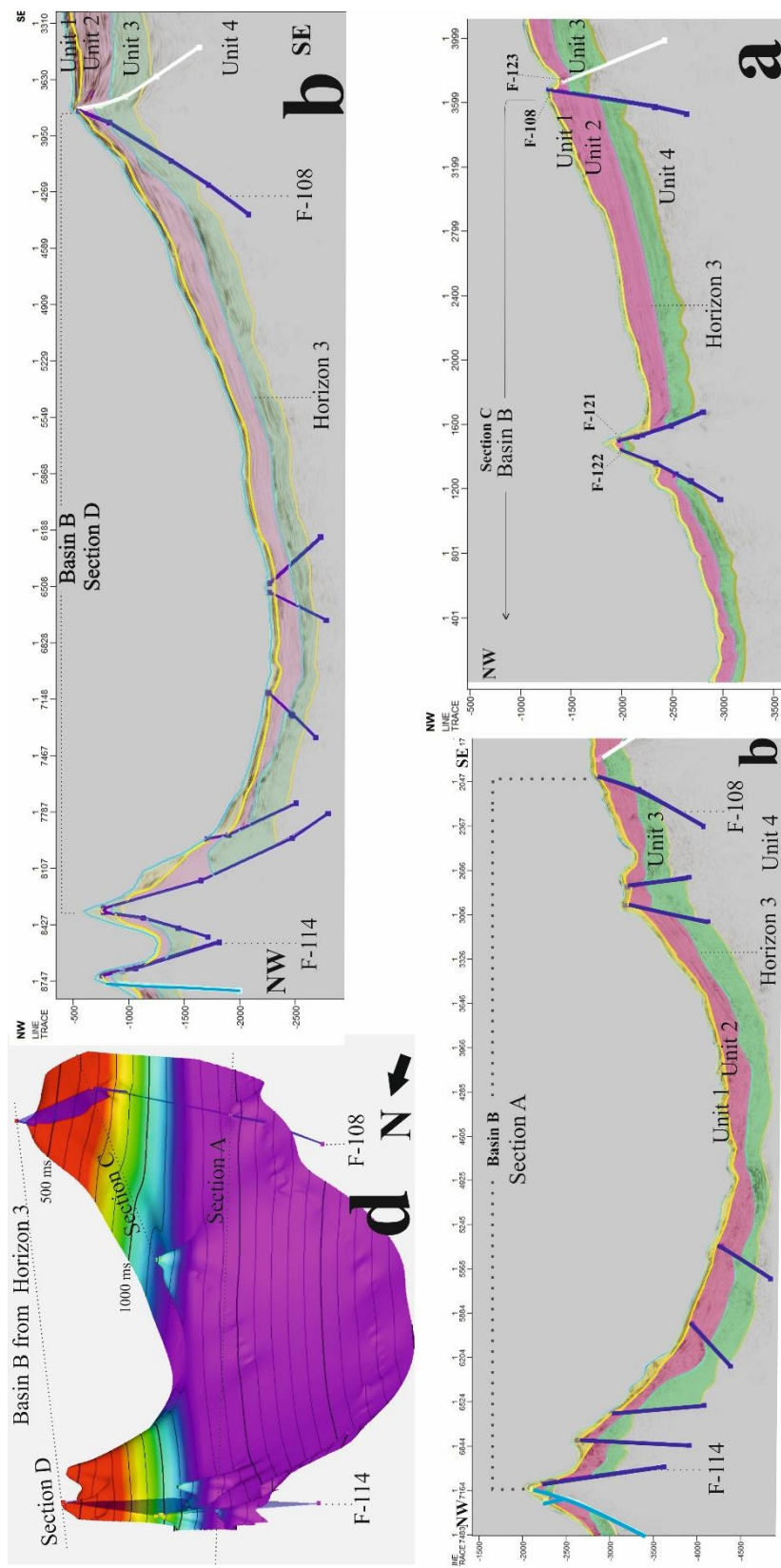
*Figure 3.20. (a–c) Interpretation of Basin B in seismic sections A, C, and D; (c) basin surface prepared from integration of horizon 3 from all sections. The basin is relatively a wide feature and is bounded by high-angle faults with considerable normal component. The basin-bounding faults appear to deform the sea floor, attesting their recent activity. The northwestern margin appear steeper compared to its southeastern margin. This may suggest that the former margin is relatively more active and that the actively growing basin B is an asymmetric structure. There are also intrabasinal highs/ridges within the basin as is seen in seismic section B (a). The horizon 3 surface confirms deepining of the basin towards southeast.*

72
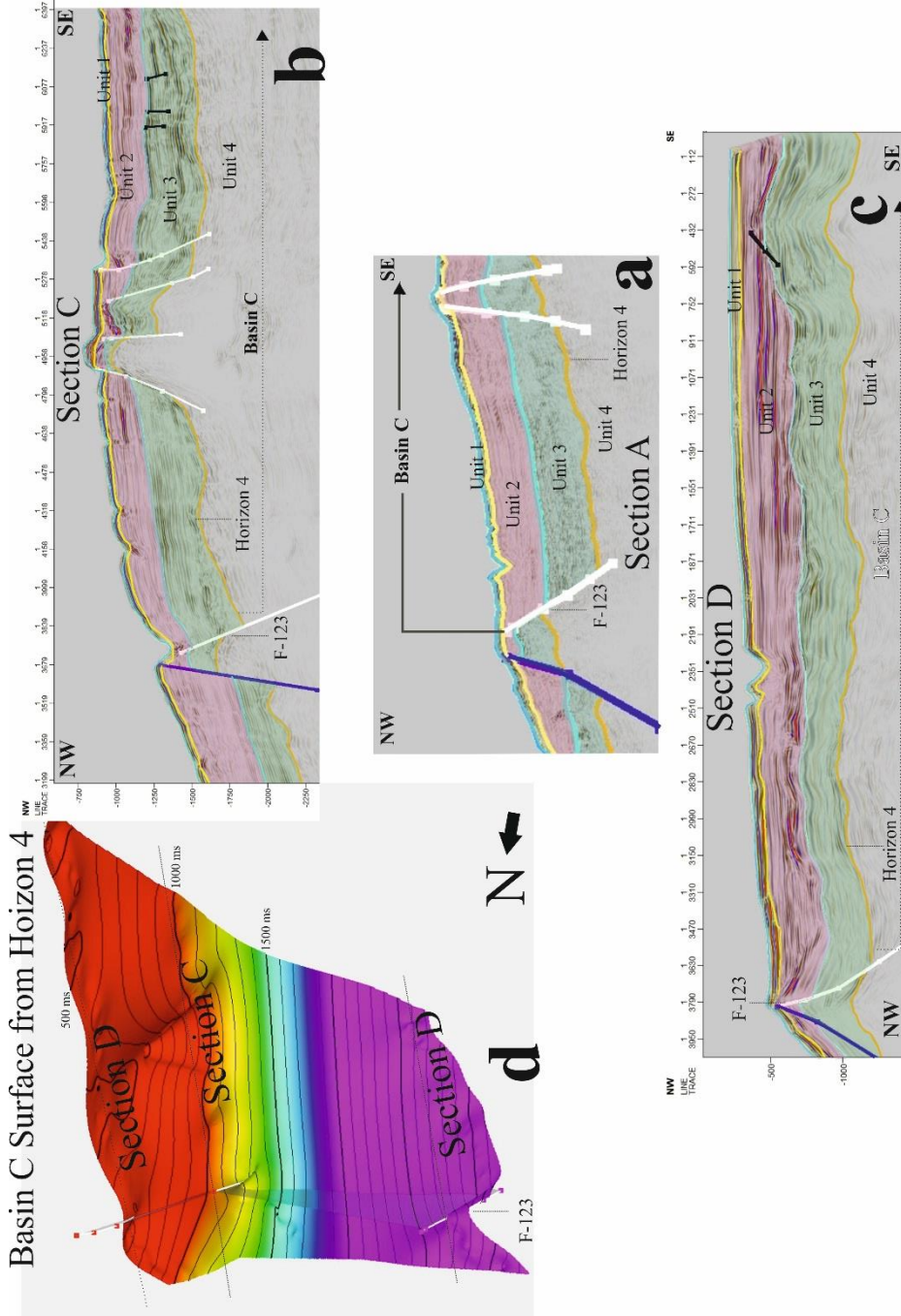
Figure 3.21. (a–c) Interpretation of Basin C in seismic sections A, C, and D; (c) basin surface prepared from integration of horizon 4 from all sections. The basin is relatively a wide structure with its northwestern margin defined in the seismic sections. The seafloor at the northwestern margin appears not deformed along basin-bounding fault F-123.There are intrabasinal highs/ridges within the basins as illustrated in 'a and c'. The ridge-bounding faults in 'c' appear to cut and displace the seafloor while those in 'a' does not cut the seafloor but deform it to form a ridge. The sea floor appears almost at the same elevation across the seismic sections. The horizon 3 surface confirms deepening (not as pronounced in basins A and B) of the basin towards southeast.

Observed width of the basin C is also variable from one section to another; it is 12, 17.5, 23 km in the seismic sections A, C, and D, respectively. Basin center line trends almost in NE–SW direction, similar to basins A and B.

Depositional sequence in the basin C comprises, form the bottom to the top, seismic units 3, 2 and 1. Seismic *unit 3* forms the first and oldest unit in the basin and it dates the initiation of basin formation. Like in other basins, *unit 3* overlies the erosional surface of horizon 4 above the seismic basement. Thus horizon 4 is a regional unconformity.

Total thickness of the seismic units in the basin C also differs from one seismic section to another. Maximum and minimum total thickness observed in sections A, C and D are 1000 ms and 900 ms, 1200 ms and 400 ms, 950 ms and 750 ms, respectively (Figure 3.19). It appears that there is dramatic difference (about 800 m) in thickness of the basin fill along seismic section C and this arises from a ridge at CDP 4900 (Figure 3.21a).

It appears that there is a considerable variation in the total thickness of the basin fill in all basins; this occurs because of intrabasinal high(s) within each basin and will be discussed in Discussion Chapter.

### 3.3.4. 3D Structural Interpretation of Faults

The 3D structural interpretation allows the faults interpreted in all of the 7 seismic sections to be assembled in a single diagram. First, all seismic sections are placed in three dimensions according to their latitudes and longitudes (Figure 3.22). All faults in seismic sections are transferred to 3D environment. It is therefore easier to monitor the continuity of faults in this window. The character and dip direction of faults and location of fault-bounded basins are used to determine the continuity of each interpreted fault; the result is a 3D structural map of the study area (Figure 3.22). To provide better images, the figure contains major faults only; major fault means any structure that occurs in at least two seismic sections. The fault-bounded basins and their continuity are more obvious in these diagrams (Figure 3.22).
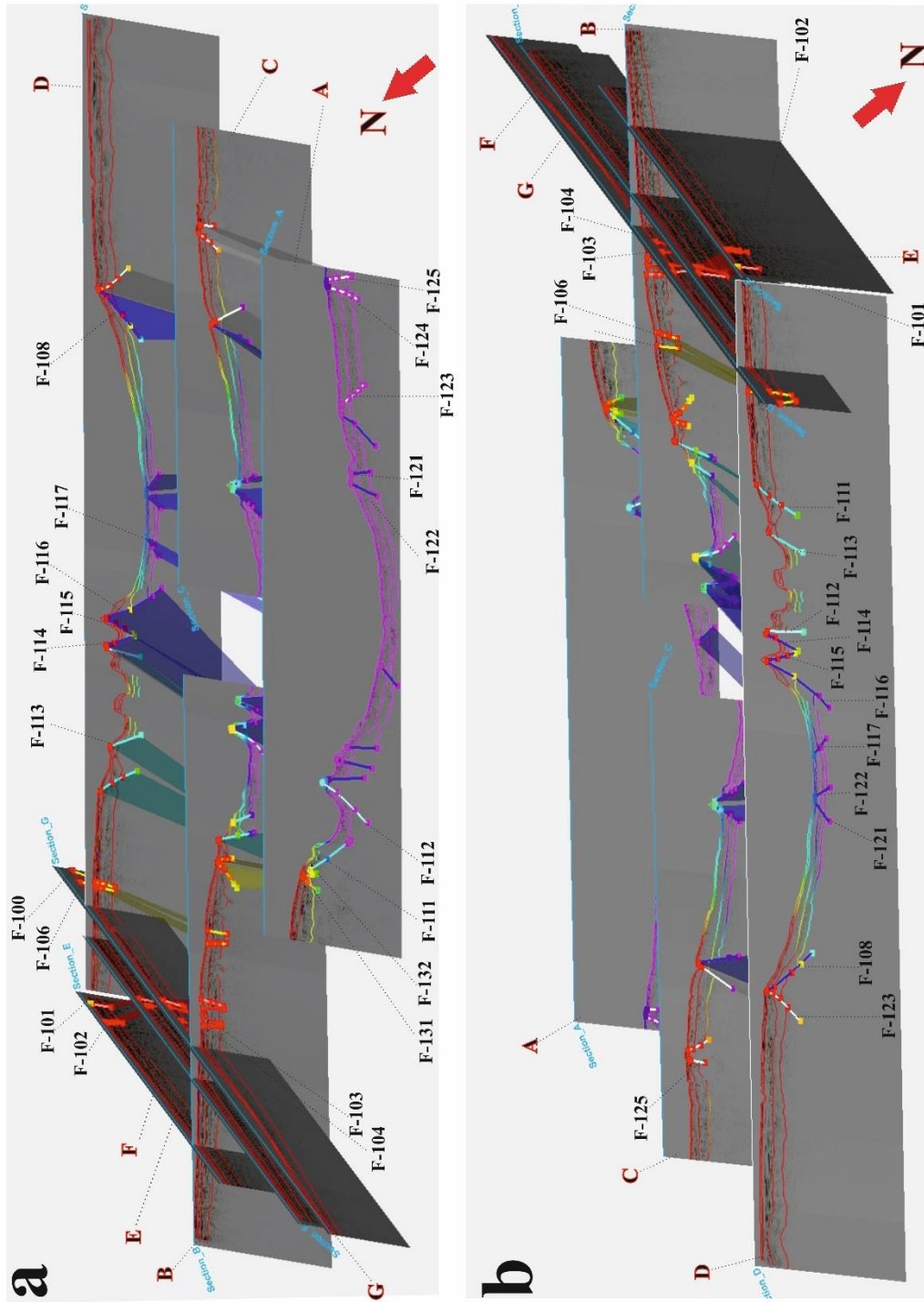
Figure 3.22. 3D structural interpretation of major faults in the study area. (a) view from northwest, red letters indicate seismic section names; (b) view from southeast. The diagram clearly illustrates how basin-bounding major faults and intervening basins continues from one section to another. The diagram forms a base for the fault map in Figure 3.23.

75

The continuum of each major fault is now shown by a line and are all transferred into a fault map (Figure 3.23). It is therefore possible to determine the geometry (strike and dip direction) of faults. The meaning of each fault and their correlation with the results of moment tensor inversion solution of the events occurred in the study area will be evaluated in Discussion Chapter.

In Figure 3.23, Bing maps Hybrid images are used as map base. Spatial on demand's color-hillshade representation of TCarta's and 1/60,000 scale coastline from Landsat imagery Seafloor resolution is 90 m (www.spatialenergy.com). Spatial on demands Global Coverage Bing Maps 30 cm+ imagery is updated in real-time; they are available at the same scale at website www.bingmaps.com.
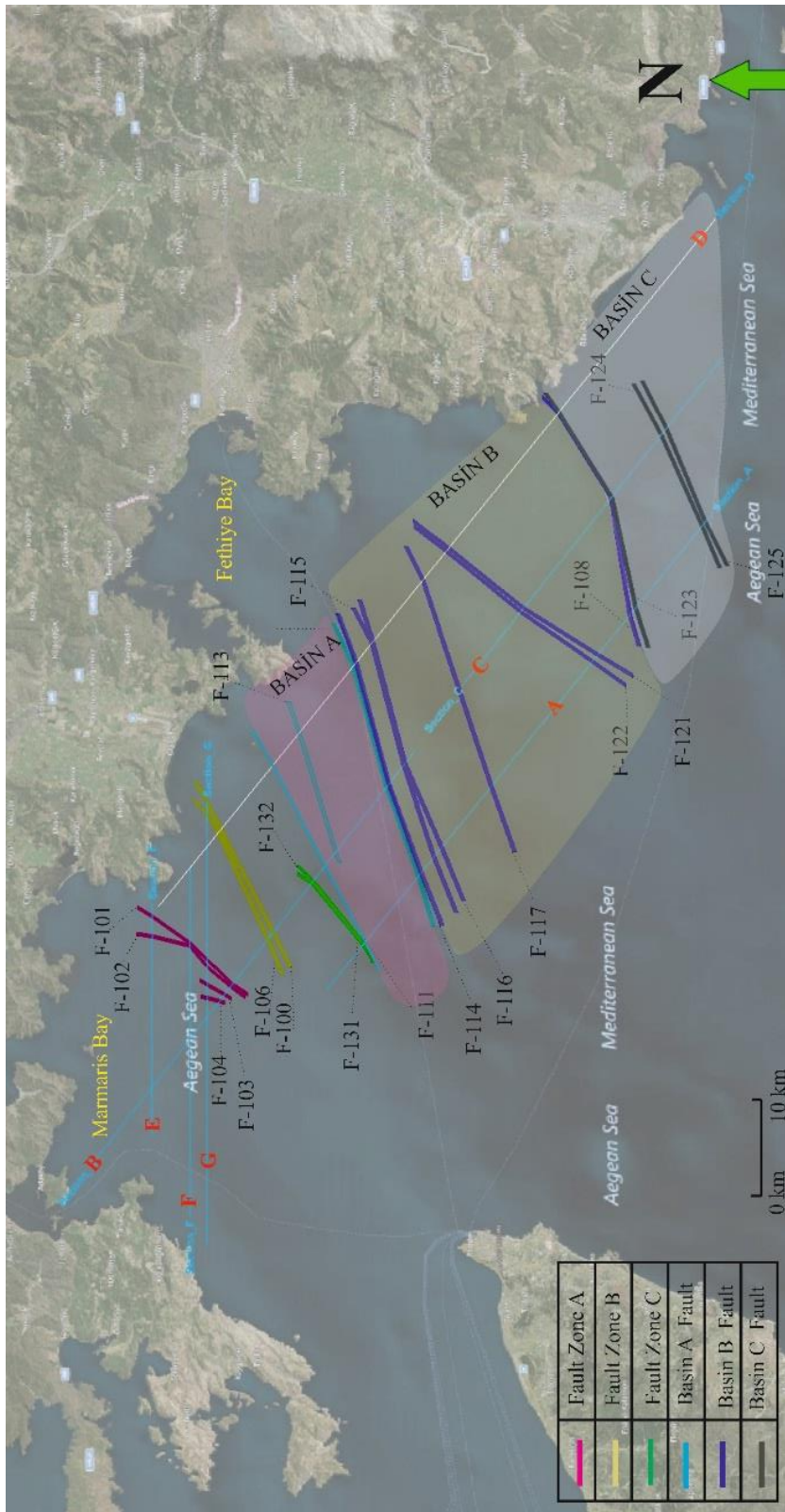
*Figure 3.23. Major fault map of the study area based on seismic interpretation. The map clearly shows that the there are several NE–SE-trending faults and they form bounding structures of three basins.*

# CHAPTER 4

## EVENT MOMENT TENSOR INVERSION SOLUTION

In this chapter moment tensor inversion solution of selected events occurred in the study area are presented. Strike and dip direction of the interpreted faults are already defined by using 2D seismic sections in Chapter 3. Moment tensor inversion solutions of selected events need to be carried in order to clarify type of faulting.

The results of the seismic interpretation and moment tensor inversion solutions will be integrated and evaluated in order to enlighten tectonic structures of the study area (see Chapter 5 for more information).

### 4.1. Event Date and Location

Events occurred after year 2005 are selected because they are thought to have high quality waveforms recorded by local and global seismic networks. Six (6) shallow main events (Table 4.1; Figure 4.1), with magnitudes (Mw) greater than 4 events, occurred near the main faults are chosen to obtain focal mechanism solutions of, and calculate values, such as depth, magnitude, nodal planes, strike, dip, rake, principal axis value, plunge azimuth for a given earthquake. The focal mechanism solutions are obtained by using broadband seismic waveforms. Beachball diagrams are produced and fault-plane solutions (geometry and sense of slip of the fault) are resolved.

### 4.2. Broadband Stations Selection

Waveforms are supplied by national and international seismic recording stations (Figure 4.1): (i) International Federation of Digital Seismograph Networks (FDSN) partners like National Seismic Network of Turkey (DDA), National Observatory of Athens Seismic Network and (ii) Boğaziçi University Kandilli Observatory and

Earthquake Research Institute (KOERİ). Location of selected events and and relevant stations are given in Figure 4.1.

*Table 4.1. Information about six events used for moment tensor inversion solutions Data is from USGS/SLU Moment Tensor Solution Institute.*

| Event Date | Hour | Latitude | Longitude | Magnitude |
|------------|----------|----------|-----------|-----------|
| 2011/04/03 | 23:42:18 | 36.4938 | 28.7715 | 4.0 |
| 2018/09/12 | 18:13:26 | 36.4453 | 28.7325 | 4.2 |
| 2012/06/25 | 13:05:28 | 36.4422 | 28.9422 | 5.0 |
| 2019/02/11 | 16:38:03 | 36.5225 | 28.8355 | 4.0 |
| 2018/10/24 | 02:36:13 | 36.4774 | 28.7423 | 4.1 |
| 2019/04/15 | 17:42:25 | 36.4777 | 28.7332 | 5.0 |
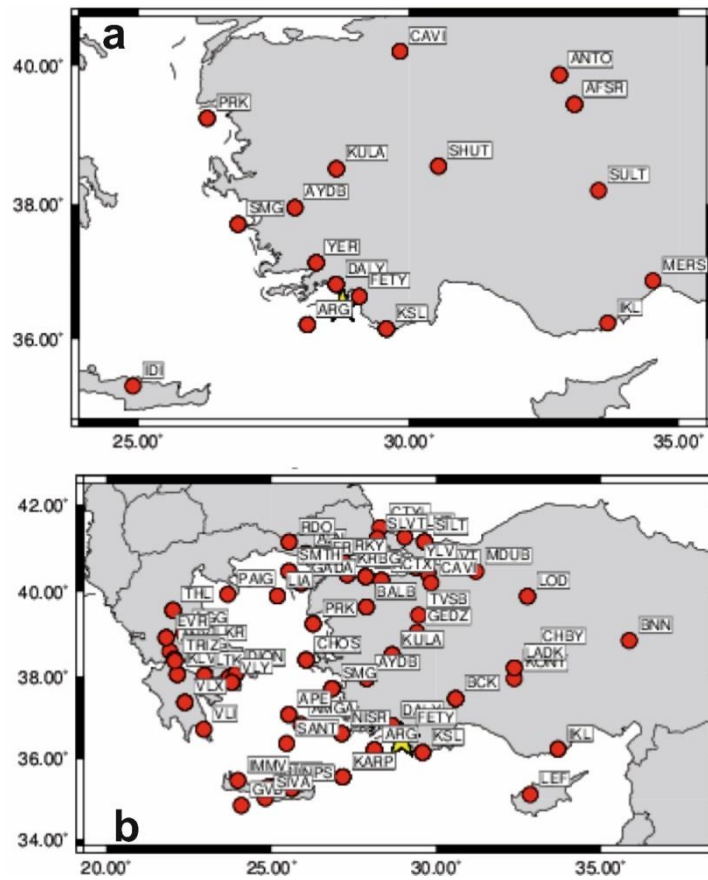
*Figure 4.1. Location and name of seismic stations that are used in moment tensor inversion method solution for sampled events in the study area. Recording seismic station locations for (a) 2011/04/03 (23:42:18) dated event; (b) 2012/06/25 (13:05:28) dated event. Figures are produced by using Hermann (2015) software.*

## 4.3. Apllied Bandpass Filter to Event Waveforms

Observed and predicted traces must be filtered by GSAC programme with band-pass filter command. These commands are used for noise filtering of traces. Filtered data gives more dependable solution for a given event. Event date and type of band-pass filters are given in Table 4.2.

*Table 4.2. Filter pass limitations applied on event waveform (HP: High pass filter LP: Low pass filter).*

| Event date | HP | LP | Event Date | HP | LP |
|---|---|---|---|---|---|
| 2018/09/12 | 0.04 | 0.06 | 2011/04/03 | 0.05 | 0.07 |
| 2012/06/25 | 0.04 | 0.06 | 2019/02/11 | 0.08 | 0.10 |
| 2018/10/24 | 0.07 | 0.09 | 2019/04/15 | 0.04 | 0.06 |

## 4.4. Calculation of Depth and Focal Mechanism Solution of Events

Wvfgrd86 is a module running on the main software; it is used for good traces monitored at short distance to calculate focal mechanism, depth and seismic moment of a given event. In order to find best solution, this software requires high quality signals and well-determined velocity model for Green's functions. These modules are used to determine best fit solution that represent focal mechanism, depth and seismic moment of given events (Figure 4.2).

Wvfgrd86 module is also used to prepare a figure that illustrates: (i) depth of event vs fitting ratio and (ii) focal mechanism solution at any depth vs the fit. Figure 4.3 illustrates depth sensivity for waveform mechanism.

| | DEPTH | STK | DIP | RAKE | MW | FIT |
|---|---|---|---|---|---|---|
| WVFGRD96 | 0.5 | 25 | 45 | 95 | 3.65 | 0.4254 |
| WVFGRD96 | 1.0 | 0 | 80 | 15 | 3.63 | 0.3950 |
| WVFGRD96 | 2.0 | 180 | 65 | 20 | 3.78 | 0.5439 |
| WVFGRD96 | 3.0 | 175 | 65 | 5 | 3.82 | 0.5750 |
| WVFGRD96 | 4.0 | 5 | 75 | 50 | 3.89 | 0.5930 |
| WVFGRD96 | 5.0 | 20 | 65 | 75 | 3.95 | 0.6408 |
| WVFGRD96 | 6.0 | 25 | 60 | 80 | 3.97 | 0.6765 |
| WVFGRD96 | 7.0 | 210 | 35 | 85 | 3.99 | 0.6875 |
| WVFGRD96 | 8.0 | 30 | 55 | 85 | 4.03 | 0.7131 |
| WVFGRD96 | 9.0 | 190 | 35 | 70 | 4.01 | 0.6994 |
| WVFGRD96 | 10.0 | 185 | 40 | 65 | 4.00 | 0.6898 |
| WVFGRD96 | 11.0 | 170 | 60 | -10 | 3.96 | 0.6780 |
| WVFGRD96 | 12.0 | 170 | 65 | -5 | 3.96 | 0.6772 |
| WVFGRD96 | 13.0 | 170 | 65 | -5 | 3.97 | 0.6764 |
| WVFGRD96 | 14.0 | 170 | 65 | -5 | 3.98 | 0.6739 |
| WVFGRD96 | 15.0 | 170 | 65 | -5 | 3.98 | 0.6695 |
| WVFGRD96 | 16.0 | 170 | 70 | -5 | 3.99 | 0.6642 |
| WVFGRD96 | 17.0 | 170 | 70 | -5 | 4.00 | 0.6599 |
| WVFGRD96 | 18.0 | 170 | 70 | -10 | 4.00 | 0.6549 |
| WVFGRD96 | 19.0 | 170 | 70 | -10 | 4.01 | 0.6502 |
| WVFGRD96 | 20.0 | 170 | 70 | -10 | 4.02 | 0.6443 |
| WVFGRD96 | 21.0 | 165 | 65 | -15 | 4.02 | 0.6370 |
| WVFGRD96 | 22.0 | 165 | 65 | -15 | 4.03 | 0.6310 |
| WVFGRD96 | 23.0 | 165 | 65 | -15 | 4.04 | 0.6233 |
| WVFGRD96 | 24.0 | 165 | 65 | -20 | 4.04 | 0.6161 |
| WVFGRD96 | 25.0 | 165 | 65 | -20 | 4.05 | 0.6085 |
| WVFGRD96 | 26.0 | 165 | 70 | -20 | 4.06 | 0.6006 |
| WVFGRD96 | 27.0 | 165 | 70 | -20 | 4.06 | 0.5932 |
| WVFGRD96 | 28.0 | 165 | 70 | -20 | 4.07 | 0.5846 |
| WVFGRD96 | 29.0 | 165 | 70 | -25 | 4.07 | 0.5773 |

The best solution is **a**

| | DEPTH | STK | DIP | RAKE | MW | FIT |
|---|---|---|---|---|---|---|
| WVFGRD96 | 8.0 | 30 | 55 | 85 | 4.03 | 0.7131 |

| | DEPTH | STK | DIP | RAKE | MW | FIT |
|---|---|---|---|---|---|---|
| WVFGRD96 | 0.5 | 335 | 60 | 25 | 3.81 | 0.3866 |
| WVFGRD96 | 1.0 | 330 | 85 | 0 | 3.80 | 0.4163 |
| WVFGRD96 | 2.0 | 335 | 80 | -15 | 3.91 | 0.5429 |
| WVFGRD96 | 3.0 | 155 | 85 | 35 | 3.99 | 0.5936 |
| WVFGRD96 | 4.0 | 160 | 80 | 40 | 4.03 | 0.6343 |
| WVFGRD96 | 5.0 | 160 | 75 | 40 | 4.05 | 0.6579 |
| WVFGRD96 | 6.0 | 160 | 75 | 35 | 4.05 | 0.6684 |
| WVFGRD96 | 7.0 | 160 | 75 | 30 | 4.05 | 0.6714 |
| WVFGRD96 | 8.0 | 160 | 75 | 35 | 4.09 | 0.6740 |
| WVFGRD96 | 9.0 | 160 | 75 | 30 | 4.09 | 0.6714 |
| WVFGRD96 | 10.0 | 160 | 75 | 25 | 4.09 | 0.6651 |
| WVFGRD96 | 11.0 | 160 | 80 | 25 | 4.09 | 0.6586 |
| WVFGRD96 | 12.0 | 160 | 80 | 25 | 4.10 | 0.6512 |
| WVFGRD96 | 13.0 | 160 | 80 | 20 | 4.10 | 0.6440 |
| WVFGRD96 | 14.0 | 160 | 80 | 20 | 4.11 | 0.6360 |
| WVFGRD96 | 15.0 | 160 | 80 | 20 | 4.12 | 0.6274 |
| WVFGRD96 | 16.0 | 160 | 80 | 20 | 4.12 | 0.6181 |
| WVFGRD96 | 17.0 | 155 | 75 | -20 | 4.13 | 0.6142 |
| WVFGRD96 | 18.0 | 155 | 75 | -20 | 4.13 | 0.6086 |
| WVFGRD96 | 19.0 | 155 | 75 | -20 | 4.14 | 0.6031 |
| WVFGRD96 | 20.0 | 155 | 75 | -20 | 4.15 | 0.5968 |
| WVFGRD96 | 21.0 | 155 | 75 | -20 | 4.16 | 0.5911 |
| WVFGRD96 | 22.0 | 155 | 75 | -20 | 4.16 | 0.5839 |
| WVFGRD96 | 23.0 | 155 | 80 | -20 | 4.17 | 0.5766 |
| WVFGRD96 | 24.0 | 155 | 80 | -20 | 4.17 | 0.5690 |
| WVFGRD96 | 25.0 | 155 | 80 | -15 | 4.18 | 0.5625 |
| WVFGRD96 | 26.0 | 155 | 80 | -15 | 4.18 | 0.5562 |
| WVFGRD96 | 27.0 | 160 | 85 | 15 | 4.20 | 0.5470 |
| WVFGRD96 | 28.0 | 155 | 80 | -10 | 4.20 | 0.5404 |
| WVFGRD96 | 29.0 | 160 | 90 | 15 | 4.21 | 0.5348 |

The best solution is **b**

| | DEPTH | STK | DIP | RAKE | MW | FIT |
|---|---|---|---|---|---|---|
| WVFGRD96 | 8.0 | 160 | 75 | 35 | 4.09 | 0.6740 |

*Figure 4.2. Wvfgrd86 module is used to obtain best solution for given events; it contains focal mechanism solution, depth and seismic moment (Mw) of the event. Best solutions for (a) 2011/04/03 (23:42:18) dated event; (b) 2012/06/25 (13:05:28) dated event. Figure is produced by using Hermann (2015) software.*

## 4.5. Accuracy Parameter of Moment Inversion Solutions

Comparison of observed and predicted waveforms is an important parameter for reliability of the moment inversion solutions (Figure 4.3). Observed (red traces) and predicted (blue traces) components are plotted using the same scale and peak amplitudes are indicated by numbers to the left of each trace (Figure 4.4). This comparison contains time shift required for maximum correlation between the observed and predicted traces and is written in numbers (Figure 4.4). Adding and extracting waveforms that represent good correlation between predicted and observed waveforms provide more reliable solutions. This method eventually leads to the best solution for given events (see section 2.1 for more information).

83

Three components of wave forms are Z (Vertical), R (Radial) and T (Transverse) (Figure 4.4). The correlation of observed and predicted waves rate is also indicated in percentage of variance reduction; higher value means better fit and supply more dependable solution for a given event.
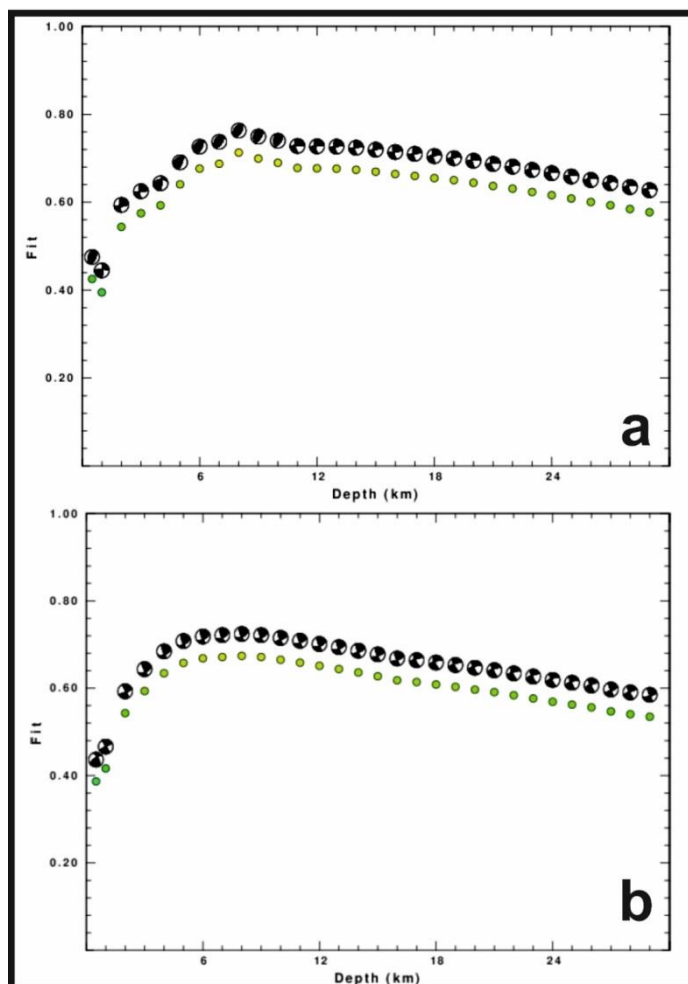


*Figure 4.3. Best fit ratio vs depth graph for moment tensor inversion solution of two events in the study area. (a) 2011.04.03 dated event and (b) 2018.09.12 dated event. Figures are produced by using Hermann (2015) software.*
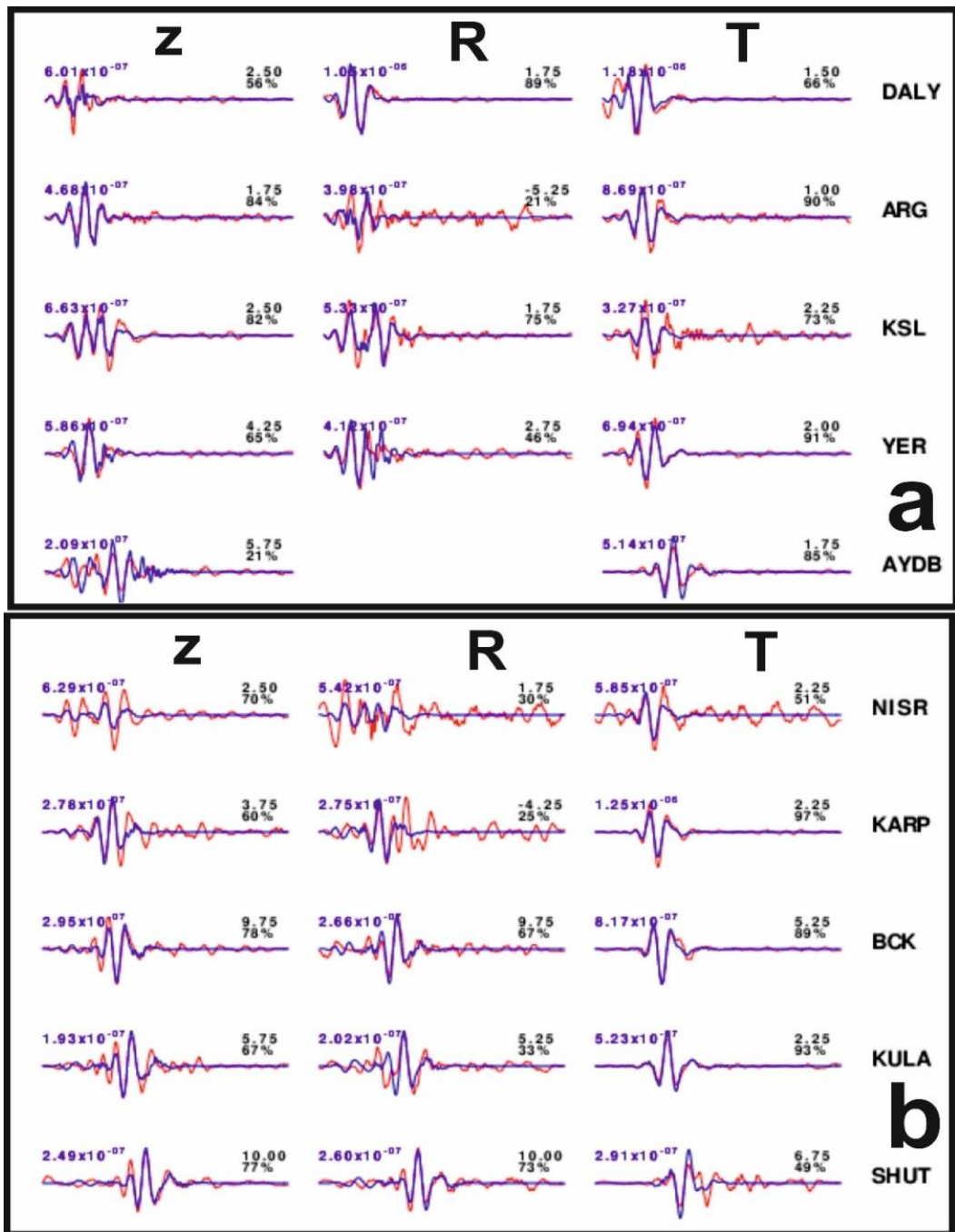
*Figure 4.4. The comparison of the observed and predicted waveforms of selected events in the study area. (a) 2011.04.03 dated event and (b) 2018.09.12 dated event. Red traces represent observed waveforms, blue, predicted waveforms. Figures are produced by using Hermann (2015) software.*

The time shift between observed and predicted waveforms indicate that synthetics are not computed strictly at the same distance because velocity model used in calculations

may not be perfect. Positive time shifts indicate that prediction trace is too fast for observed one whereas a negative value means a slow prediction (Figure 4.6). Time shifts between predicted and observed waveforms are used to estimate and calculate location errors. Time shift between waveforms may rise when: (i) origin time and epicentral distance are incorrect, (ii) velocity model used for the inversion is incorrect, (iii) velocity model used to define the P-arrival time is not the same as the velocity model used for the waveform inversion. By using a formula of mislocation, the time shifts can be fitted to a functional form (see section 2.1.1 for more information). Once derived shift in origin time and epicentral coordinates are calculated in the safe zone, reliable solutions may be generated (Figure 4.5).

Velocity models used for inversion cause of changes for a given event moment tensor inversion solution. In order to find most reliable moment tensor inversion solution, accuracy of the velocity model is important. Velocity model used in this thesis is given in Table 4.3. For a given depth inerval (H), VP (P wave velocity) , Vs (S wave velocity) and RHO (Density) are used in the velocity model.

## 4.6. Event Moment Tensor Inversion Solutions

Moment tensor inversion of solutions of six (6) main events are preformed; the results will be presented for each event. The method supplies dependable results about character of the related fault.

### 4.6.1. Mo, Mw, Z Values of Moment Tensor Inversion Solution Events

Moment tensor inversion solution of events that occured in our study area suppy significant data about the fault that cause the event. Magnitude, depth and moment of events are calculated by sofware (Table 4.4). Events are selected based on their magnitude, location and depth, in order to supply reasonable moment tensor inversion solutions.
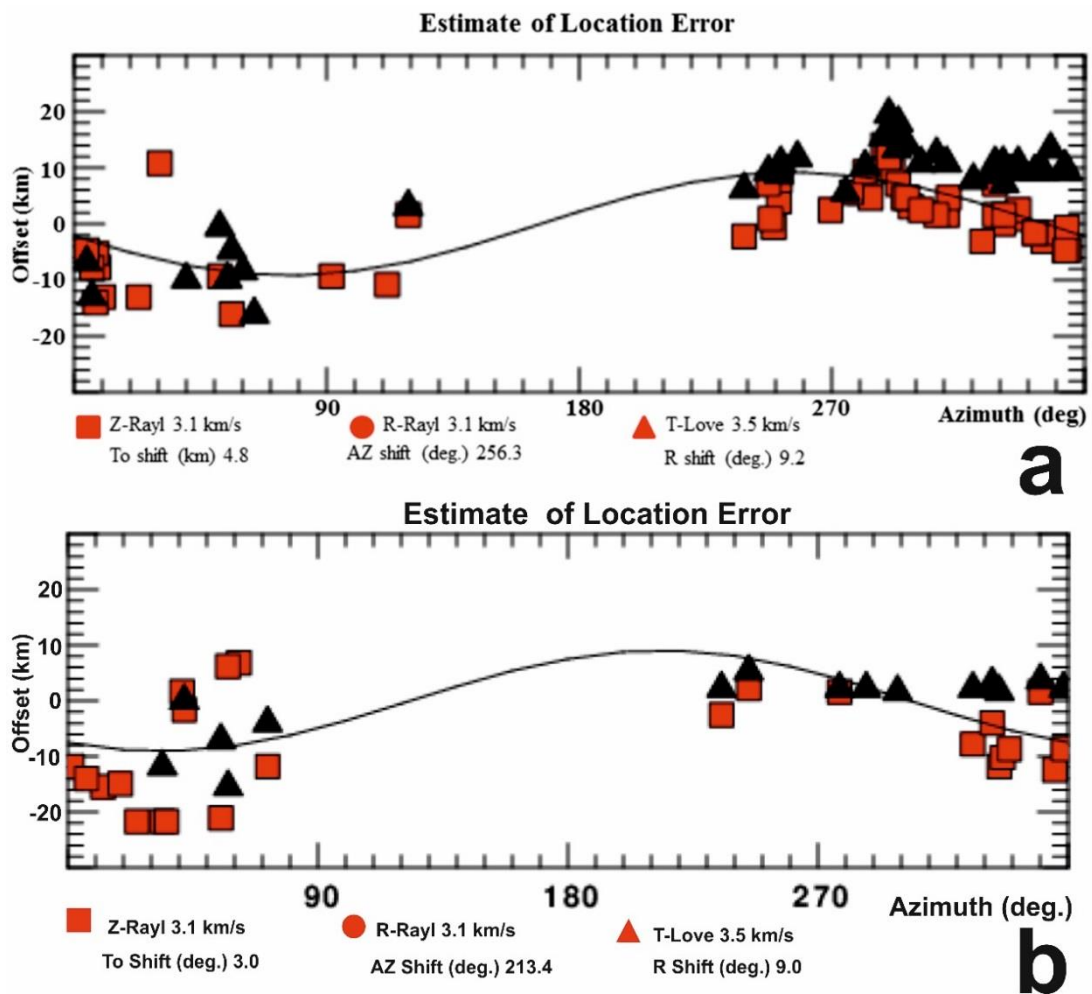
*Figure 4.5. Estimate of location error calculation for selected events in the study area. (a) 2018.09.12 dated event and (b) 2011.04.03 dated event. Figures are produced by using Hermann (2015) software.*

Size of an earthquake is indicated by number that is called magnitude. Magnitude measurements are calculated from the maximum movements recorded by seismograph. Several type of measurement method, like Ml local magnitude (*Richter Magnitude*), Ms (Surface-wave magnitude), body-wave magnitude (Mb) and Moment magnitude (Mw), are used for calculations. Another important parameter related with moment is Mo (seismic moment) and it is calculated from parameters, such as earthquake rupture surface, average fault displacement, shear modulus of the crustal volume containing the fault.

*Table 4.3. Table indicate velocity model parameters (Vp,Vs, RHO) for moment tensor inversion solution in study area.*

| H (km) | Vp (km/s) | Vs (km/s) | RHO(GM/CC) |
|--------|-----------|-----------|------------|
| 1,90   | 3,41      | 2,01      | 2,21       |
| 6,10   | 5,54      | 3,30      | 2,61       |
| 13,00  | 6,27      | 3,73      | 2,78       |
| 19,00  | 6,41      | 3,77      | 2,82       |
| 0,00   | 7,90      | 4,62      | 3,27       |

Events' solution indicates predominantly shallow earthquake epicenter in the study area. Seismic interpretation presented in Chapter 3 also corresponds to shallow depths up to 3 seconds from seabed. Correlation between epicenter of an earthquake and related fault interpreted from seismic section is possible. Medium-sized magntitude (Mo and Mw) earthquakes area selected (Table 4.4) for better focal mechanism solutions and to clarify better tectonic settlement.

*Table 4.4. Date, Mo (Seismic Moment), Mw (Moment Magnitude) and Z (Depth) values of six events used in moment tensor inversion solution.*

| Event Date | Mo (Seismic Moment) | Mw (Moment Magnitude) | Z (Depth) |
|------------|---------------------|-----------------------|-----------|
| 2018/09/12 | 1.72e+22 dyne-cm    | 4.09                  | 8 km      |
| 2011/04/03 | 1.40e+22 dyne-cm    | 4.03                  | 8 km      |
| 2012/06/25 | 2.54e+23 dyne-cm    | 4.87                  | 32 km     |
| 2019/02/11 | 1.06e+22 dyne-cm    | 3.95                  | 16 km     |
| 2018/10/24 | 1.06e+22 dyne-cm    | 3.95                  | 10 km     |
| 2019/04/15 | 1.22e+22 dyne-cm    | 3.99                  | 10 km     |

## 4.6.2. Nodal Planes, Dip and Strike Values From Moment Tensor Inversion Solution Events

Moment tensor inversion method solution of events supply two possible seismic nodal planes that are responsible for each event. One of them is paralel to main fault that cause the event, while the other is called auxiliary plane. In order to decide which of these nodal planes are responsible for a given event, geometry (strike and dip direction) of the faults need to be known. In this study, the information about the main faults is obtained by structural interpretation of seismic sections (see Chapter 3 for more information). Strikes of the faults varies between N745°E to N32°E. Dip directions are also variable; depending on the strike of the fault as towards South, North, Southeast and Northwest. Nodal planes for each event are presented in Table 4.5.

*Table 4.5. Strike, dip, rake of selected events in study area. Blue raws indicate principal plane axes responsible from a given event. The fault data is based on seismic interpretation presented in Chapter 3.*

| Event Date | Plane | Strike (°N) | Dip (°) | Rake (°) |
|---|---|---|---|---|
| 12.09.2018 | Nodal Plane 1 | 160 | 75 | 35 |
|  | Nodal Plane 2 | 60 | 56 | 162 |
| 03.04.2011 | Nodal Plane 1 | 30 | 55 | 85 |
|  | Nodal Plane 2 | 219 | 35 | 97 |
| 25.06.2012 | Nodal Plane 1 | 225 | 70 | -30 |
|  | Nodal Plane 2 | 326 | 62 | -157 |
| 11.02.2019 | Nodal Plane 1 | 125 | 70 | -45 |
|  | Nodal Plane 2 | 234 | 48 | -153 |
| 24.10.2018 | Nodal Plane 1 | 239 | 60 | -145 |
|  | Nodal Plane 2 | 130 | 60 | -35 |
| 15.04.2019 | Nodal Plane 1 | 230 | 81 | -150 |
|  | Nodal Plane 2 | 135 | 60 | -10 |

### 4.6.3. 2018/09/12 Dated Event Moment Tensor Inversion Solution

Moment tensor inversion solution of 2018/10/24 (18.13.26) (GMT) dated event provides two seismic nodal planes (Figure 4.6; Table 4.5). Comparison with the information from the seismic interpretation indicates that principal plane strikes in 060°N and dips at 56° towards SE; the rake angle is 162°. The solution of this event therefore is consistent with a right-lateral strike-slip fault with relatively minor reverse component. Plunges and azimuths P and T axes are 12°/286°N and 35°/025°N, respectively. Direction of pressure axis that creates this fault strike should be in NE–SW direction (Figure 4.6). The moment magnitude (Mw) of this event is 4.09 and the depth is 8 km; one of the shallowest event presented in the thesis (Table 4.4).



**Moment Tensor Inversion Method Solution of 2018/09/12 Dated Event**

| Event Date | Mo (Seismic Moment) | Mw (Moment Magnitude) | Z (Depth) |
|---|---|---|---|
| 2018/09/12 | 1.72e+22 dyne-cm | 4.09 | 8 km |

**a**

| Axis | Azimuth (°) | Plunge (°) |
|---|---|---|
| P-axes | 286 | 12 |
| T-axes | 25 | 35 |

**b**

| Event Date | Plane | Strike (N) | Dip (deg°) | Rake (deg°) |
|---|---|---|---|---|
| 12.09.2018 | Nodal Plane 1 | 160 | 75 | 35 |
| | Nodal Plane 2 | 60 | 56 | 162 |

**c**

**d**
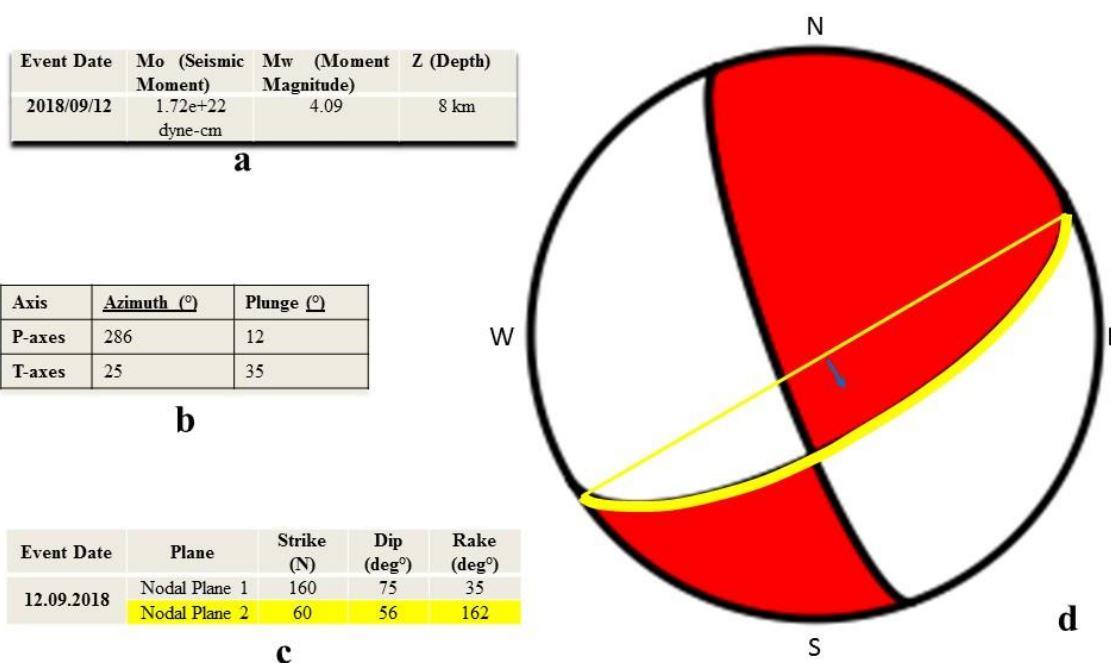
*Figure 4.6. Moment tensor inversion solution of 2018/09/12 dated event. (a) Mo, Mw, Z values for the event; (b) Azimuth and plunge of P- and T-axes; (c) strike, dip and rake of two seismic nodal planes, yellow raw marks the principal plane for the event; (d) focal mechanism solution of the event; yellow plane represents the principal plane that caused the event. Blue arrow shows the dip direction of the fault.*

90

### 4.6.4. 2012/06/25 Dated Event Moment Tensor Inversion Solution

Moment tensor inversion solution of 2012/06/25 (13.05.28) (GMT) dated event provides two seismic nodal planes (Figure 4.7; Table 4.5). Comparison with the information from the seismic interpretation indicates that principal plane strikes in 225°N and dips at 70° towards NW; the rake angle is –30°. The solution of this event therefore is consistent with a left-lateral strike-slip fault with relatively minor normal component. Plunges and azimuths P and T axes are 35°/183°N and 05°/277°N, respectively. Direction of pressure axis that creates this fault strike should be in NE–SW direction (Figure 4.7). The moment magnitude (Mw) of this event is 4.87 that correspond to a moderate earthquake. The depth of the event is 32 km; deepest event presented in the thesis (Table 4.4).

**Moment Tensor Inversion Method Solution of 2012/06/25 Dated Event**

| Event Date | Mo (Seismic Moment) | Mw (Moment Magnitude) | Z (Depth) |
|---|---|---|---|
| 2012/06/25 | 2.54e+23 dyne-cm | 4.87 | 32 km |

**a**

| Axis | Azimuth (°) | Plunge (°) |
|---|---|---|
| P-axes | 183 | 35 |
| T-axes | 277 | 5 |

**b**

| Event Date | Plane | Strike (N) | Dip (deg°) | Rake (deg°) |
|---|---|---|---|---|
| 2012/06/25 | Nodal Plane 1 | 225 | 70 | -30 |
| | Nodal Plane 2 | 326 | 62 | -157 |

**c**



**d**
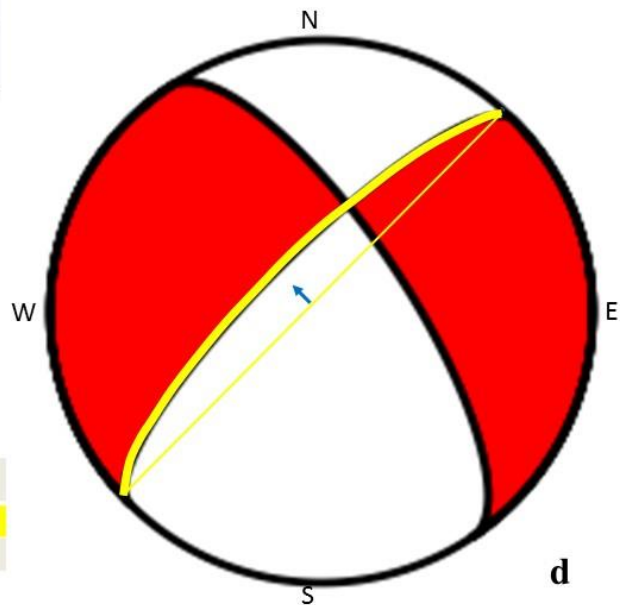
*Figure 4.7. Moment tensor inversion solution of 2012/06/25 dated event. (a) Mo, Mw, Z values for the event; (b) Azimuth and plunge of P- and T-axes; (c) strike, dip and rake of two seismic nodal planes, yellow raw marks the principal plane for the event; (d) focal mechanism solution of the event; yellow plane represents the principal plane that caused the event. Blue arrow shows the dip direction of the fault.*

91

## 4.6.5. 2019/02/11 Dated Event Moment Tensor Inversion Solution

Moment tensor inversion solution of 2019/02/11 (16.38.03) (GMT) dated event provides two seismic nodal planes (Figure 4.8; Table 4.5). Comparison with the information from the seismic interpretation indicates that principal plane strikes in 234°N and dips at 48° towards NW; the rake angle is −153°. The solution of this event therefore is consistent with a right-lateral strike-slip fault with relatively minor normal component. Plunges and azimuths P and T axes are 45°/0803°N and 13°/184°N, respectively. Direction of pressure axis that creates this fault strike should be in NE–SW direction (Figure 4.8). The moment magnitude (Mw) of this event is 3.95 that correspond to a moderate earthquake. The depth of the event is 16 km (Table 4.4).

**Moment Tensor Inversion Method Solution 2019/02/11 Dated Event**

| Event Date | Mo (Seismic Moment) | Mw (Moment Magnitude) | Z (Depth) |
|---|---|---|---|
| 2019/02/11 | 1.06e+22 dyne-cm | 3.95 | 16 km |

**a**

| Axis | Azimuth (°) | Plunge (°) |
|---|---|---|
| P-axes | 80 | 45 |
| T-axes | 184 | 13 |

**b**

| Event Date | Plane | Strike (N) | Dip (deg°) | Rake (deg°) |
|---|---|---|---|---|
| 2012/06/25 | Nodal Plane 1 | 125 | 70 | -45 |
| | Nodal Plane 2 | 234 | 48 | -153 |

**c**



**d**
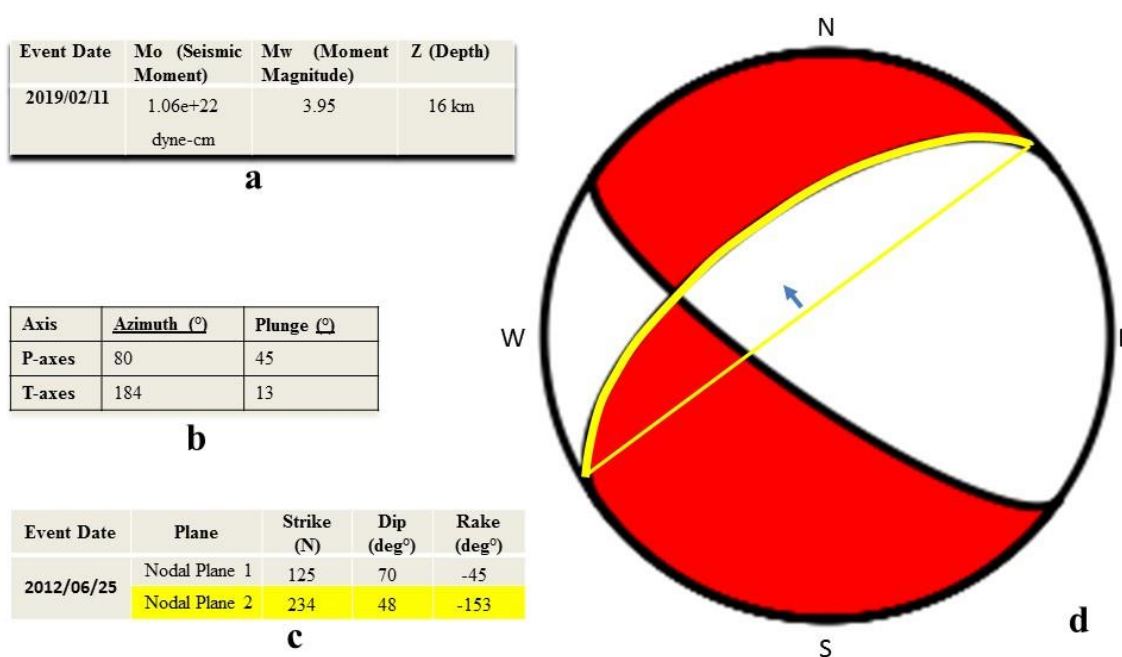
*Figure 4.8. Moment tensor inversion solution of 2019/02/11 dated event. (a) Mo, Mw, Z values for the event; (b) Azimuth and plunge of P- and T-axes; (c) strike, dip and rake of two seismic nodal planes, yellow raw marks the principal plane for the event; (d) focal mechanism solution of the event; yellow plane represents the principal plane that caused the event. Blue arrow shows the dip direction of the fault.*

### 4.6.6. 2019/04/15 Dated Event Moment Tensor Inversion Solution

Moment tensor inversion solution of 2019/04/15 (17.42.25) (GMT) dated event provides two seismic nodal planes (Figure 4.9; Table 4.5). Comparison with the information from the seismic interpretation indicates that principal plane strikes in 230°N and dips at 81° towards NW; the rake angle is −150°. The solution of this event therefore is consistent with a right-lateral strike-slip fault with relatively minor normal component. Plunges and azimuths P and T axes are 27°/097°N and 14°/359°N, respectively. Direction of pressure axis that creates this fault strike should be in NE–SW direction (Figure 4.9). The moment magnitude (Mw) of this event is 3.99 that correspond to a moderate earthquake. The depth of the event is 10 km (Table 4.4).

**Moment Tensor Inversion Method Solution 2019/04/15 Dated Event**

| Event Date | Mo (Seismic Moment) | Mw (Moment Magnitude) | Z (Depth) |
|---|---|---|---|
| 2019/04/15 | 1.22e+22 dyne-cm | 3.99 | 10 km |

**a**

| Axis | Azimuth (°) | Plunge (°) |
|---|---|---|
| P-axes | 97 | 27 |
| T-axes | 359 | 14 |

**b**

| Event Date | Plane | Strike (N) | Dip (deg°) | Rake (deg°) |
|---|---|---|---|---|
| 2019/04/15 | Nodal Plane 1 | 230 | 81 | -150 |
| | Nodal Plane 2 | 135 | 60 | -10 |

**c**



**d**
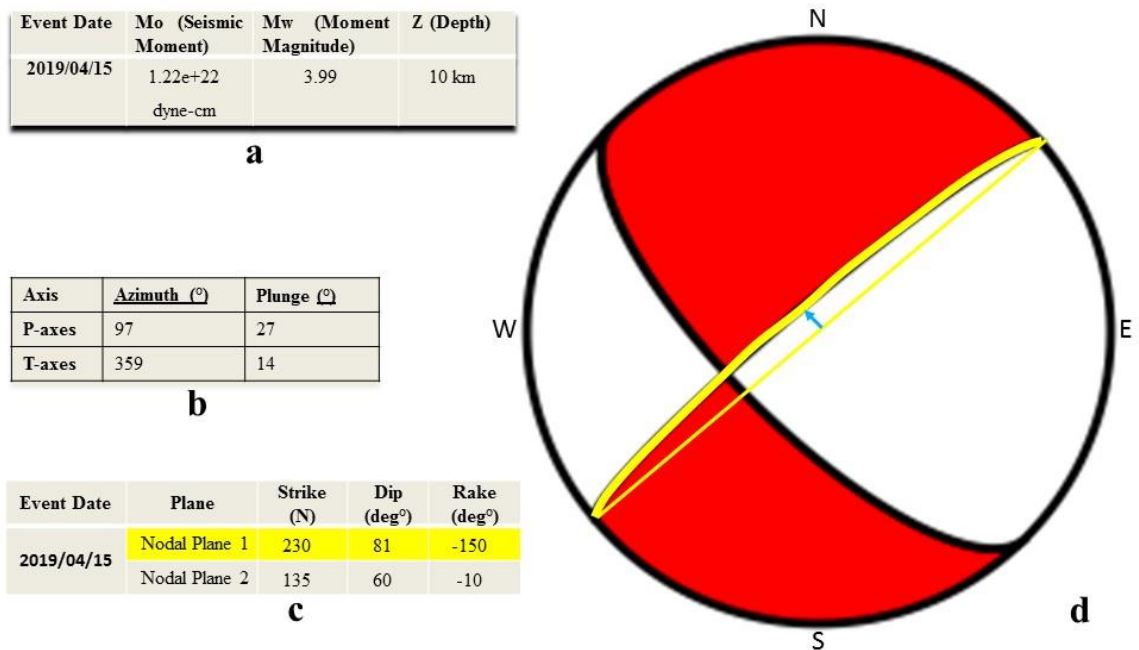
*Figure 4.9. Moment tensor inversion solution of 2019/04/15 dated event. (a) Mo, Mw, Z values for the event; (b) Azimuth and plunge of P- and T-axes; (c) strike, dip and rake of two seismic nodal planes, yellow raw marks the principal plane for the event; (d) focal mechanism solution of the event; yellow plane represents the principal plane that caused the event. Blue arrow shows the dip direction of the fault.*

### 4.6.7. 2018/10/24 Dated Event Moment Tensor Inversion Solution

Moment tensor inversion solution of 2018/10/24 (02.36.13) (GMT) dated event provides two seismic nodal planes (Figure 4.10; Table 4.5). Comparison with the information from the seismic interpretation indicates that principal plane strikes in 239°N and dips at 60° towards NW; the rake angle is −145°. The solution of this event therefore is consistent with a right-lateral strike-slip fault with normal component. Plunges and azimuths P and T axes are 45°/095°N and 00°/005°N, respectively. Direction of pressure axis that creates this transtensional fault strike should be in NE–SW direction (Figure 4.10). The moment magnitude (Mw) of this event is 3.95 that correspond to a moderate earthquake. The depth of the event is 10 km (Table 4.4).



**Moment Tensor Inversion Method Solution 2018/10/24 Dated Event**

| Event Date | Mo (Seismic Moment) | Mw (Moment Magnitude) | Z (Depth) |
|---|---|---|---|
| 2018/10/24 | 1.06e+22 dyne-cm | 3.95 | 10 km |

**a**

| Axis | Azimuth (°) | Plunge (°) |
|---|---|---|
| P-axes | 95 | 45 |
| T-axes | 5 | 0 |

**b**

| Event Date | Plane | Strike (N) | Dip (deg°) | Rake (deg°) |
|---|---|---|---|---|
| 2012/06/25 | Nodal Plane 1 | 239 | 60 | -145 |
| | Nodal Plane 2 | 130 | 60 | -35 |

**c**

**d**
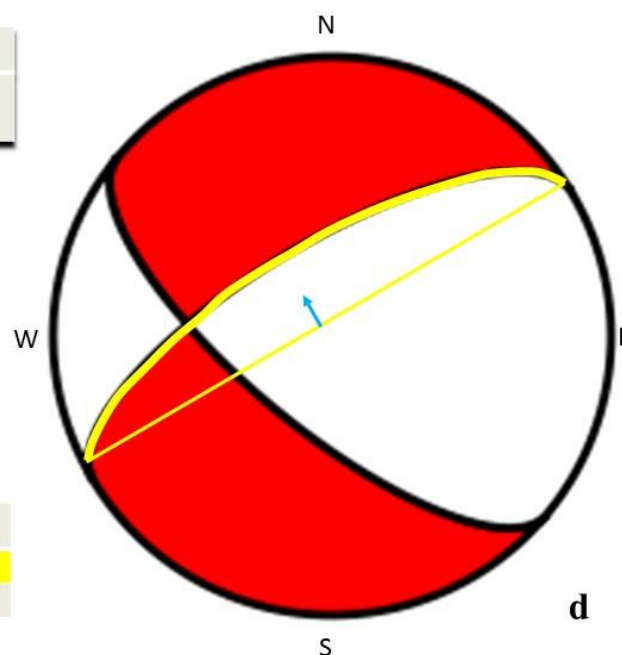
*Figure 4.10. Moment tensor inversion solution of 2018/10/24 dated event. (a) Mo, Mw, Z values for the event; (b) Azimuth and plunge of P- and T-axes; (c) strike, dip and rake of two seismic nodal planes, yellow raw marks the principal plane for the event; (d) focal mechanism solution of the event; yellow plane represents the principal plane that caused the event. Blue arrow shows the dip direction of the fault.*

### 4.6.8. 2011/04/03 Dated Event Moment Tensor Inversion Solution

Moment tensor inversion solution of 2011/04/03 (23.42.18) (GMT) dated event provides two seismic nodal planes (Figure 4.11; Table 4.5). Comparison with the information from the seismic interpretation indicates that principal plane strikes in 219°N and dips at 35° towards NW; the rake angle is 97°. The solution of this event therefore is consistent with a reverse fault with very minor right-lateral component. Plunges and azimuths P and T axes are 79°/281°N and 10°/124°N, respectively. Direction of pressure axis that creates this fault strike should be in NE−SW direction (Figure 4.11). The moment magnitude (Mw) of this event is 4.03 that correspond to a moderate earthquake. The depth of the event is 8 km; one of the shallowest event presented in the thesis (Table 4.4). There isnt any interpreted pure reverse fault near that event because of seismic data gap between Section B and C . Therefore two nodal planes whose strike almost paralel each other can be acceptable as a main solution.

Moment Tensor Inversion Method Solution of 2011/04/03 Dated Event

| Event Date | Mo (Seismic Moment) | Mw (Moment Magnitude) | Z (Depth) |
|---|---|---|---|
| 2011/04/03 | 1.40e+22 dyne-cm | 4.03 | 8 km |

a

| Axis | Azimuth (°) | Plunge (°) |
|---|---|---|
| P-axes | 281 | 79 |
| T-axes | 124 | 10 |

b

| Event Date | Plane | Strike (N) | Dip (deg°) | Rake (deg°) |
|---|---|---|---|---|
| 2011/04/03 | Nodal Plane 1 | 30 | 55 | 85 |
| | Nodal Plane 2 | 219 | 35 | 97 |

c

d
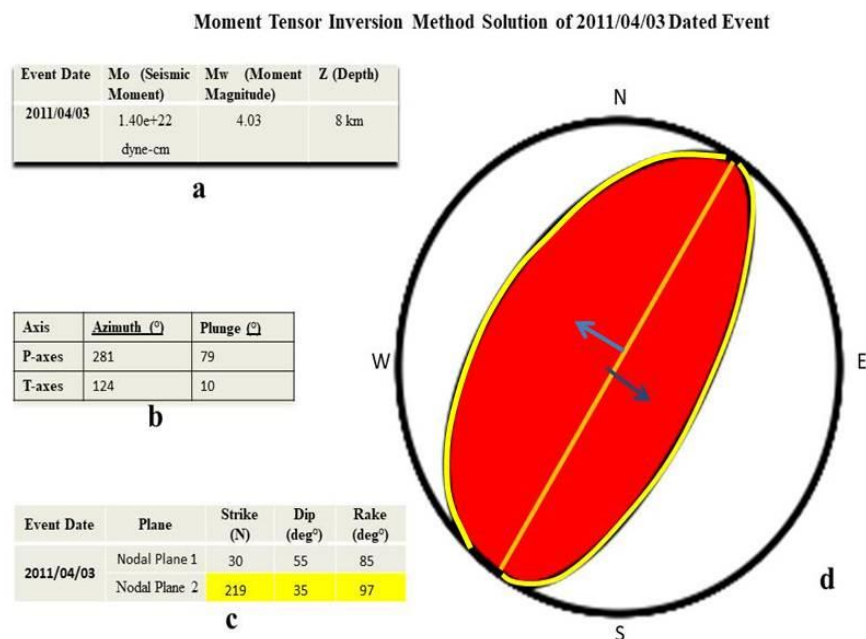
Figure 4.11. Moment tensor inversion solution of 2011/04/03 dated event. (a) Mo, Mw, Z values for the event; (b) Azimuth and plunge of P- and T-axes; (c) strike, dip and rake of two seismic nodal planes, yellow raw marks the principal plane for the event; (d) focal mechanism solution of the event; yellow and gray planes represents the principal plane that caused the event. Blue arrow shows the dip direction of the fault.

95

### 4.6.9. Location of Moment Tensor Inversion Solutions of All Events

The results of focal mecahanism solutions of six events and their beachballs are combined into one diagram and presented in Figure 4.12. The correlation of each event with the faults interpreted from seismic sections will be discussed in Discussion Chapter.
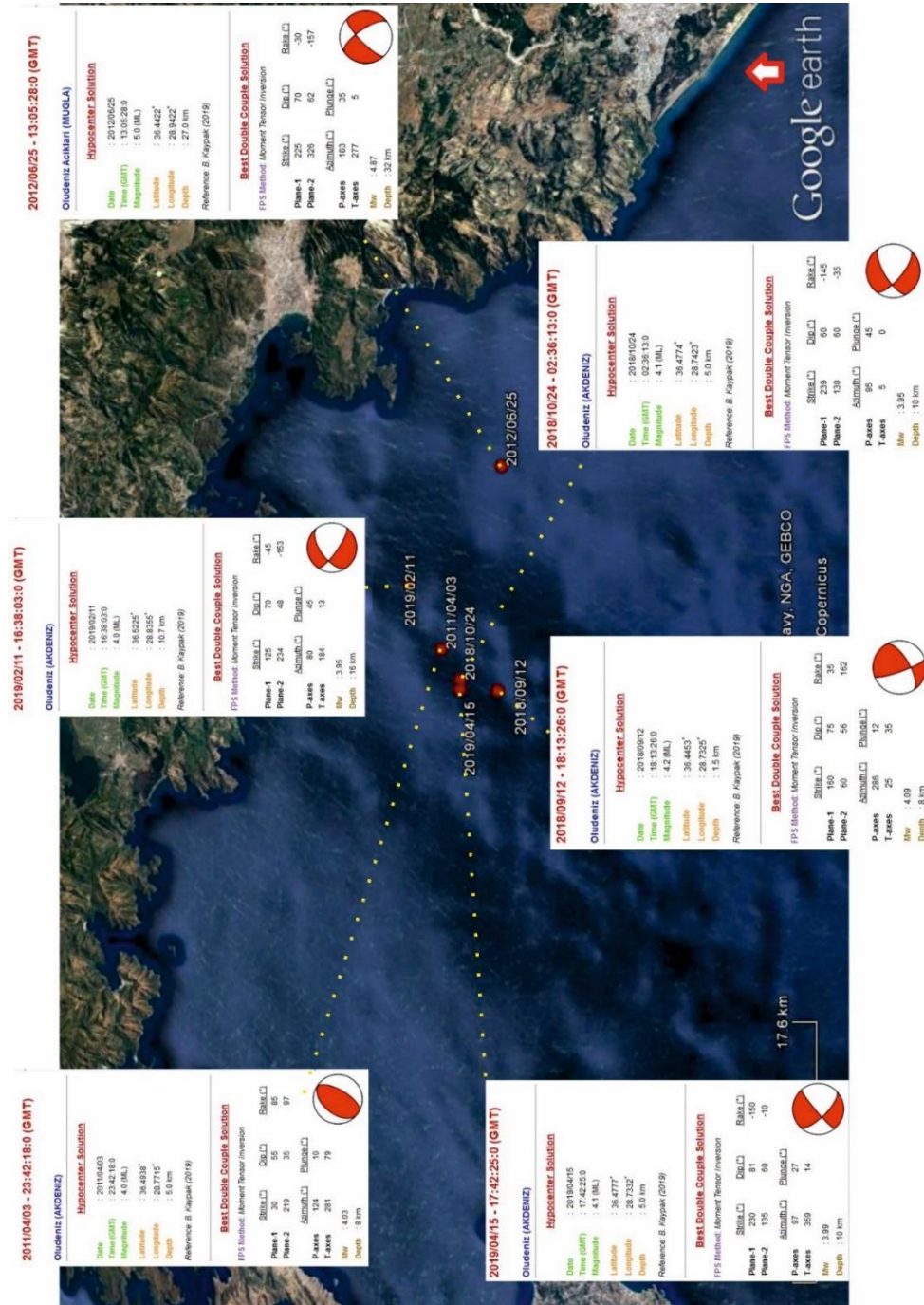
*Figure 4.12. Map view of moment tensor inversion solution of events, white rectangles indicate event values Strike, dip,Mw etc.*

# CHAPTER 5

# DISCUSSION AND CONCLUSION

The main objectives of the present thesis are interpret, identify and map major structural elements (faults) in a key area along Mediterranean coastline between Datça and Finike bays and define the basic characteristics of these structures. Two main methods have been applied in order to achieve these objectives: structural interpretation of seven seismic sections acquired by MTA Sismik-1 Research Vessel in 1996 and 1997 and moment tensor inversion solutions of six (selected) main events occurred in the area of interest.

This chapter is about the integration and interpretation of the main results obtained from the two methods (see Chapters 3 and 4 for details). Fault and event correlation will be performed, and basin evolution, be discussed. A comparison with the results of similar previous studies will also be made.

## 5.1. Fault and Event Correlation

Correlation between major (basin-bounding) faults and events would provide important insights into better understanding of structural styles and evolution in a given region; the geometry of faults (strike and dip direction) obtained from the seismic sections (Table 5.1) and orientation, dip direction and location of events presented in Figure 4.13 will form the base for this correlation.

Moment tensor inversion solution of a given event provides two possible seismic nodal planes (strike, dip and rake of possible fault planes) that are responsible for the event. The solution should be compatible with strike and dip direction of the structures identified in the seismic sections. Thus, one of those nodal planes will be eliminated to reach a compatible result.

99

Magnitude and depth of the earthquakes are taken into consideration when selecting the events; relatively shallow-to-moderate magnitude recent (after year 2005) earthquakes are chosen as they have most high quality reliable waveforms. The results of the movement tensor inversion method (the strike, dip and rake of the fault planes and the type of faulting; Table 5.2) are then compared and correlated to that of seismic interpretation (Table 5.3 and Figure 5.1).

*Table 5.1. Faults strike and dip direction inferred from seismic sections. Red colour in dip direction column means faults with almost vertical geometry or and changing dip direction. Blue refers faults with slight strike changes.*

| Fault Name | Orientation (Strike) | Dip Direction | Fault Name | Orientation (Strike) | Dip Direction |
|---|---|---|---|---|---|
| F-104 | N10°E | SE | F-114 | N70°E | SE |
| F-103 | N28°E | NW | F-115 | N69°E | NW |
| F-102 | N36°E | SE | F-116 | N65°E | SE |
| F-101 | N42°E | NW | F-117 | N64°E | NW |
| F-106 | N74°E | SE | F-122 | N37°E | NW |
| F-100 | N77°E | NW | F-121 | N32°E | SE |
| F-131 | N47°E | NW | F-108 | N72°E | NW |
| F-132 | N48°E | SE | F-123 | N70°E | SE |
| F-111 | N68°E | SE | F-124 | N65°E | NW |
| F-113 | N72°E | SE | F125 | N66°E | SE |
| F-112 | N70°E | NW | | | |

*Table 5.2. Type of faulting occurred in the study area.*

| Event Date | Type of Faulting |
|---|---|
| 2018-09-12 | Right-lateral strike-slip fault with reverse component |
| 2018-10-24 | Right-lateral strike-slip fault with normal component |
| 2019-04-15 | Right-lateral strike-slip fault with normal component |
| 2011-04-03 | Reverse fault |
| 2019-02-11 | Right-lateral strike-slip fault with normal component |
| 2012-06-25 | Left-lateral strike-slip fault with normal component |

Table 5.3. Correlation of faults interpreted from seismic sections and the moment tensor inversion solution. Blue rows indicate main fault data that caused the event (see Figure 5.1 for correlation).

| Event Date | Data from Moment Tensor Inversion Solution | | | | | | | | Data from Structural Seismic Interpretation | | |
|---|---|---|---|---|---|---|---|---|---|---|---|
| | Strike (°N) | Dip (°) | Rake (°) | Azimut (°N) | Plunge (°) | Axis (P, T) | Mg | Depth (km) | | Responsible Fault | |
| | | | | | | | | | | Orientation (Strike) | Dip Direction |
| 2018-09-12 | 160 | 75 | 35 | 286 | 12 | P | 4.09 | 8 | F-116 | N65°E | SE |
| | 60 | 56 SE | 162 | 25 | 35 | T | | | | | |
| | dextral fault with relatively minor reverse component | | | | | | | | | | |
| 2018-10-24 | 239 | 60 NW | -145 | 95 | 45 | P | 3.95 | 10 | F-117 | N64°E | NW |
| | 130 | 60 | -145 | 5 | 0 | T | | | | | |
| | dextral fault with normal component | | | | | | | | | | |
| 2019-04-15 | 230 | 81 NW | -150 | 97 | 27 | P | 3.99 | 10 | F-117 | N64°E | NW |
| | 135 | 60 | -150 | 359 | 14 | T | | | | | |
| | dextral fault with relatively minor normal component | | | | | | | | | | |
| 2011-04-03 | 30 | 55 | 85 | 124 | 10 | P | 4.03 | 8 | ? | ? | ? |
| | 219 | 35 NW | 97 | 281 | 79 | T | | | | | |
| | reverse fault with very minor dextral component | | | | | | | | | | |
| 2019-02-11 | 125 | 70 | -45 | 80 | 45 | P | 3.95 | 16 | F-115 | N72°E | NW |
| | 234 | 48 NW | -153 | 184 | 13 | T | | | | | |
| | dextral fault with relatively minor normal component | | | | | | | | | | |
| 2012-06-25 | 225 | 70 NW | -30 | 183 | 35 | P | 4.87 | 32 | F-122 | N37°E | NW |
| | 326 | 62 | -157 | 277 | 5 | T | | | | | |
| | sinistral fault with minor normal component | | | | | | | | | | |

102

The main conclusions derived from Table 5.3 and Figure 5.1 are summarized as follows:

**(1)** The source of the 2018-09-12 dated event, is interpreted as SE-dipping fault F-116 that bounds the basin B in seismic sections B and D. Fault F-116 is defined as a right-lateral strike-slip fault with reverse component. The fault displays changes in strike and dip direction; this geometry is attributed to strike-slip nature of the structure (Figure 5.1). The reverse component of the fault from the moment tensor solution appears not compatible with the normal faulting in the seismic interpretation.

**(2)** 2018-10-24 and 2019-04-15 dated events are interpreted to source from NW-dipping fault F-117; a stucture that forms at the central part of the basin B. It is defined as right-lateral strike-slip fault with a normal component (Table 5.2).

**(3)** 2019-02-11 dated event is caused by NW-dipping fault F-115; it occurs within the basin B and bounds an intrabasinal high/ridge-bounding structure in seismic sections A, B, and D. Fault F-115 is defined as a right-lateral strike-slip fault with normal component.

**(4)** NW-dipping fault F-122 is interpreted as the source structure for 2012-06-25 dated event. The fault also occurs in the basin B and bounds a intrabasinal high/ridge within the basin in seismic sections A and C (Figure 5.1). Fault F-122 is defined as a left-lateral strike-slip fault with normal component.

**(5)** Moment tensor solution of the 2011-04-03 dated event suggest reverse fault with very minor dextral component; it is not possible to correlate this event with any of the faults from the seismic interpretation. This may be a fault which is not possible to interpret in the seismic section.

**(6)** The difference in strike of fault from moment tensor solutions and seismic interpretations may arise from corrugated nature of the faults.
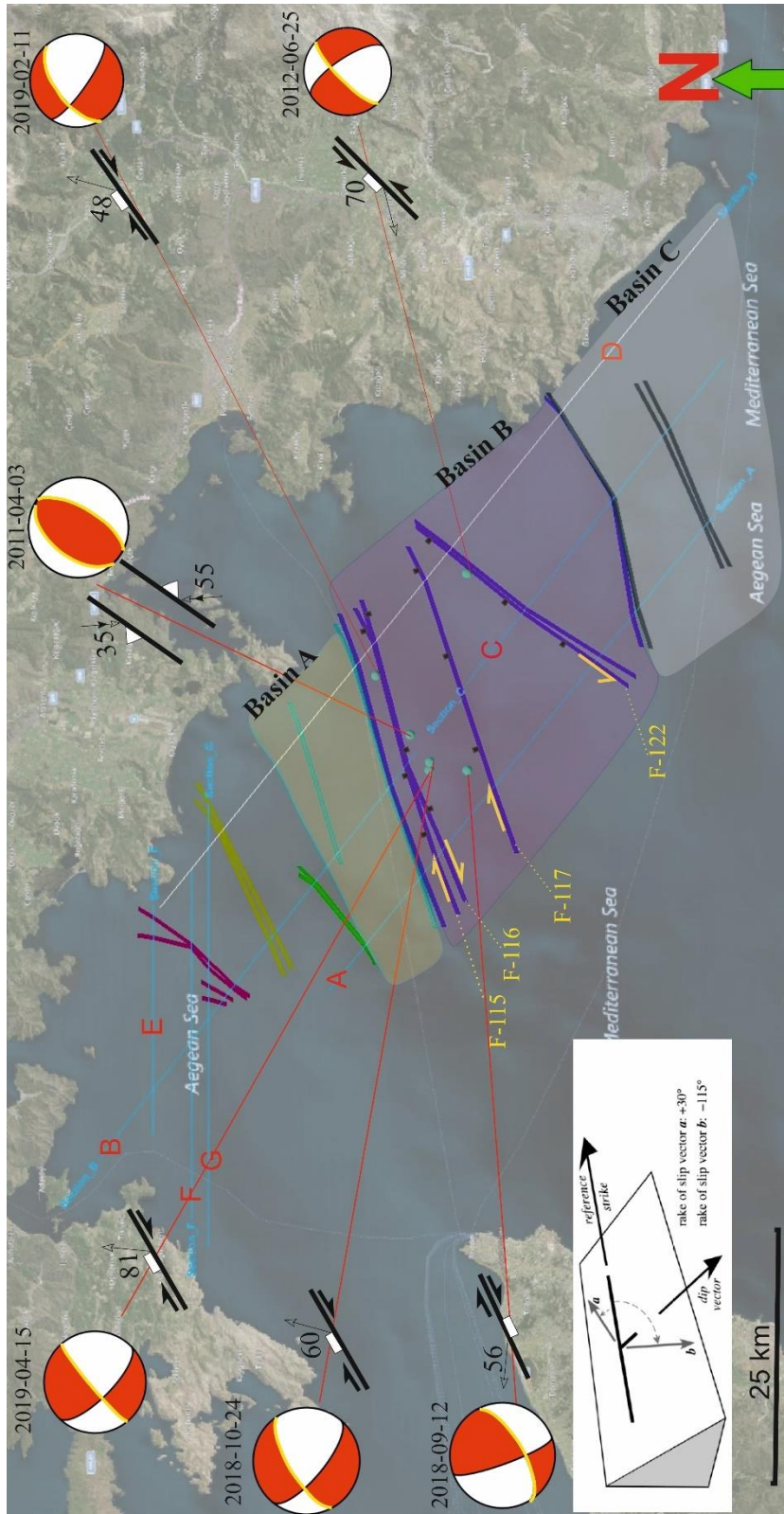
Figure 5.1. Correlation of major faults interpreted from seismic sections and beach balls from focal mechanism solutions produced from moment tensor inversion. Transparent yellow color area represents Basin A with light blue bounding faults; transparent red color area shows Basin B bounded by dark blue faults; and transparent white color area illustrates Basin C with gray colored bounding faults. Yellow arrows indicate slip motion on the faults. Black rectangle indicates dip directions of the faults.

104

It is important to emphasize that basin B is completely covered at seismic sections A and D, respectively at the west and east of the study area. Sections B and C are placed between A and D where basin B cannot be observable because approximately 8-km-long seismic data was not acquired by RV MTA Sismik-1 between sections B and C. Thus, the correlation of events occurred in the gap area with possible responsible fault is not possible.

To test the result of the present thesis and, to make a robust interpretation and correlation of faults and events, moment tensor inversion solutions of other events from the literature are studied (Table 5.4). The final fault-event correlation map is illustrated in Figure 5.2. The final solutions are broadly consistent with thesis study.

*Table 5.4. Moment tensor inversion solution of earthquakes occurred in the study area (from Irmak et al., 2015).Moment tensor inversion solutions from the thesis study are marked with (\*) and italic bold character.*

| No. | Date (dd/mm/yyyy) | Origin time (hr:mm:s) | Location (°) Lat.–Lon. | Depth (km) | Mag | Strike° | Dip° | Rake° | P° Az | P° Pl | T° Az | T° Pl |
|---|---|---|---|---|---|---|---|---|---|---|---|---|
| 1 | 10/06/2012 | 12:44:16 | 36.4528-28.9160 | 30 | 6.1ᵃ | 212 | 78 | 3 | 167 | 6 | 76 | 11 |
| 2 | 25/06/2012 | 13:05:30 | 36.4422-28.9422 | 49 | 5.0ᵇ | 211 | 57 | −57 | 175 | 62 | 278 | 7 |
| 3 | 10/06/2012 | 18:28:33 | 36.4622-28.9398 | 20 | 4.5ᵇ | 201 | 62 | −106 | 78 | 69 | 302 | 16 |
| 4 | 12/06/2012 | 21:58:12 | 36.4585-28.9157 | 30 | 4.4ᵇ | 261 | 35 | −33 | 252 | 53 | 131 | 21 |
| 5 | 11/06/2012 | 19:51:05 | 36.4315-28.9633 | 10 | 4.3ᵇ | 349 | 35 | −90 | 79 | 80 | 259 | 10 |
| 6 | 11/06/2012 | 02:06:35 | 36.3858-28.9552 | 10 | 4.3ᵇ | 229 | 80 | 4 | 184 | 4 | 93 | 10 |
| 7 | 11/06/2012 | 17:35:38 | 36.4022-28.9815 | 10 | 4.2ᵇ | 232 | 81 | 5 | 187 | 3 | 96 | 10 |
| 8 | 11/06/2012 | 14:00:18 | 36.4045-28.9762 | 20 | 3.9ᵇ | 328 | 42 | −104 | 134 | 80 | 247 | 4 |
| 9 | 10/06/2012 | 22:31:45 | 36.4343-28.9337 | 15 | 3.9ᵇ | 234 | 76 | 5 | 189 | 6 | 98 | 13 |
| 10 | 23/06/2012 | 04:26:06 | 36.4468-28.9178 | 23 | 3.7ᵇ | 344 | 42 | −93 | 110 | 86 | 256 | 3 |
| 11 | 10/06/2012 | 18:42:28 | 36.4385-28.9398 | 20 | 3.7ᵇ | 201 | 62 | −106 | 78 | 69 | 302 | 16 |
| 12 | 25/06/2012 | 14:33:30 | 36.4467-28.9350 | 23 | 3.5ᵇ | 234 | 76 | 5 | 189 | 6 | 98 | 13 |
| *13 | 2012/06/25 | 13:05:28 | 36,4422-28,9422 | 32 | 4.9 | 225 | 70 | -30 | 183 | 35 | 277 | 5 |
| *14 | 2019/02/11 | 16:38:03 | 36,5225-28,8355 | 16 | 3.9 | 234 | 48 | -153 | 184 | 13 | 80 | 45 |
| 15 | 04/08/2005 | 08:01:50 | 36.5587-28.7372 | 18 | 3.5ᶜ | 223 | 62 | −110 | 95 | 67 | 327 | 15 |
| *16 | 2011/04/03 | 23:42:18 | 36,4938-28,7715 | 8 | 4.0 | 219 | 35 | 97 | 124 | 10 | 281 | 79 |
| *17 | 2018/09/12 | 18:13:26 | 36,4453-28,7325 | 8 | 4.1 | 60 | 56 | 162 | 286 | 12 | 25 | 35 |
| 18 | 12/12/2009 | 15:23:16 | 36.5342-28.6402 | 57 | 4.7 | 198 | 46 | −90 | 108 | 89 | 288 | 1 |
| *19 | 2018/10/24 | 02:36:13 | 36,4774-28,7423 | 10 | 3.9 | 239 | 60 | -145 | 5 | 0 | 95 | 45 |
| 20 | 25/04/1957 | 02:25:36 | 36.4700-28.5600 | 53 | 7.1 | 328 | 73 | 71 | 73 | 26 | 212 | 58 |
| 21 | 14/06/2012 | 16:46:06 | 36.3907-29.0555 | 19.7 | 4.8 | 91 | 47 | 93 | 179 | 2 | 44 | 87 |
| 22 | 13/06/2012 | 08:59:06 | 36.4488-28.9263 | 23.8 | 4.4 | 125 | 48 | 121 | 14 | 1 | 107 | 67 |
| 23 | 10/06/2012 | 12:49:36 | 36.4707-28.9145 | 21.6 | 4.9 | 133 | 51 | 101 | 215 | 5 | 93 | 80 |
| *24 | 2019/04/15 | 17:42:25 | 36,4777-28,7332 | 10 | 4.0 | 230 | 81 | -150 | 359 | 14 | 97 | 27 |
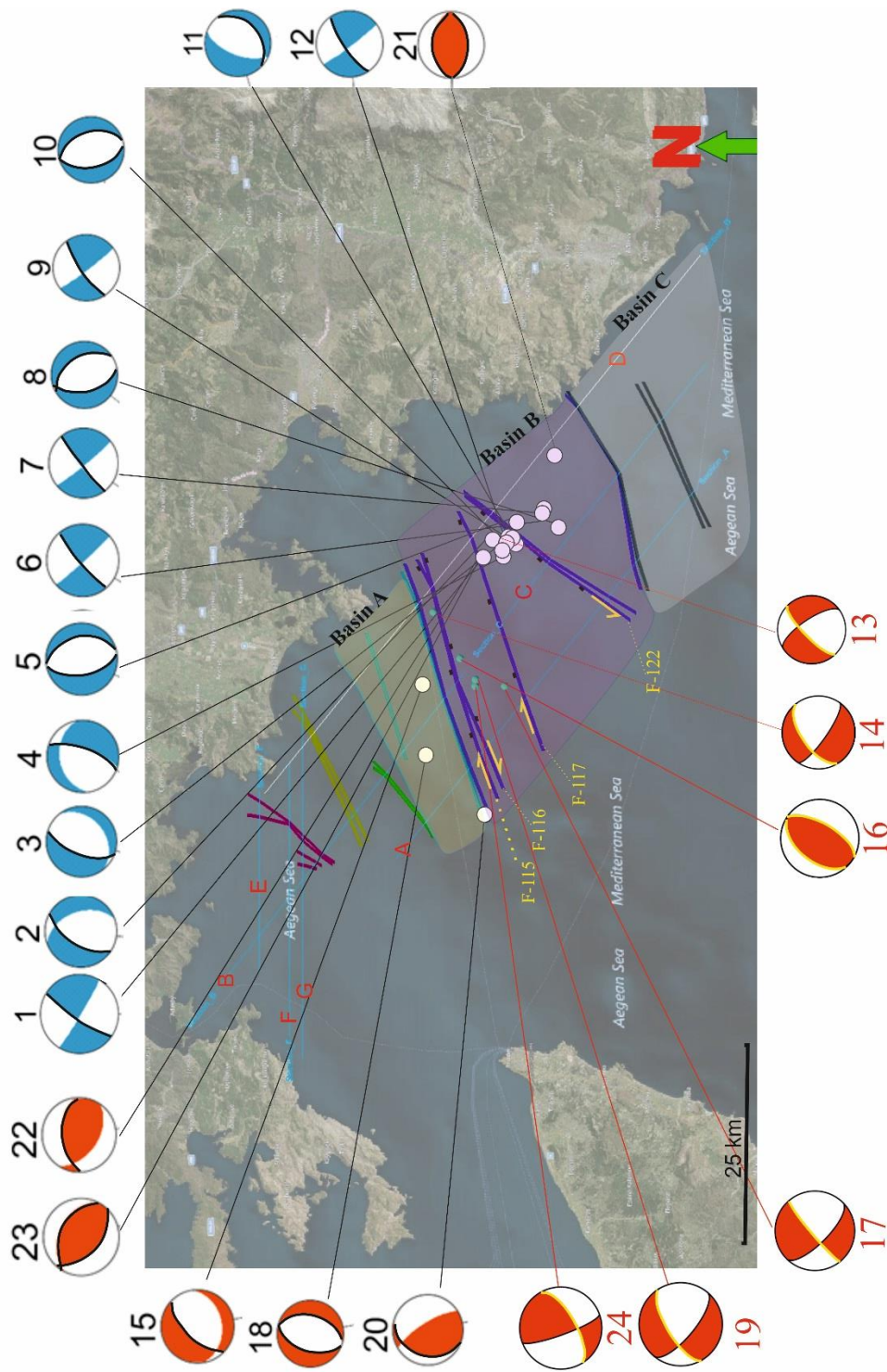
*Figure 5.2. Focal mechanism solution of the events occurred in the study area from Irmak et al (2015 and thesis study). Black lines with white balls show focal mechanism solutions from Irmak et al (2015). blue-white color focal mechanism solutions illustrates events M≤4, red-white color illustrates events M>4 events. Red lines with navy color balls indicate focal mechanism solutions from the thesis study. Yellow arrow indicates fault block movement direction. Black rectangle on the fault shows dip direction of the faults.*

Right-lateral strike-slip faulting is not only compatible with Fethiye-Burdur Fault Zone (FBFZ) and Pliny-Strabo STEP fault zone which are identified as a left-lateral strike-slip faults. The general orientation of the faults from the seismic interpretation is consistent with the fault segments in the FBFZ and STEP fault zone but not the sense of motion. The results of the present study therefore brings more confusion and makes the present case more complex. That is why, the accuracy of the moment tensor solutions are also checked; accuracy of the solutions is indicated by best fit value between green function and real seismic wave forms which is given in Table 5.5. These numbers change between 1.0 and 0.0 (minimum best fit value is 0,6680 and maximum best fit value is 0,7676) and indicate that reliability of the moment tensor inversion solutions of events is within accepted limits. Thus, it is concluded that the event solutions are rebost and that there are right-lateral faults in the study area.

Moment tensor inversion solution uses velocity model, which is supplied by the software. If more accurate velocity model(s) for the study area and its nearby regions is produced by future researchers, the results would be more accurate and reliable. Seismic stations used in thesis are mostly located in Anatolia. Data from stations in the Aegean Sea may supply more reliable solutions.

*Table 5.5. Table indicate events, responsible faults and best fit value that indicate reliability of the solution.*

| Event Date | Responsible Fault | Best Fit Value |
|---|---|---|
| 2018-09-12 | F-116 | 0,6740 |
| 2018-10-24 | F-117 | 0.6680 |
| 2019-04-15 | F-116 | 0.7413 |
| 2011-04-03 | F-116 | 0,7131 |
| 2019-02-11 | F-115 | 0.7378 |
| 2012-06-25 | F-122 | 0,7676 |

The nature of the faults in the study area casts more questions between the correlation of the FBFZ and STEP fault zone. That is why moment tensor inversion solutions of more events should be performed to obtain more reliable results. The results of present study therefore suggest that It may be wrong to correlate the FBFZ and the Pliny-Strabo STEP fault zone.

## 5.2. Basin Analysis

Interpretation of 2D seismic sections has revealed existence of three NE–SW trending basins in the area between Marmaris and Finike bays; basins A, B and C. Basin A occurs at the continental slope. There occur some irregularities along sea bottom morphology in all of these basins. They are interpreted as fault-bounded intrabasinal highs/ridges (Figure 5.3).

Formation time of ridges is a question waiting for clarification. Thickness of seismic units on top of the ridges and within the deepest floor of the basins can be used as a good indicator. As expected, the thickness is minimum at top of the ridges and maximum above the basin floor (Figure 5.3). This arises from accommodation space where it is limited above ridges.

Until the deposition of the *unit 3*, these ridges were formed under contractional tectonic regime. The deposition of the units 1, 2 and 3 has occurred under regional extensional regime, as suggested by the nature of bounding faults. Deposition continued as basins become deepened in the downthrown hanging-wall of the faults. Consequently, basins accommodated relatively thick basin-fill while deposition at top of the ridges is limited because of limited accommodation space. Focal mechanism solutions of the events that occurred in and around the study area on land mostly indicate almost pure normal faulting. Although F-116 interpreted as a fault with normal component in seismic sections that indicate a possibly transtensional or extensional tectonic regime, focal mechanism solutions of the events related with F-116 indicate dextral faulting with minor reverse component (Table 5.3, Figure 5.1). The reverse component is not compatible with the observed offset in the seismic

sections. Thickness of seismic horizon 1 changes between 5 – 7.5 ms. Total thickness of this horizon may reach up to 15 meters at the interpreted sesimic sections. Therefore, sea bottom should be deformed at least 10–15 meters in order to define recognizable recent deformation at seismic sections. The controversy between the focal mechanism solutions and the normal faulting interpreted from the seismic sections can therefore by explained by two different ways: (i) recent reverse faulting, which is indicated by focal mechanism solutions, should be the youngest (Holocene or Pleistocene?) event and has very limited deformation on the sea floor and is therefore different from phase 2; or (ii) the earthquake is sourced from a different fault which is not possible to interpreted at seismic sections.

## 5.3. Tectonic Evolution of Study Area

Tectonic evolution of the study area commenced by the deformation of the seismic basement (*unit 4*) as illustrated by deformation of its upper boundary, the horizon 4 (Figure 5.4). Horizon 4 also indicates a deformation style, which is different from horizons 3 and 2, which are lower boundary of the *unit 1* and *unit 2*, respectively. Deformation style of the horizon 4 suggests reverse faulting and indicates compressional or transpressional tectonic environment. This phase ended prior to the deposition of seismic *unit 3* in the study area.

The second phase is represented by the deposition of seismic *units 3, 2 and 1* within fault-controlled basins (labelled as basin A, B and C). During this phase, the reverse faults are inverted and reactivated as normal structures. As the faults continued their activity, the NE−SW trending basins deepened and accommodated sedimentation of seismic units 3, 2 and 1, respectively. The faults also controlled the formation of several intrabasinal highs/ridges.

Recent tectonic setting of the study area is observed especially along the continental shelf and is dominated by strike-slip faults with reverse and/normal components. Although it is difficult to distinguish the effects of recent tectonics setting in highly

deformed basins, the right- and left-lateral strike-slip faults appear to effect seismic *unit 1* and the sea floor.
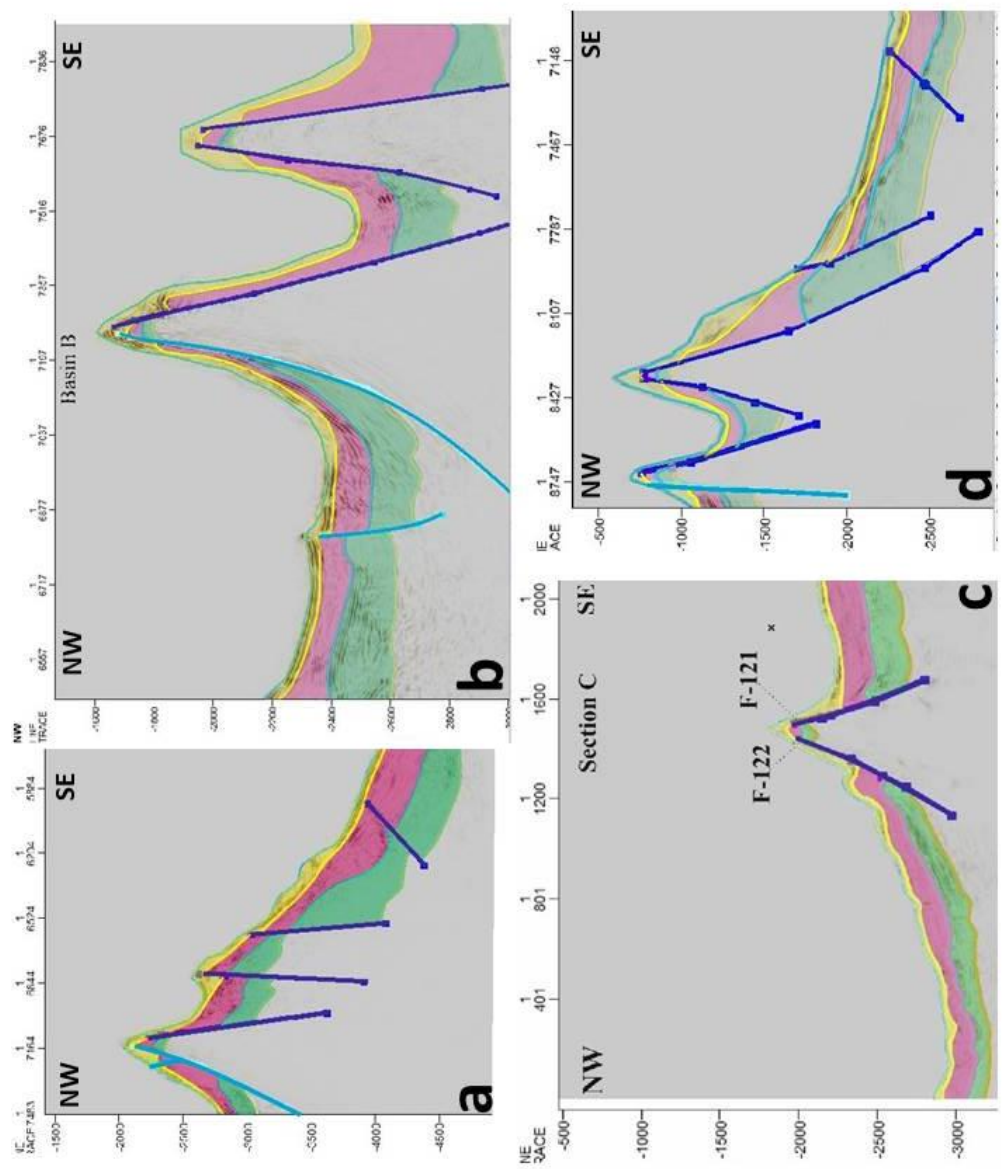


*Figure 5.3. Sections illustrating ridges defined in the basins. From bottom to top units are: gray represents the seismic basement, green is for unit 3, pink illustrates unit 2, and yellow is for unit 1. Dark blue lines – Basin B-bounding faults, light blue lines – basin A-bounding faults. (a) Ridges in section A; (b) ridges in section B; (c) ridges in section B; and (d) ridges in section B.*
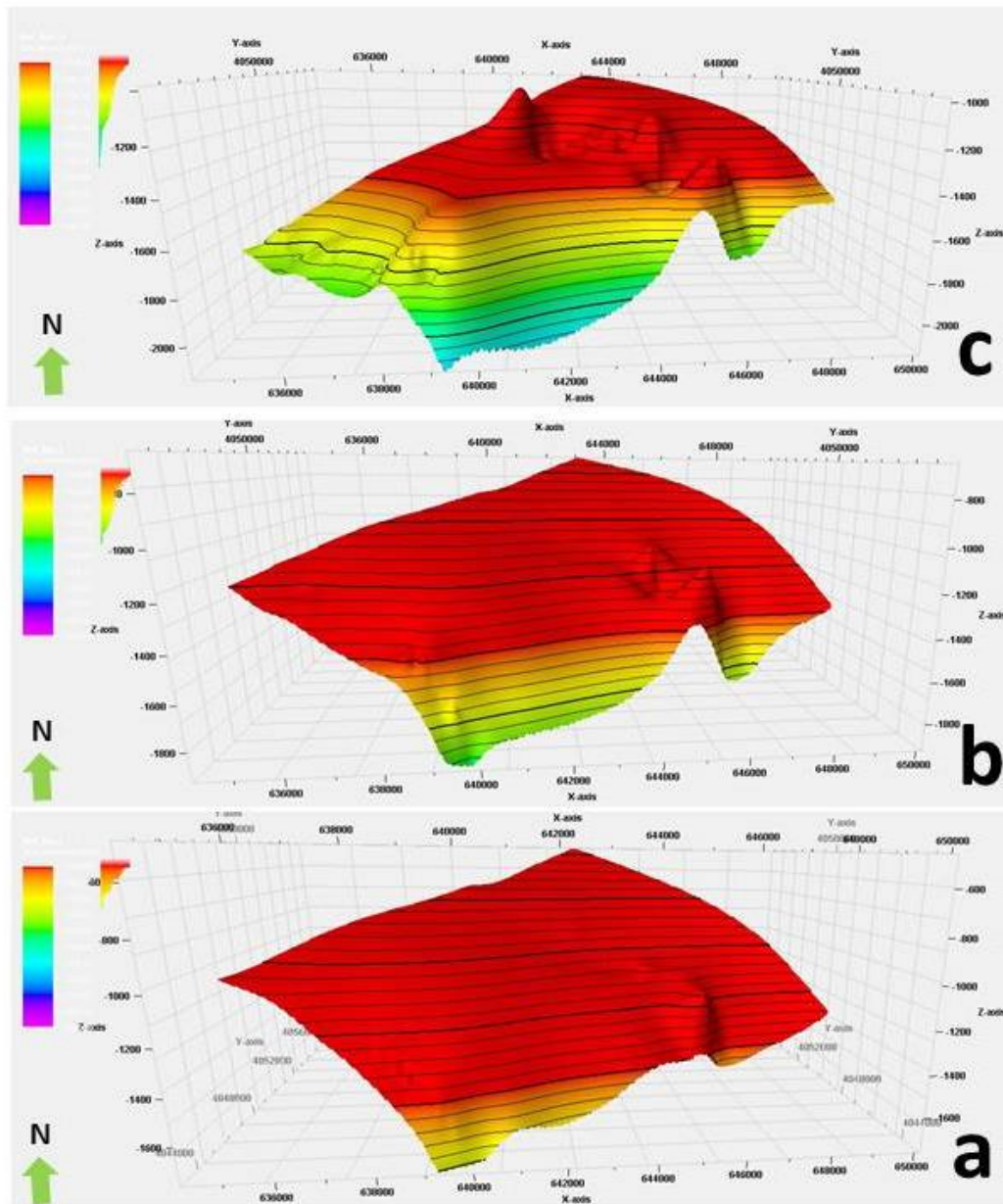
*Figure 5.4. Three surfaces created from horizons defined in the study area: (a) bottom boundary surface of the* seismic unit 1*; (b) upper boundary surface* seismic unit *3; and (c) upper boundary surface of* seismic unit 4 *(seismic basement).*

Focal mechanism solutions of the earthquakes support this contention. The strike-slip nature of the basin bounding structures may suggest a second phase reactivation of tectonic structures, during which normal faults have reactivated as strike-slip structures with mostly normal component.

One of the objectives of the study area is to assess presence and/or continuum of Pliny-Strabo STEP fault zone within the study area and into the Fethiye-Burdur Fault Zone. The available evidence may support the contention that the NE–SW trending fault zone affecting Pleistocene–Quaternary sediments and the sea floor in the study area may be may represent northeastern continuation of the similarly trending faults defined in the Rhodes Basin to the south (cf. Hall et al., 2014a). The linkage of these faults to the Fethiye-Burdur Fault Zone is not possible to clarify; this needs more detailed survey in the area.

Nevertheless, Seismic profiles from the study area therefore include tri-partite prominent seismic stratigraphic units, separated from one another by conspicuous angular unconformities. Two prominent seismic reflectors define the top and bottom of these sedimentary successions. The seismic *unit 1* is the youngest succession in the study area and is presumably tentatively correlated with Pleistocene–Holocene sediments of the onland Çameli-Gölhisar, Eşen, Kasaba, Aksu, Köprüçay and Manavgat basins. The erosional surface may be correlated with Pleistocene angular unconformity defined in onland basins (Çameli, Gölhisar, Eşen and Kasaba basins; cf. Alçiçek, 2007).

The second succession comprises seismic *units 2 and 3* and is overlain by the *unit 1* along a local unconformity; this package is correlated with either (i) middle Miocene–Pliocene sediments of the onland basins if present or (ii) Post- Messinian possibly Pliocene sediments. The oldest seismic *unit 4* forms the basement to the overlying sedimentary succession; its upper boundary also appears as a regional unconformity. The seismic *unit 4* is therefore correlated with the basement of the onland basins. The seismic basement must be represented by pre-Miocene rocks (lower Mesozoic to Oligocene) that form the basement of, and/or Miocene–Pleistocene basin-fill of, onland Çameli, Gölhisar, Eşen and Kasaba basins.

It is therefore concluded, based on the information from the intrabasinal highs/ridges, that the region has experienced three distinct phases of deformation: **(1)** a

contractional regime prior to the deposition of unit 3. This phase may be associated with continent-continent collision between the Anatolide-Tauride platform in the south and Sakarya Continent in the north and the Miocene emplacement of the Lycian Nappes; **(2)** extensional or transtensional regime during which three NE–SW-trending basins (A, B and) and intrabasinal highs/ridges commenced – the basins deepened, ridges become pronounced as similarly trending bounding faults continued to move. The reverse faults have reactivated as similarly trending high-angle normal faults, thus defining NE–SW-trending fault zone; this geological process is described as part of 'reactivation of tectonic structures' that occurred in the eastern Mediterranean (Williams *et al.,* 2009). This phase may be related to either (i) gravitational collapse of the hinterland zone of the Lycian Nappes in response to the lithospheric thickening subsequent to continent-continent collision or (ii) southward rollback of the Aegean arc; **(3)** recent strike-slip regime as suggested by focal mechanism solutions of events occurred along these faults.

It is suggested that the basin evolution is presumably very similar to those of onland Miocene–Pleistocene basins to the north of the study area, like Çameli, Gölhisar, Eşen and Kasaba basins to the north of the study area. The tectonic evolution of these basins may therefore form a reference framework for the study area.

## 5.4. A Review and Comparison of the Literature

Interpretation of seismic sections in and around the study area was also performed by other researchers (Ocakoğlu, 2012; Hall et al., 2014a; Aksu et al., 2019). In fact, in many of these studies seismic sections acquired by MTA Sismik 1 and RV Piri Reis are used in these studies (Figure 5.5). This means many of the seismic sections intepreted during thesis research were already interpreted by others. That is why a comparison of the results from the present work and from others deserves a discussion. One of the main and common conclusions of all of these studies (including the present thesis) is about the structural complexity of the study area and its nearby region.
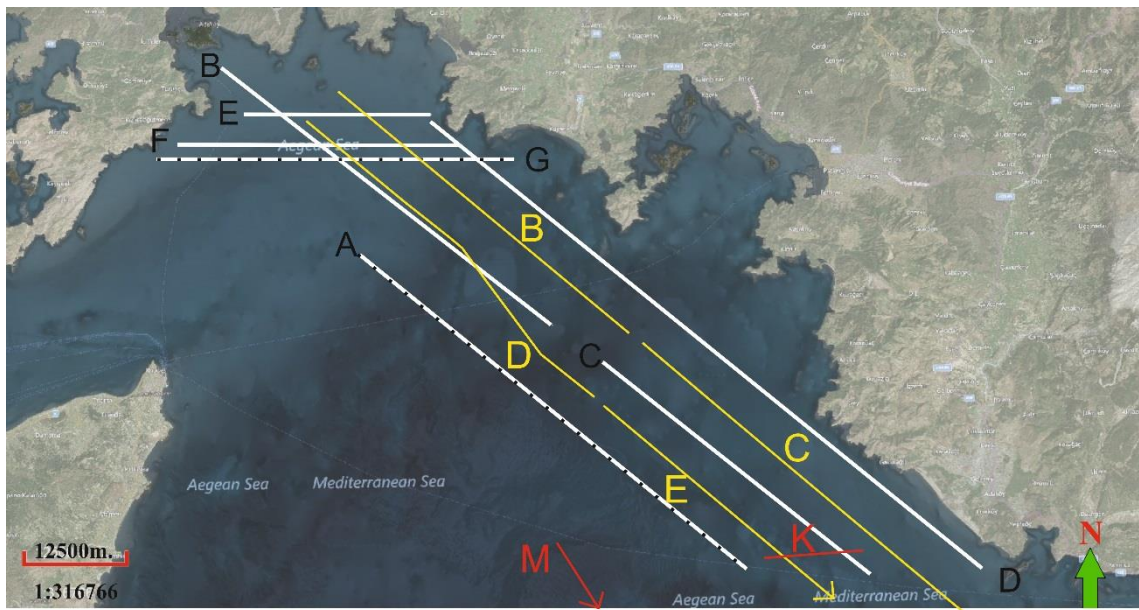
*Figure 5.5. Map showing approximate location of the seismic sections studied by Ocakoğlu (2012), Hall et al., (2014a), and Aksu et al., (2019). Yellow lines indicate interpreted seismic lines in Hall et al., (2014a); red lines, interpreted seismic lines in Aksu et al., (2019); black dashed lines, interpreted common seismic lines in Ocakoğlu (2012). White lines shows interpreted seismic lines in thesis study. Red and yellow arrows indicate extension of seismic sections.*

Ocakoğlu (2012) has already used the same seismic sections. Ocakoğlu (2012) described two seismic units as seismic basement (Cretaceous and Miocene rocks) and overlying Plio–Quaternary basin fill (Figure 5.5 and 5.6.d). The present work defines there seismic units (units 1, 2 and 3) above the basement; these units are defined and differentiated by using seismic stratigraphical features like, erosional truncation, unconformities, initial surface of deposition, etc. The identification of 3 seismic sections contributes to better understanding of fault activity in the study area so that it becomes more obvious and easy to comment on the reactivation of faults. This further means a different structural interpretation of common seismic sections, like seismic section G. For example, delta deposits described in Ocakoğlu (2012) are reinterpreted as a regional landslide. Furthermore at parellel sections E, F and G, respectively at CDP 3400-2500, 0-1500, 6800-5600  points, the delta deposits of Ocakoğlu (2012) are not observable.

114
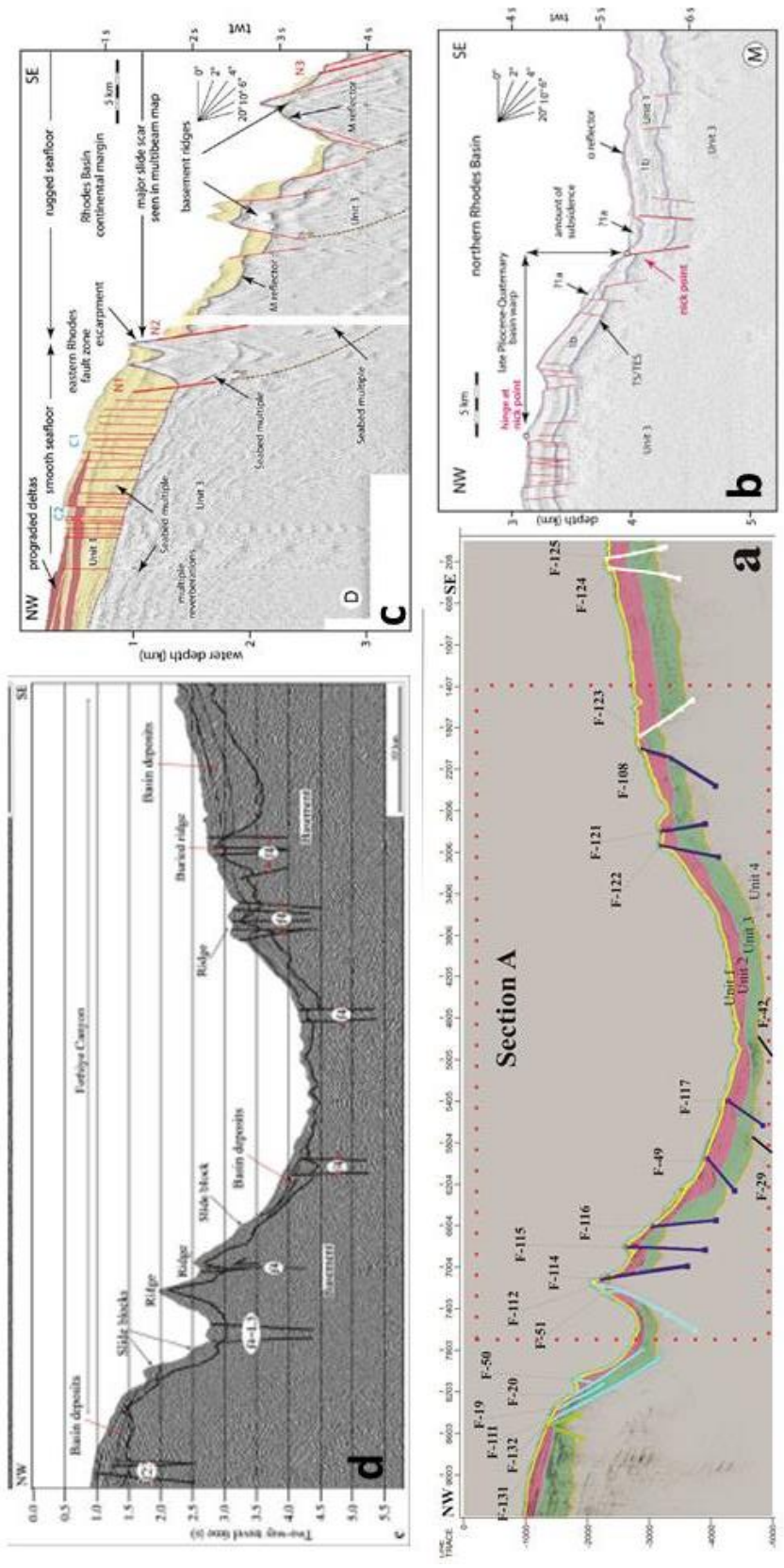
Figure 5.6. Interpreted seismic sections interpreted by Ocakoğlu (2012), (Hall et al., 2014a) and Aksu et al., (2019) and thesis study. (a) Seismic section A from thesis study, shown by black dashed line in Figure 5.5. (b) Seismic section M interpreted by Aksu et al., (2019), indicated with red arrow in Figure 5.5. (c) Seismic section D interpreted by Hall et al., (2014a), shown by yellow line in Figure 5.5. (d) Seismic section A, interpreted by Ocakoğlu (2012), black dashed line in Figure 5.5.

115
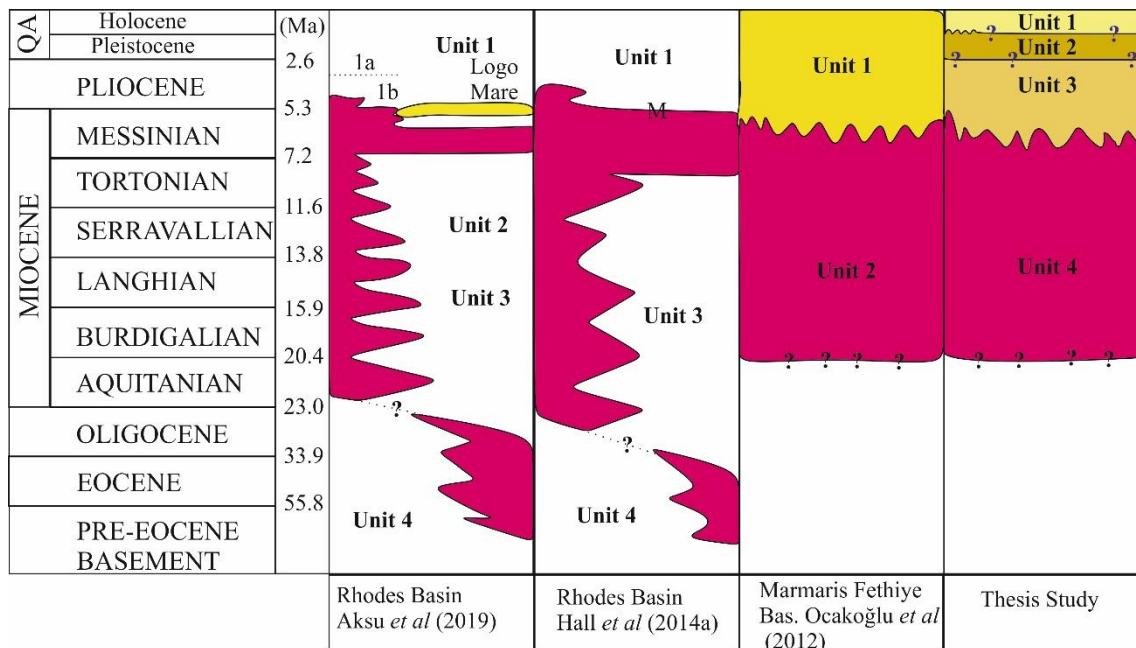
*Figure 5.7. Correlation of the seismic stratigraphy in four studies; they propose different stratigraphic successions. Blue question mark (?) indicates that geologic timing is not precise; black question mark (?), not only geologic timing but also boundary type are not precise.*

This interpretation may arise from a confusion of laterally terminating seismic horizons; this relationship is explained by a regional landslide as explained in Figures 3.6, 3.5 and 3.4. Ocakoğlu (2012) also mentioned about sliding blocks in section A; this will be discussed latter (see discussion on work by Aksu et al., 2019) (Figure 5.6 d).

Ocakoğlu (2012) interpreted the Marmaris fault zone (MFZ) and f-3 faults as synthetic ruptures of the faults that may belong to Pliny-Strabo STEP fault zone. These structures are also interpreted as submarine extension of the FBFZ which goes through the Rhodes island (Figures 5.6d and 5.8d).Whereas moment tensor inversion solution of the events indicates right-lateral motion and this is not compatible with left-lateral strike-slip faulting.

Yellow B, C, D, E lines in Figure 5.5 represent seismic sections interpreted in Hall et al. (2014a). These seismic sections are acquired by RV Koca Piri Reis of the Institute of Marine Sciences and Technology (IMST), Dokuz Eylül University in 2001, 2007,

2008 and 2010. Seismic sections are paralel to sections A, B, C, D seismic lines interpreted in this study. Two seismic units are described by Hall et al. (2014a): a bottom unit of pre-Messinian rocks and a top unit consisting of Plio–Quaternary succesion (Figures 5.6c and 5.7). Normal faults are described as bounding structures of ridges; these faults are interpreted as reactivitated reverse faults. Extension of the basin and basin bounding faults described in this study are also observable in Hall et al. (2014a) sections (Figures 5.6c and 5.8).

Many of the SW–NE-trending faults have been interpreted as dip-slip faults with variable amounts of sinistral strike-slip component (Hall et al., 2014a). These authors also mentioned about existence of faults with dextral component (in addition to sinistral structures) and discussed their role in recent tectonic regime. Upper crustal-scale traces (ofsets, releasing bends, etc that are interpreted to relate the FBFZ) mention in Hall et al. (2014a) can not be observable in the study area. The authors interpreted, based on magnetotelluric studies by Gürer et al. (2004), the faults in the study area as part of a flower structure along the crustal-scale extension of a STEP fault. This is not compatible with the model of the present work as many of the faults are described to have normal components and to control the formation of three subbasins A, B and C. They also provide a fault map with structures aligned in the same direction with those described during this study (Figure 5.6). Likely, many right-to left lateral strike-slip faults with reverse and normal component have been described in Hall et al. (2014a), similar to present study (Table 5.2). It may therefore be wrong to interpret such a deformation zone as a offshore extension of FBFZ in a crustal scale.

Red M, K seismic lines where M extends out of study area (Figure 5.5) are interpreted in Aksu et al. (2019). These seismic sections are acquired by RV Koca Piri Reis of the Institute of Marine Sciences and Technology (IMST), Dokuz Eylül University in 1992, 2001, 2007, 2008 and 2010. E–W-oriented seismic section K crosscuts section C of the present study (Figure 5.5). NW–SE-oriented seismic section extends out of study area and is also almost parallel to seismic section A (Figure 5.5) interpreted by Ocakoğlu (2012).

Two seismic units are described as a bottom unit of pre-Messinian rocks and top unit of Upper Messinian–Quaternary succesion by Aksu et al. (2019). Upper Messinian–Quaternary succesion, *Unit 1* is divided into two subunits as bottom *unit 1b* and Pliocene–Quaternary top *unit 1a* by (Figure 5.7). Seismic horizons are interpreted as a unit 1a corelates *unit 1* of this study. This kind of seismic horizons are also interpreted as a landslides in seismic section A between 4600 and 6200 CDP points. Seismic *unit 1a* of Aksu et al. (2019) are interpreted as part of slide blocks, like in Ocakoğlu (2012) (Figure 5.6a, d). These areas are explained as: '*decapitated nearly the entire uppermost Messinian–Quaternary sub-unit 1a by profound unconformity indicated α-reflector at norheastern margin of Rhodes basin*' by Aksu et al., (2019). 'Profound α–reflector' can not observable in thesis seismic sections where water depth is lower than section M (Figure 5.6b). Aksu et al. (2019) did not mentioned about reactivation of tectonic structures in the Rhodes Basin though they suggest existence of reactivation of tectonic structures in Antalya Basin and Anaximander Mountain. These authors also confirmed the existence of NE–SW-trending faults in the study area (Figure 5.8).

Aksu et al. (2019) intepreted the FBFZ as a zone bounded by two major left-lateral strike-slip faults; these faults has almost the same orientation with right-lateral strike-slip faults described in this study. They suggest that FBFZ is onland extension of the Pliny-Strabo STEP fault zone (Figure 5.8). Although the general trend of the faults share similar orinetations, the nature of the faults interpreted in Aksu et al. (2019) and the present study are contrasting.

Furthermore subsidence that occured in the study area was also explained with 'reactivation of tectonic structures occured during time of deposition unit 3,2 and 1 in theisis study. Observed relative subsidence up to reach 3000 ms at occured section A-B in also huge amount to take place only in short time period defined by Aksu et al. (2019).

It is not possible to observe the traces of the prograde shelf edge delta interpreted in Figure 20 at Aksu et al. (2019), at thesis seismic sections which are closer to the shoreline. Considering that the prograding delta feeding is from the shore to the sea, the structures of this delta development which can be observed in NW–SE direction are not observed in our sections (Figures 3.15b, 3.17b and 3.14b).

Existence of the right-lateral strike-slip faults and their parallelism with already defined left- lateral strike-slip faults in a same are define unexplainable case. A possible explanation requires a more detailed work and may be moment tensor solution of many earthquakes from the same area. Structural complexity of the study area needs to be examined more detailed in future surveys.  For example, 3D seismic surveys can be performed to be ensure fault extension and direction in the study area. Regional velocity model, which is used in moment tensor inversion, should be obtained by further research.
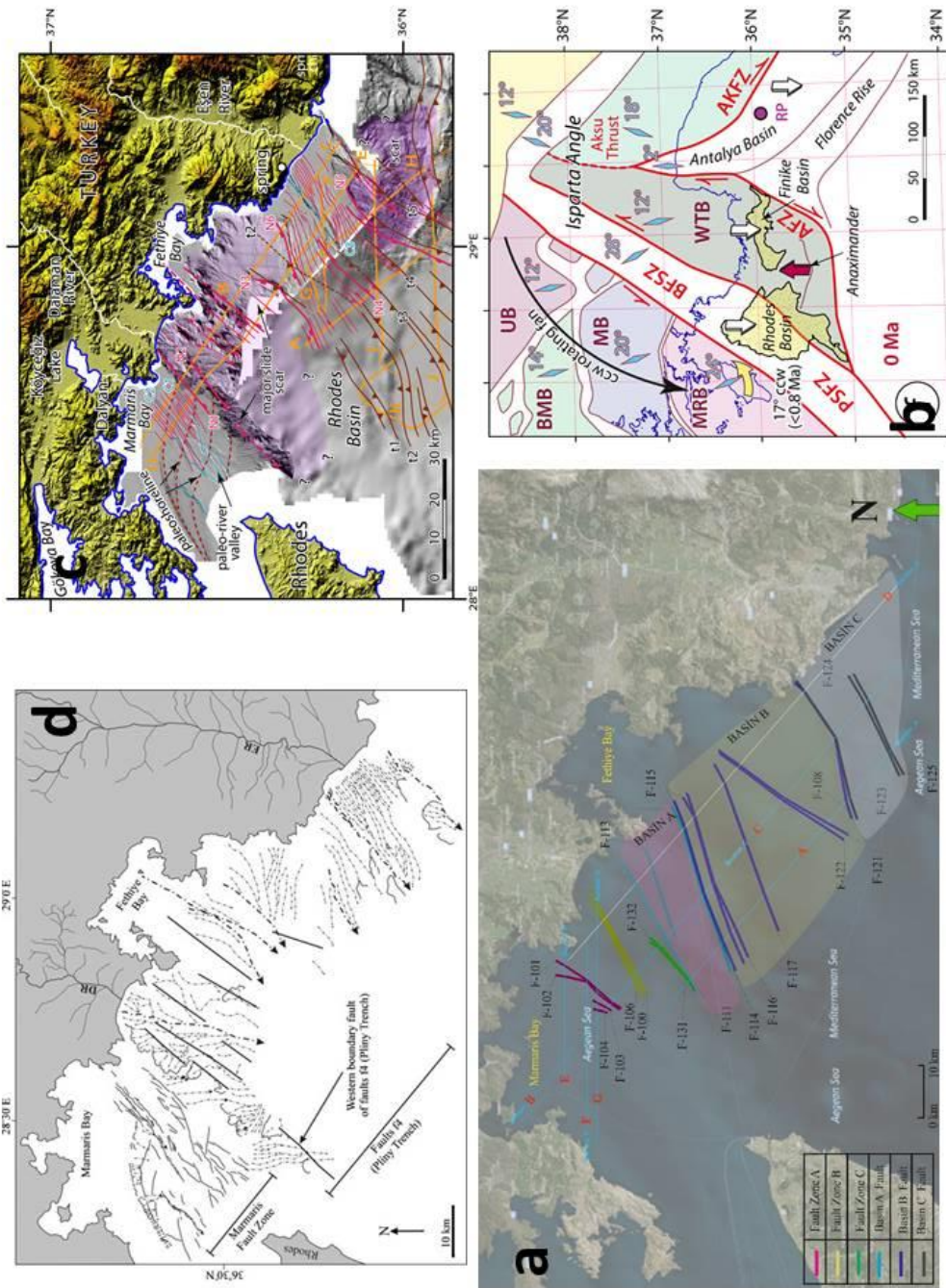
*Figure 5.8. Quaternary and active fault maps of the study area from different researchers and the thesis area. (a) Thesis study; (b) Structural map indicating the FBFZ and Pliny-Strabo STEP fault zone in the study area, from Aksu et al., (2019). (c) Active fault map prepared by Hall et al., (2014a). (d) Active fault map and sediment transportation system (hatch lines) prepared by Ocakoğlu (2012).*

120

# REFERENCES


Agostini, S., Tokcaer, M. and Savaşçın, M. Y. 2010. Volcanic rocks from Foça-Karaburun and Ayvalik-Lesvos grabens (western Anatolia) and their petrogenetic-geodynamic significance. Turkish Journal of Earth Sciences 19 (2), 157-184.

Aksoy, R. and Aksarı, S. 2016. Neogene-Quaternary evolution of the Tefenni basin on the Fethiye-Burdur fault zone, SW Anatolia-Turkey. Journal of African Earth Sciences 118.

Aksu, A.E., Calon, T.J., Hall, J., Mansbridge, S. and Yaşar, D. 2005. The Cilicia–Adana Basin complex, Eastern Mediterranean: Neogene evolution of an active fore-arc basin in an obliquely convergent margin. Marine Geology, 221, 121–159.

Aksu, A.E., Hall, J. and Yaltırak. C. 2005. Miocene to Recent tectonic evolution of the eastern Mediterranean: New pieces of the old Mediterranean puzzle.Marine Geology 1 (221), 1-13.

Aksu, A.E., Hall, J. and Yaltırak, C. 2009. Miocene-Recent evolution of Anaximander Mountains and Finike Basin at the junction of Hellenic and Cyprus Arcs, EasternMediterranean.Mar. Geol. 258, 24–47.

Aksu, A.E., Hall, J. and Yaltırak, C. 2019. Dramatic Pliocene–Quaternary subsidence of the southern Rhodes Basin and concomitant north-tilting and uplift of the Anaximander Mountains, the junction of Hellenic and Cyprus arcs, eastern Mediterranean Sea. Tectonophysics 762 (2019) 121–143.

Akyüz, H.S. and Altunel, E. 2001. Geological and archaeological evidence for post-Roman earthquake surface faulting at Cibyra, SW Turkey. Geodinamica Acta 14, 1–7.

Alçiçek, M.C., Kazancı, N. and Özkul, M. 2005. Multiple rifting pulses and sedimentation pattern in the Çameli Basin, southwestern Anatolia, Turkey. Sedimentary Geology, 173,409–431.

Alcicek M.C., Veen, J.T. and Özkul, M. 2006. Neotectonic development ofthe Cameli Basin, south-western Anatolia, Turkey. Geol Soc Spec Publ 260: 591-611.

Alçiçek, M.C. 2007. Tectonic development of an orogen-top rift recorded by its terrestrialsedimentation pattern: the Neogene Eşen Basin of southwestern Anatolia, Turkey. Sedimentary Geology, 200, 117–140.

Alçiçek, M.C. and Veen, J.H. 2008. The late Early Miocene Acıpayam piggy-back basin: refining the last stages of Lycian nappe emplacement in SW Turkey. Sedimentary Geology, 208 (3), 101–113.

Alçiçek, M.C., Brogi, A., Capezzuoli, E., Liotta, D. and Meccheri, M. 2013. Superimposed basins formation during the Neogene-Quaternary extensional tectonics in SW-Anatolia (Turkey): insights from the kinematics of the Dinar Fault Zone. Tectonophysics 608,713–727.

Alçiçek M.C. 2015. Comment on "Tectonophysics 635, 80-99 by J. Hall et al.," Tectonophysics 664, 1-4.

Alçiçek M.C., van den Hoek, Ostende, L.W., Saraç, G., Tesakov, A.S., Murray, A.M., Hakyemez, H.Y., Göktaş, F., Mayda, S., Jimenez-Moreno, G., Büyükmeriç, Y., Wesselingh, F.P., and Alçiçek, H. 2018. Comment on "Tectonophysics 690, 336-354 by İ. Elitez and C. Yaltırak" Tectonophysics 722, 595-600.

Ambraseys N. 1962. Data for the investigation of the seismic seawaves in the Eastern Mediterranean. Bull. Seism. Soc. Am., 52 (4), 895-913.

Ambraseys, N. and Adams, R.D. 1993. Seismicity of the Cyprus region. Terra Nova 5(1), 85-94.

Ambraseys, N.N., Melville, C.P. and Adams, R.D. 1994. The Seismicity of Egypt, Arabia and the Red Sea. Cambridge, Cambridge University Press, 182 p.

Ambraseys, N.N. and Finkel C. 1995. The Seismicity of Turkey and adjacent areas. A Historical Review, 1500-1800. Eren, Istanbul, 240 p.

American Association of Petroleum Geologists Encyclopedia of Geoscience https://wiki.aapg.org/Seismic_processing_basics)  Last accesed July 2019.

Amundsen L. and Reitan, A. 1995. Decomposition of multicomponent sea-floor data into upgoing and downgoing P- and S-waves. Geophysics, 60, 563–572.

Baes M, Govers R, Wortel MJR (2011). Subduction initiation along the inherited weakness zone at the edge of a slab: insights from numerical models. Geophys J Int 184: 991-1008.

Barka, A., Reilinger, R., Saroğlu, F. and Şengör, A.M.C. 1995. The Isparta Angle: its importance in the neotectonics of the eastern Mediterranean region. In: Pişkin, Ö., Ergün, M., Savaşçin, M.Y., and Tarcan, G. (Eds.), Proceedings of the International Earth Sciences Colloquium on the Aegean Region-1995 3–17 pp.

Barka, A.A. and Reilinger, R. 1997. Active tectonics of the Eastern Mediterranean region: deduced from GPS, neotectonic and seismicity data. Annali di Geofi sica 40, 587–610

Becker, J.J. et al., 2009. Global bathymetry and elevation data at 30 arcseconds resolution: SRTM30_PLUS, Mar. Geod., 32(4), 355–371.

Becker, D. and Meier, T. 2010. Seismic slip deficit in the southwestern forearc of the Hellenic subduction zone. Bulletin of the Seismological Society of America, 100 (1), 325–342.

Benetatos, C., Kiratzi, A., Papazachos, C. and Karakaisis, G. 2004. Focal mechanisms of shallow and intermediate depth earthquakes along the Hellenic Arc. Journal of Geodynamics 37, 253–296.

Bessiere, E., Rabillard, A., Precigout, J. and Mansard, N. 2018. Strain localization within a syntectonic intrusion in a back-arc extensional context: The Naxos Monzogranite (Greece). Tectonics 37(2):558-587

Biryol, C., Beck, S.L., Zandt, G. and Özacar, A.A. 2011. Segmented African lithosphere beneath the Anatolian region inferred from teleseismic P-wave tomography. Geophys. J. Int. 184, 1037–1057.

Bonev, N., Beccaletto, L., Robyr, M. and Monie, P., 2009. Metamorphic and age constraints on the Alakeçi shear zone: Implications for the extensional exhumation history of the northern Kazdağ Massif, NW Turkey. Lithos 113(1)

Bonev, N., Marchev, P., Moritz, R. and Filipov, P. 2015. Timing of igneous accretion, composition, and temporal relation of the Kassandra–Sithonia rift-spreading center within the eastern Vardar suture zone, Northern Greece: insights into Jurassic arc/back-arc systems evolution at the Eurasian plate margin, International Journal of Earth Sciences 104(7).

Bohnhoff, M., Harjes, H.P. and Meier, T. 2005. Deformation and stress regimes in the Hellenic subduction zone from focal mechanisms. J. Seismol. 9, 341–366.

Bozcu, M., Yağmurlu, F., and Şentürk, M. 2007. Some Neotectonic and Paleoseismological features of the Fethiye-Burdur Fault zone, SW Anatolia. Geol. Eng. 31 (1), 25–48.

Bozkurt, E. 2001. Neotectonics of Turkey−a synthesis. Geodinamica Acta 14: 3-30.

Bozkurt, E. and Sözbilir, H. 2004. Tectonic evolution of the Gediz Graben: field evidence for an episodic, two-stage extension in western Turkey. Geological Magazine, 141, 63-79.

Bozkurt, E. 2007. Extensional v. contractional origin for the southern Menderes shear zone, SW Turkey: tectonic and metamorphic implications. Geological Magazine 144 (1), 191-210

Bozkurt, E., Satır, M., and Buğdaycıoğlu, C. 2011a. Surprisingly y ung Rb/Sr ages fr the Simav extensional detachment fault zone, northern Menderes Massif, Turkey: Journal of Geodynamics, v. 52, p. 406–431.

Caldwell, J. 1999. Marine multicomponent seismology. Leading Edge , 18, 1274–1282.

Canbay, E. 2009. Fethiye Burdur fay kuşağının güneybatı uzantısının kinematik özellikleri. MSc. Thesis, Istanbul University, 254 p.

Caputo, M., Panza, G.F. and Postpischl, D. 1970. Deep structure of the Mediterranean Basin, J. geophys. Res., 75(26), 4919–4923.

Catlos, E.J. and Çemen, İ. 2005. Monazite ages and the evolution of the Menderes Massif, western Turkey. International Journal of Earth Sciences 94: 204-217.

Cavazza, W., Catto, M., Okay, A.I. and Reiner, P. 2018. Thermochronology of the Miocene Arabia-Eurasia collision zone of southeastern Turkey. Geosphere (2018) 14 (5): 2277-2293.

Cavazza, W., Okay, A.I., Zattin, M. 2009. Rapid early-middle Miocene exhumation of the Kazdag metamophic core complex (Western Anatolia), International Journal of Earth Sciences, 98, 1935 - 1947 pp.

Coşkuner, B., Eren, Y., Demircioğlu, R. and Aksoy, R. 2019. Fethiye Burdur fay zonu'nun kuzeydoğu kesiminin (burdur-güneybatı anadolu) göreceli tektonik aktivitesinin jeomorfik indislerle incelenmesi. Geological Bulletin of Turkey 62.

Chaumillon, E. and Mascle, J. 1997. From foreland to forearc domains: new multichannel seismic reflection survey of the Mediterranean Ridge accretionary complex (Eastern Mediterranean), Mar. Geol., 138(3), 237–259.

Çiftçi, N. B. and Bozkurt, E., Folding of the Gediz Graben Fill, SW Turkey: Extensional and/or Contractional Origin. "Geodinamica Acta", 21, (2008), p.145-167.

Çiftçi, N. B. and Bozkurt, E. 2009. Pattern of normal faulting in the Gediz Graben, SW Turkey. "Tectonophysics", 473, 234-260 p.

Çiftçi, N. B. and Bozkurt, E. 2010. Tructural evolution of the Gediz Graben, SW Turkey: temporal and spatial variation of the graben fill. "Basin Research", 22, 846-873 p.

Dahmn, T. 1996. Relative moment tensor inversion based on ray theory: theory and synthetic tests. Geophysical Journal International, 124, 245-257

de Boorder, H., Spakman, W., White, S.H. and Wortel, M.J.R. 1998. Late Cenozoic mineralization, orogenic collapse and slab detachment in the European Alpine Belt. Earth Planet. Sci. Lett. 164, 569–575.

DeMets, C., Gordon, R.G.R. and Argus, D.D.F. 2010. Geologically current plate motions, Geophys. J. Int., 181(1), 1–80

Dewey, J.F., Pitman, W.C., Ryan W.B .F. and Bonnin, J. 1973. Plate tectonics and evolution of the Alpine system.Geological Society of America Bulletin,. 84, 3137-3180.

Dewey, F. and Şengor, A.M.C. 1979. Aegean and surrounding regions: complex multiple and continuum tectonics in a convergent zone. Geological Society of America Bulletin, 90, 84-92.

Dewey, J.F., Hempton, M.R., Kidd, W.S.F., Şaroğlu, F. and Xengfr, A.M.C. 1986. Shortening of continental lithosphere: the neotectonics of eastern Anatolia—a young collision zone. In:Coward, M.P., Ries, A.C. (Eds.), Collision Tectonics, Geological Society Special Publication, vol. 19, 3 – 36 pp.

126

Dilek, Y. and Sandvol, E. 2009. Seismic Structure, Crustal architecture and tectonic evolution of the anatolian-african plate boundary and the cenozoic orogenic belts in the eastern Mediterranean region, in Murphy, B., Keppie, J.D., and Hynes, A., eds., Ancient Orogens and modern analogues, Geological Society of London Special Publication, 327, 127–160 p.

Dondurur, D., (2018) Acquisition and Processing of Marine Seismic Data, Elsevier, 606, 211-239 p.

Dumont, J.F., Poisson, A. and Şahinci, A. 1979. Sur l'existence de coulissements sénestres récents a l'extrémité orientale de l'arc Égéen (sud-ouest de la Turquie). C. R. Acad.Sci. Paris 289, 261–264.

Dziewonski, A. M., Chou, T. A. and Woodhouse, J. H. 1981. Determination of earthquake source parameters from waveform data for studies of global and regional seismicity. Journal of Geophysical Research, 86, 2825–2852.

Edme, P. and Singh, S.C. 2008. Receiver function method in reflection seismology. Geophysical Prospecting, 56, 327–340

Elitez, İ. and Yaltırak, C. 2014a. Burdur-Fethiye shear zone (Eastern Mediterranean, SW Turkey). General Assembly European Geosciences Union (EGU). 27 April-2 May 2014. Austria, Vienna.

Elitez, İ. and Yaltırak, C. 2014b. Miocene-Quaternary geodynamics of Çameli Basin, Burdur-Fethiye shear zone (SW Turkey). Geological Bulletin of Turkey, 57 (3), 41–67.

Elitez, İ. and Yaltırak, C., Hall, J., Aksu, A.E. and Çifçi, G. 2015. Reply to the comment by M.C. Alçiçek on "The Fethiye–Burdur Fault Zone: a component of upper plate extension of the subduction transform edge propagator fault linking Hellenic and Cyprus Arcs, Eastern Mediterranean," Tectonophysics, 635, 80–99. Tectonophysics, 664, 5–13.

Elitez, İ., Yaltırak, C. and Sunal. G. 2017. A new chronostratigraphy (40Ar-39Ar and U-Pb Dating) for the Middle Section of the Burdur-Fethiye Shear Zone, SW Turkey. EGU General Assembly Conference Abstracts 19, 180.

Elitez, İ. and Yaltırak, C. 2018. Reply to the comment on "Miocene to Quaternary tectonostratigraphic evolution of the middle section of the Burdur-Fethiye Shear Zone, south-western Turkey: implications for the …Tectonophysics 722, 601-606.

Elitez, İ. and Yaltırak, C. 2016. Miocene to Quaternary tectonostratigraphic evolution of the middle section of the Burdur-Fethiye Shear Zone, southwestern Turkey: implications for the wide inter-plate shear zones. Tectonophysics, 690, 336-354

Emre, Ö., Duman, T.Y., Özalp, S., Elmacı, H., Olgun, Ş. and Şaroğlu, F. 2013. Açıklamalı Türkiye diri fay haritası. ölçek 1:1.250.000, VI+89s.+bir pafta, Maden Tetkik ve Arama Genel Müdürlüğü, Özel Yayın Serisi-30, Ankara-Türkiye.

Encyclopedia of Subsurface Science. http://subsurfwiki.org/wiki/Gather last accesed July 2019 Last accesed July 2019

Eyidogan, H. and Barka, A. 1996. The 1 October 1995 Dinar earthquake, SW Turkey, Terra Nov., 8(5), 479–485.

Etter, P.C. 2018. Underwater Acoustic Modeling and Simulation 5th Edition CRC Press 638 pages, 9780429225383.

European-Mediterranean Seismological Centre websitehttps://www.emsc-csem.org/Earthquake/earthquake.php?id=752096#

Faccenna, C., Bellier, O., Martinod, Piromallo, C. and Regard, V. 2006. Slab detachment beneath eastern Anatolia: A possible cause for the formation of the North Anatolian fault. Earth and Planetary Science Letters, 242, 1–2.

Foulger, G.R. and Julian, B.R. 1993. Non double couple earthquakes at the Hengill-Greensdalur volcanic complex, Iceland Are they artifacts of crustal heterogeneity?, Bull. seism. Soc. Am., 83, 38-52.

Geoprocesados: Geoscience Services Company http://geoprocesados.com/english/nuestros-servicios/procesamiento-sismico-crs/index.html Last accesed July 2019

Gessner, K., Gallardo, L. A., Markwitz, V. and Ring, U. 2013. What caused the denudation of the Menderes Massif: Review of crustal evolution, lithosphere structure, and dynamic topography in southwest Turkey. Gondwana Research. 24(1): 243–274.

Gessner, K., Markwitz, V. and Güngör, T. 2018. Crustal fluid flow in hot continental extension: Tectonic framework of geothermal areas and mineral deposits in western Anatolia. Geological Society Special Publication. 453, 1, 289-311 p.

Glover, C. and Robertson, A.H.F. 1998a. Neotectonic intersection of the Aegean and Cyprus tectonic arcs: extensional and strike-slip faulting in the Isparta Angle, SW Turkey. Tectonophysics 298, 103–132.

Glover, C. and Robertson, A.H.F. 1998b. Role of extensional processes and uplift in the PlioQuaternary sedimentary and tectonic evolution of the Aksu Basin, south west Turkey. J. Geol. Soc. Lond. 155, 335–365.

Govers, R. and Wortel, M.J.R. 2005. Lithosphere tearing at STEP faults: response to edges of subduction zones. Earth and Planetary Science Letters 236(1–2), 505-523.

Granot, R. 2016. Palaeozoic oceanic crust preserved beneath the easternMediterranean, Nat. Geosci., 9(9), 701–705.

Gürer, A., Bayrak, M. and Gürer, Ö.F. 2004. Magnetotelluric images of the crust and mantle inthe southwestern Taurides, Turkey. Tectonophysics 391, 109–120.

Hall, J., Aksu, A.E., Calon, T.J. and Yaşar, D. 2005. Varying tectonic control on basin development at an active microplate margin: Latakia Basin Eastern Mediterranean. Marine Geology, 221, 15–60.

Hall, J., Aksu, A.E., Elitez, İ., Yaltırak, C. and Çifçi, G. 2014a. The Fethiye–Burdur Fault Zone: a component of upper plate extension of the subduction transform edge propagator fault linking Hellenic and Cyprus Arcs, Eastern Mediterranean. Tectonophysics 635, 80–99

Hall, J., Aksu, A.E., Yaltırak, C. and Winsor, J.D. 2009. Structural architecture of the Rhodes Basin: a deep depocentre that evolved since the Pliocene at the junction of Hellenic and Cyprus Arcs, eastern Mediterranean. Marine Geology, 258, 1–23.

Hancock, P.L. and Barka, A.A. 1981. Opposed shear senses inferredfrom neotectonic mesofractures systems in the North Anatolianfault zone. J. Struct. Geol. 3, 383– 392.

Hatzfeld, D. 1994. On the shape of the subducting slab beneath the Peloponnese, Greece, Geophys. Res. Lett., 21(3), 173–176.

Hatzfeld, D. and Martin, C. 1992. Intermediate depth seismicity in the Aegean defined by teleseismic data, Earth planet. Sc. Lett., 113, 267-275.

Herrman, R.B. 2015. Computer Programs in Seismology Moment Tensor Inversion Virtual Box VDI Distribution, Tutorial 65 P. https://ds.iris.edu/media/workshop/2015/09/iris-international-development-seismology/files/presentations/MomentTensor2015_01.pdf

Hidas, K., Garrido, C., Rea, G. B. and Marchesi, C. 2019. Lithosphere tearing along STEP faults and synkinematic formation of lherzolite and wehrlite in the shallow subcontinental mantle.  Solid Earth 10(4), 1099-1121

Hollenstein, C., Müller, M.D., Geiger, A. and Kahle, H.G. 2008. Decade of GPS measurements, 1993–2003 Tectonophysics 449, 1–4.

Huguen, C., Mascle, J., Chaumillon, E., Woodside, J.M., Benkhelil, J., Kopf, A. and Volkonska˙ıa, A. 2001. Deformational styles of the easternMediterranean Ridge and surroundings from combined swath mapping and seismic reflection profiling.Tectonophysics, 343(1), 21–47.

Huguen, C., Chamot-Rooke, N., Loubrieu, B. and Mascle, J. 2006. Morphology of a pre-collisional, salt-bearing, accretionary complex: The Mediterranean Ridge (eastern Mediterranean), Mar. Geophys. Res., 27(1), 61–75. International Seismological Centre, 2017. On-line Bulletin.

Irmak, T.Ş., Karakaş, A. and Kalafat, D. 2015. Seismotectonic Content by the Source Parameters of the 10 June 2012 Ölüdeniz-Fethiye (Dodecanese Islands) Mw 6.1 Earthquake and Aftershocks (southwestern Turkey). Acta Geod Geophys, DOI 10.1007/s40328-015-0106-8.

İşler, F.I., Aksu, A.E., Hall, J., Calon, T.J. and Yaşar, D. 2005. Neogene development of the Antalya Basin, Eastern Mediterranean: an active fore-arc basin adjacent to an arc junction.Mar. Geol. 221, 299–330.

Jackson, J. and McKenzie, D. 1984. Active tectonics of theAlpine–Himalayan Belt between western Turkey and Pakistan, Geophys. J. Int., 77(1), 185–264.

Jolivet, L., 2001, A comparison of geodetic and finite strain pattern in the Aegean, geodynamic implications: Earth and Planetary Science Letters, 187(1-2), 95–104 p.

Jolivet, L. and Brun, J.P. 2010. Cenozoic geodynamic evolution of the Aegean region: International Journal of Earth Sciences, 99, 109–138 p.

Jolivet, L., Faccenna, C., Goffé, B., Burov, E., and Agard, P. 2003. Subduction tectonics and exhumation of highpressure metamorphic rocks in the Mediterranean orogens: American Journal of Science, 303, 353–409 p.

Jolivet, L., Famin, V., Mehl, C., Parra, T., Aubourg, C., Hébert, R., and Philippot, P. 2004. Strain localization during crustal-scale boudinage to form extensional metamorphic domes in the Aegean Sea, in Whitney, D.L., Teyssier, C., and Siddoway, C.S., eds., Gneiss Domes in Orogeny: Geological Society of America Special Paper 380, 185–210 p.

Jolivet, L., Lecomte, E., Huet, B., Denèle, Y., Lacombe, O., Labrousse, L., Le Pourhiet, L., and Mehl, C. 2010. The North Cycladic detachment system: Earth and Planetary Science Letters, 289, 87–104 p.

Jolivet, L., Faccenna, C., Huet, B., Labrousse, L., Le Pourhiet, L., Lacombe, O., Lecomte, E., Burov, E., Denèle, Y. and Brun, J. P. 2013. Aegean tectonics: Strain localisation, slab tearing and trench retreat: Tectonophysics, 597–598, 1–33 p.

Jolivet, L., Menant, A., Sternai, P., Rabillard, A., Arbaret, A., Augier, R., Laurent, V., Beaudoin, A., Grasemann, B., and Huet, B. 2015. The geological signature of a slab tear below the Aegean: Tectonophysics, 659, 166– 182 p.

Jolivet, M., Gardel, A., and Anthony, E. J. 2019. Multi-decadal changes on the mud-dominated coast of western French Guiana: implications for mesoscale shoreline mobility, river-mouth deflection, and sediment sorting. J. Coast. Res. 82, (in press).

Jongsma, D. 1977. Bathymetry and shallow structure of the Pliny and Strabo trenches, south of the Aegean Arc. Geological Society of America Bulletin, 88, 797-805.

Jongsma, D., van Hinte, J.E. and Woodside, J.M. 1985. Geological structure and neotectonics of the north African continental margin south of Sicily. Mar. Pet. Geol. 2, 156– 179.

Jongsma, D., Woodside, J.M., King, G.C.P. and van Hinte, J.E. 1987. The Medina Wrench: a key to the kinematics of the central andeastern Mediterranean over the past 5 Ma. Earth Planet. Sci.Lett. 82, 87–106.

Kahle, H.G., Cocard, M., Peter, Y., Geiger, A., Reilinger, R., Barka, A. and Veis, G. 2000. GPS derived strain rate field within the boundary zones of the Eurasian, African, and Arabian Plates. Journal of Geophysical Research, 105, 23.353–23.370.

Karabacak, V. 2011. Geological, geomorphological and archeoseismological observations along the Cibyra fault and their implications on the regional tectonic of SW Turkey, Turkish Journal of Earth Sciences, 20, 429-447

Kaymakci, N., Inceöz, M., Ertepinar, P. and Koç, A. 2010. Late Cretaceous to Recent kinematicsof SE Anatolia (Turkey). Geological Society Special Publications.

Kaymakci, N., Langereis, C., Özkaptan, M., Özacar, A.A., Gülyüz, E., Uzel, B. and Sözbilir, H. 2017. Fethiye–Burdur Fault Zone (SW Turkey): a myth? In: General Assembly Conference Abstracts, 19, 5443 p.

Kaymakci, N., Langereis, C., Özkaptan, M., Özacar, A.A., Gülyüz, E., Uzel, B. and Sözbilir, H. 2018. Paleomagnetic evidence for upper plate response to a STEP fault, SW Anatolia: Earth and Planetary Science Letters, 498 101–115

Kawakatsu, H. 1991. Enigma of earthquakes at ridge-transform fault plate boundaries-Distribution of non-double-couple parameter of Harvard CMT solutions. Geophysical Research Letter, 18, 1103-1106

Kawakatsu, H. 1995. Automated near-realtime CMT inversion.Geophysical Research Letter, 22, 2569–2572, doi:10.1029/95GL02341.

Ketin, İ. 1948. Uber die tektonisch-mechanischen Folgerungen aus den grossen anatolischen Erdbeben des letzten Dezenniums.Geol Rundsch 36: 77-83 (in German).

Kikuchi, M. and Kanamori, H. 1991. Inversion of complex body wave-III. Bulletin of the Seismological Society of America, 81, 2335-2350.

Koçyiğit, A., Yusufoğlu, H. and Bozkurt, E. 1999. Evidence from the Gediz graben for episodic two-stage extension in western Turkey. Journal of the Geological Society, London 156: 605−616.

Koçyiğit, A. 2000. Güneybatı Türkiye'nin depremselliği: Batı Anadolu'nun depremselliği sempozyumu (BAD SEM2000), Bildiriler, s: 30-38.

Kuge, K. and Kawakatsu, H. 1992. Deep and intermediate-depth nondouble couple earthquakes: Interpretation of moment tensor inversions using various passbands of very broadband seismic data. Geophysical Journal International, 111, 589-606.

Le Pichon, X. and Angelier, J. 1979. The Hellenic Arc and trench system: a key to the evolution of the eastern Mediterranean area. Tectonophysics, 60, 1–42

Le Pichon, X., Chamot-Rooke, N., Lallemant, S., Noomen, R. and Veis, G. 1995. Geodetic determination of the kinematics of central Greece with respect to Europe. Journal of Geophysical Research, 100, 12.675–12.690.

Le Pichon, X., Angelier, J., Aubouin, J., Lyberis, N., Monti, S., Renard, V., Got, H., Hsli, K., Marty, Y., Mascle, J., Mathews, D., Mitropoulos, D., Tsotlies, P. and Chronis, G. 1979. From subduction to transform motion: a seabeam survey of the Aegean trench system. Earth and Planetary Science Letters ,44, 441-450.

Le Pichon, X. and Kreemer, C. 2010. The miocene-to-present kinematic evolution of the eastern mediterranean and middle east and its implications for dynamics Annual Review of Earth and Planetary Sciences, 38(1) 323-351 p.

Le Pourhiet, L., Huet, B., May, D. and Labrousse, L. 2012. Kinematic interpretation of the 3D shapes of metamorphic core complexes. Geochemistry Geophysics Geosystems 13(9).

Lecomte, E., Jolivet, L., Lacombe, O., Denèle, Y., Labrousse, L., and Le Pourhiet, L. 2010. Geometry and kinematics of a low-angle normal fault on Mykonos island (Cyclades, Greece): evidence for slip at shallow dip: Tectonics, 29, 5012 p.

Leite, O. and Mascle, J. 1982. Geological structures on the south Cretan continental margin and Hellenic trench (eastern Mediterranean). Mar. Geol. 49, 199–223.

Macdonald, W.D. 1980. Net Tectonic rotation, apparent tectonic rotation, and the structural tilt correction in paleomagnetic studies, Journal of Geophysical Research, 85(B7), 3659-3669 pp.

Mascle, J. et al., 1982. The Hellenic margin from eastern Crete to Rhodes: Preliminary results, Tectonophysics, 86(1–3), 133–147.

Mascle, J., Cleac'h, A. and Jongsma, D. 1986. The eastern Hellenic margin from Crete to Rhodes: Example of progressive collision, Mar. Geol.,73(1–2), 145–168.

Mascle, J., Benkhelil, J., Bellaiche, G., Zitter, T., Loncke, Prismed II Scientific Party, 2000. Marine geologic evidence for a Levantine–Sinai plate, a new piece of the Mediterranean puzzle.Geology 28, 779– 782.

Meulenkamp, J.E., Wortel, M.J.R., van Wamel, W.A., Spakman, W., and Strating, E.H. 1988. On the Hellenic subduction zone and the geodynamic evolution of Crete since the late Middle Miocene. Tectonophysics 146, 203–215.

McClusky, S. and Balassanıan, S., 2000. Global Positioning System constrains on plate kinematics and dynamics in the eastern Mediterrenean and Caucasus, Journal Of Geophysical Research, 105 5695-5719

McKenzie, D.P. 1970. Plate tectonics of the Mediterranean region. Nature, 220, 239-243

McKenzie D.P. 1972. Active tectonics of the Mediterranean region. Geophys. J. Royal Astron. Soc. 30 109-185.

McKenzie, D. P. 1976. The East Anatolian Fault; a major structure in eastern Turkey. Earth and Planetary Science Letters, 29(1), 189-193.

McKenzie, D. 1978a. Active tectonics of the Alpine–Himalayan belt: the Aegean Sea and surrounding regions, Geophys. J. R. astr. Soc., 55, 217– 254.

McKenzie, D. 1979. Finite deformation during fluid flow. Geophysical Journal International. 58(3), 689-715.

McQuarrie, N., and van Hinsbergen, D. J. 2013. Retrodeforming the Arabia-Eurasia Collision zone: Age of collision versus magnitude of continental subduction, Geology 41(3), 315-318.

Menant. A., Jolivet. L., Augier, R. and Skarpelis, N. 2013. The North Cycladic Detachment System and associated mineralization, Mykonos, Greece: Insights on the evolution of the Aegean domain. Tectonics 32(3)

Mutlu, A.K. and Karabulut, H. 2011. Anisotropic Pn tomography of Turkey and adjacent regions. Geophysical Journal International 187, 1743–1758.

Müller, R.D., Dutkiewicz, A., Seton1, M. and Gaina. C. 2013. Seawater chemistry driven by supercontinent assembly, breakup, and dispersal. Geology, 41(8), 907–910 p.

Nocquet, J.M. 2012. Present-day kinematics of the Mediterranean: A comprehensive overview of GPS results. Tectonophysics 579:220–242

Nur, A. and Ben-Avraham Z. 1978. The eastern Medi terranean and the Levant: tectonics of continental collision.Tectonophysics, 46, 297- 311.

Ocakoğlu, N. 2012. Investigation of Fethiye-Marmaris Bay (SW Anatolia): seismic and morphologic evidences from the missing link between the Pliny Trench and the Fethiye-Burdur Fault Zone. Geo-Marine Letters 32, 17-28.

Okay, A.I. and Satir, M. 2000. Coeval plutonism and metamorphism in a latest Oligocene metamorphic core complex in northwest Turkey. Geological Magazine 137(5), 495-516

Okay, A.I., Zattin, M. and Cavazza, W. 2010. Apatite fission-track data for Miocene Arabia-Eurasia collision. Geology, 38, 35-38.

Oncescu, M.C. 1986. Relative seismic moment tensor determination for Vrancea intermediate depth earthquakes. Pageoph., 124, 931-940.

Onescu, M.C. and Trifu, C.I. 1987. Depth variation of moment tensor principal axes in Vrancea (Romania) seismic region. Annales Geophysicae, 5B, 149-154.

Oral, M.B., Reilinger, R.E., Toksöz, M.N., Kong, R.W., Barka, A.A., Kınık, İ. and Cenk, O. 1995. Global positioning system offers evidence of plate motions in eastern Mediterranean, EOS Transac, 76, 9- 11.

Över, S., Pınar, A., Özden, S., Yılmaz, H., Ünlügenç, U.C. and Kamacı, Z. 2010. Late Cenozoic stress field in the Cameli Basin, SW Turkey. Tectonophysics 492(1), 60–72.

Över, S., Yılmaz, H., Pınar, A., Özden, S., Ünlügenç, U.C. and Kamacı, Z. 2013. Plio-Quaternary stress state in the burdur basin, SW-Turkey. Tectonophysics 588, 56–68.

Özacar, A.A, Zandt, G., Gilbert, H. and Beck, S.L. 2010. Geological Society, London, Special Publications, 340, 485-496.

Özbakır, A.D., Şengör, A.M.C.,Wortel, M.J.R., Govers, R. (2013). The Pliny–Strabo trench region:a large shear zone resulting fromslab tearing. Earth Planet. Sci. Lett. 375, 188–195.

Özkaptan, M., Kaymakci, N., Langereis, C.G., Gülyüz, E., Özacar, A.A., Uzel, B., Sözbilir, H. 2018. Age and kinematics of the Burdur Basin: Inferences for the

existence of the Fethiye Burdur Fault Zone in SW Anatolia (Turkey).Tectonophysics 744, 256-274.

Papazachos, B.C., Papaioannou, C.A., Papazachos, C.B. and Savvaidis, A.S. 1999. Rupture zones in the Aegean region. Tectonophysics 308, 205–221.

Pe-Piper, G. and Piper, D.J.W. 2007. Neogene back-arc volcanism of the Aegean: new insights into the relationship between magmatism and tectonics. In: Beccaluva, L., Bianchini, G. (Eds.), Cenozoic Volcanism in the Mediterranean Area: Geological Society of America Special Paper. Geological Society of America, pp. 17–31.

Philippon, M., Willingshofer, E., Sokoutis, D., Corti, G., Sani, F., Bonini, M. and Cloetingh, S. 2015. Slip re-orientation in oblique rifts. Geology 43, 147–150.

Philippon, M., Brun, J.P., Gueydan, F. and Sokoutis, D. 2014. The interaction between Aegean back-arc extension and Anatolia escape since Middle Miocene. Tectonophysics 631, 176-188.

Posamentier, H. W., Allen, G. P. and James, D. P. 1992a. High resolutionsequence stratigraphy – the East Coulee Delta, Alberta.Journal of Sedimentary Petrology, 62( 2), 310–317.

Posamentier, H. W., and Allen, G. P. 1999. Siliciclastic sequencestratigraphy: concepts and applications. SEPM Concepts inSedimentology and Paleontology 7, 210 p.

Price, S.P. and Scott, B. 1994. Fault-block rotations at the edge of a zone of continental extension; southwest Turkey. J Struct Geol 16: 381-392.

Rabillard, A., Jolivet, L., Arbaret, L., Bessiere, E., Laurent, V., Menant, A, Augier, R. and Beaudoin, A. 2018. Tectonic 10.1029/2017TC004697

Reilinger, R., McClusky, S., Vernant, P., Lawrence, S., Ergintav, S., Cakmak, R., Ozener, H., Kadirov, F., Guliev, I., Stepanyan, R., Nadariya, M., Hahubia, G.,

Mahmoud, S., Sakr, K., ArRajehi, A., Paradissis, D., Al-Aydrus, A., Prilepin, M., Guseva, T., Evren, E., Dmitrotsa, A., Filikov, S.V., Gomez, F., Al-Ghazzi, R. and Karam, G. 2006. GPS constraints on continental deformation in the Africa–Arabia–Eurasia continental collision zone and implications for the dynamics of plate interactions. J.Geophys. Res., Solid Earth 111.

Reilinger, R., McClusky, S., Paradissis, D., Ergintav, S. and Vernant, P. 2010. Geodetic constraints on the tectonic evolution of the Aegean region and strain accumulation along the Hellenic subduction zone. Tectonophysics, 488 (1–4), 22–30.

Ring, U. and Collins, A.S. 2004. U-Pb SIMS dating of syn-kinematic granites: Timing of core-complex formation in the northern Anatolide belt of western Turkey. Journal of the Geological Society, London (in press).

Roche, V., Conand, C., Jolivet, L. and Augier, R. 2018. Tectonic evolution of Leros Island (Dodecanese, Greece) and correlations between the Aegean Domain and the Menderes Massif. HAL Id: insu-01795049.

Roche, V. Jolivet, L., Papanikolaou, D., Rimmele, G., (2019)Slab fragmentation beneath the Aegean/Anatolia transition zone: Insights from the tectonic and metamorphic evolution of the Eastern Aegean region. Tectonophysics 754.

Rolland, Y. 2017. Caucasus collisional history: Review of data from East Anatolia to West Iran. Gondwana Research, 49, 130-146 pp.

Ron, H., Freund, R. and Garfunkel, Z. 1984. Block rotation by strike-slip faulting: Structural and Paleomagnetic evidence, Journal of Geophysical Research, 89, (B7), 6256-6270 pp.

Roveri, M., Manzi, V., Bergamasco, A., Falcieri, F. M., Gennari, R., Lugli, S. and Schreiber, B. C. 2014. Dense shelf water cascading and messinian canyons: a new scenario for the mediterranean salinity crisis. American Journal of Science, 314,3, 751-784.

Salamon, A., Hofstetter, A., Garfunkel, Z. and Hagai, R. 2003. Seismotectonics of the Sinai subplate–eastern Mediterranean region. Geophys. J. Int. 155, 149–173.

Salaün, G., Pedersen, H., Paul, A., Farra, V., Karabulut, H., Hatzfeld, D., Childs, D.M., Pequegnat, C. and SIMBAAD Team. 2012. High-resolution surface wave tomography beneath the Aegean-Anatolia region: constraints on upper mantle structure. Geophysical Journal International 190 (1), 406–420.

Sandwell, D.T.,M¨uller, R.D., Smith,W.H.F., Garcia, E. and Francis, R., 2014.New global marine gravity model from CryoSat-2 and Jason-1 reveals buried tectonic structure, Science, 346(6205), 65–67.

Schneider, W.A. and Backus, M. M. 1964. Ocean-bottom seismic measurements off the California coast. Journal of Geophysical Research , 69, 1135–1143.

Seyitoğlu, G. and Scott, B. 1991. Late Cenozoic crustal extension and basin formation in west Turkey. Geological Magazine, 128(2), 155-166.

Seyitoglu, G. and Scott, B. C. 1996b. The cause of N-S extensional tectonics in western Turkey: Tectonic escape vs. Back-arc spreading vs. Orogenic collapse. Journal of Geodynamics, 22, 145 - 153.

Seyitoglu, G., Isik, V. and Cemen, I. 2004. Complete Tertiary exhumation history of the Menderes massif, western Turkey: an alternative working hypothesis. Terra Nova, 16, 358-364.

Seyitoğlu, G., Tekeli, O., Çemen, I., Şen, Ş. and Işık, V. 2002. The role of the flexural rotation/rolling hinge model in the tectonic evolution of the Alaşehir graben, western Turkey. Geological Magazine 139(1), 15-26 pp.

Shaw, B. and Jackson, J. 2010. Earthquake mechanisms and active tectonics of the Hellenicsubduction zone. Geophysical Journal International 181, 966–984.

Sheriff, R. and Geldart L.P. 1995. Exploration Seismology. 2nd edn. Cambridge: Cambridge University Press.

Simkin, T. and Siebert, L. 2002. "Volcanoes of the world: an illustrated catalog of holocene volcanoes and their eruptions". Smithsonian Institution. Gloval volcanism program digital information series, GVP-3.

Smith, A.G. 1971. Alpine deformation and the oceanic areas of the ( tethys, Mediterranean and Atlantic). Geol. Soc. Am. Bull., 82, 2039-2070.

Siebert, L. and Simkin, T. 2008. Volcanoes of the World: an illustrated catalog of Holocene volcanoes and their eruptions., Smithsonian Institution Digital Information Series GVP-3. http://www.volcano.si.edu/gvp/world. Last accesed July 2019.

Stewart, R.R., Gaiser, J. E., Brown, R.J. and Lawton, D. C. 2002. Converted-wave seismic exploration: method.,Geophysics , 67, 1348–1363.

Strelitz, R. A. 1980. The fate of a downgoing slab: A study of the moment tensors from body waves of complex deep-focus earthquakes. Phys. Earth planet. Inter., 21, 83-96.

Şenel, M. 1997a. Geological Map of Fethiye, L8 Quadrangle, No: 2, 1:100,000 General Directorate of Mineral Research and Exploration, Ankara, Turkey 22 pp.

Şenel, M., 1997b. Geological Map of Fethiye, M8 Quadrangle, No: 4, 1:100,000. General Directorate of Mineral Research and Exploration, Ankara, Turkey 15 pp.

Şenel, M. and Bölükbaşı, A.S. 1997. Geological Map of Fethiye, M9 Quadrangle, No: 5, 1:100,000. General Directorate of Mineral Research and Exploration, Ankara, Turkey 11 pp.

Şengör, A.M.C. 1979. Mid-Mesozoic closure of Permo-Triassic Tethys and its implications. Nature, 279, 590-593,

Şengör, A.M.C. and Yılmaz, Y. 1981. Tethyan evolution of Turkey: aplate tectonic approach. Tectonophysics 75, 181–241.

Şengör, A.M.C. and Sungurlu, O. 1984. Tectonics of the Mediterranean Cimmerides: nature and evolution of the western termination of Palaeo-TethysGeological Society, London, Special Publications 17 (1), 77-112.

Şengör, A.M.C. 1985. The Alpides and Cimmerides-the doubled history of the Tethys Geologische Rundschau 74 (2), 181-213.

Şengör, A.M.C. and Bozkurt, E. 2013. Layer-parallel shortening and related structures in zones undergoing active regional pure horizontal extension. "International Journal of Earth Sciences", 102, 101-119 p.

Taymaz, T., Jackson, J.A. and McKenzie, D.P. 1991. Active tectonics of the north and central Aegean Sea. Geophysical Journal International 106, 433–490.

Taymaz, T., and Price, S. P. 1992. The 12.05.1971 Burdur earthquake sequence: A synthesis seismological and geological observations. Geophys. J. Int., 108, 589-603.

Ten Veen, J.H. and Kleinspehn, K.L. 2002. Geodynamics along an increasingly curved convergent plate boundary: Late Mioicene-Pleistocene Rhodes, Greece. Tectonics, 21(3), 1017-1029.

Ten Veen, J.H. 2004. Extension of the Hellenic forearc shear zones in SW Turkey: the Pliocene-Quaternary deformation of the Eşen Çay Basin. Journal of Geodynamics, 37, 181–204.

Ten Veen, J.H., Boulton, S.J. and Alçiçek, M.C. 2008. From palaeotectonics to neotectonics in the Neotethys realm: The importance of kinematic decoupling and inherited structural grain in SW Anatolia (Turkey). Tectonophysics 473, 261–281.

Ten Veen, J.H., Boulton, S.J. and Alçiçek, M.C. 2009. From palaeotectonics to neotectonics in the Neotethys realm: the importance of kinematic decoupling and inherited structuralgrain in SW Anatolia (Turkey). Tectonophysics, 473, 261–281.

Thomson, S. N. and Ring, U. 2006. Thermochronologic evaluation of postcollision extension in the Anatolide orogen, western Turkey Tectonics, 25(3).

Tiryakioglu, I., Floyd, M., Erdogan, S., Gulal, E., Ergintav, S., Mc-Clusky, S. and Reilinger, R. 2013. GPS constraints on active deformationin the Isparta Angle region of SW Turkey, Geophys. J. Int., 195(3), 1455–1463.

Tohon, D.S., Sintubin, M., Muchez, P., Verhaert, G., Vanneste, K., Fernandez, M., Vandycke, S., Vanhaverbeke, H. and Waelkens, M. 2006. The identification of an active fault by a multidisciplinary study at the archaeological site of Sagalassos (SW Turkey).Tectonophysics,  435(1–4), 55-62 pp.

Vail, P. R., Audemard, F., Bowman, S. A., Eisner, P. N. and Perez-Cruz, C. 1991. The stratigraphic signatures of tectonics, eustasy andsedimentology–an overview. In Cycles and Events in Stratigraphy. (G. Einsele, W. Ricken and A. Seilacher, Eds.), 617–659 pp. Berlin, Springer-Verlag.

Van Hinsbergen, D.J.J., Dekkers, M. J., Bozkurt, E. and Koopman, M. 2010. Exhumation with a twist: Paleomagnetic constraints on the evolution of the Menderes metamorphic core complex, western Turkey. Tectonics, 29(3).

Van Wagoner, J. C., Mitchum, R. M. Jr., Campion, K. M. and Rahmanian, V. D. 1990. Siliciclastic sequence stratigraphy inwell logs, core, and outcrops: concepts for high-resolution correlationof time and facies. American Association of Petroleum Geologists Methods in Exploration Series 7, 55 p.

Vasco, D.W. 1990. Moment-tensor invariants: Searching for non double couple earthquakes, Bulletin of the Seismological Society of America, 80, 345-371.

Verhaert, G., Muchez, P., Sintubin,M., Similox-Tohon, D., Vandycke, S., Keppens, E., Hodge, E. J. and Richards, D.A. 2004. Origin of palaeofluids in a normal fault setting in the Aegeanregion. Geofluids 4 (4), 300–314.

Verhaert, G., Similox-Tohon, D., Vandycke, S., Sintubin, M. and Muchez, P. 2006. Different stress states in the Burdur-Isparta region (SW Turkey) since LateMiocene times: a reflection of a transient stress regime. J. Struct. Geol. 28, 1067–1083.

Vidal, N., Alvarez-Marron, J. and Klaeschen, D. 2000. The structure of the Africa-Anatolia plate boundary in the eastern Mediterranean. Tectonics, 19, 723-739.

Yılmaz, A., Adamia, S., Chabukiani, A., Chkhotua, T., Erdoğan, K., Tuzcu, S. and Karabıyıkoğlu, M. 2000. Structural Correlation of the Southern Transcaucasus (Georgia)-Eastern Pontides (Turkey). Geological Society, London, Special Publications, 173, 171-182 pp.

Yolsal, S., Taymaz, T. and Yalçıner, A. C. 2007. Understanding tsunamis, potential source regions and tsunami prone mechanisms in the Eastern Mediterranean. In: Taymaz, T., Yılmaz, Y. and Dilek, Y. (Eds.), The Geodynamics of the Aegean and Anatolia. Geological Society. 291. Special Publications, London, 201–230.

Zachariasse, W.J., van Hinsbergen, D.J.J. and Fortuin, A. R. 2008. Mass wasting and uplift on Crete and Karpathos during the early Pliocene related to initiation of south Aegean left-lateral strike–slip tectonics. Bulletin of the Geological Society of America, 120, 976–993.

Zhu, C., Cheng, S.,Li, Q., Shan, H., Lu, J., Shen, Z., Liu, X. and Jia, Y. 2019. Giant Submarine Landslide in the South China Sea: Evidence, Causes, and Implications. J. Mar. Sci. Eng. 7, 152 p.

Zitter, T.A.C., Woodside, J.M. and Mascle, J. 2003. The Anaximander Mountains: a clue to the tectonics of southwest Anatolia. Geological Journal 38, 375– 394.

Williams, G., Powell, M. and Cooper M. 1989. Geometry and Kinematics of Inversion Tectonics , Geological Society, London, Special Publications, 44, 3-15, 1.

Woodside, J. M. 1977. Tectonic elements and crust of the eastern Mediterranean Sea, Journal of Geophysical Research, 99, 12071-12090.

Woodside, J., Mascle, J., Huguen, C. and Volkonskaia, A. 2000. The Rhodes Basin, a postMiocene tectonic trough. Mar. Geol. 165, 1–12.

Wortel, M. J. R. and  Spakman, W. 2000. Subduction and Slab Detachment in the Mediterranean-Carpathian Region .Science   290(5498), 1910-1917.